Max-Planck-Institut
für Meteorologie

MAX-PLANCK-GESELLSCHAFT

# Development and application of a high-resolving atmosphere-microphysics-chemistry model for prediction of aerosol characteristics in the vicinity of sources

Álvaro M. Valdebenito B.

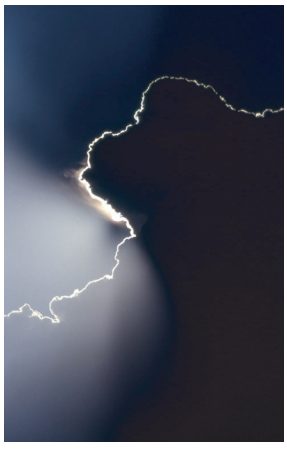

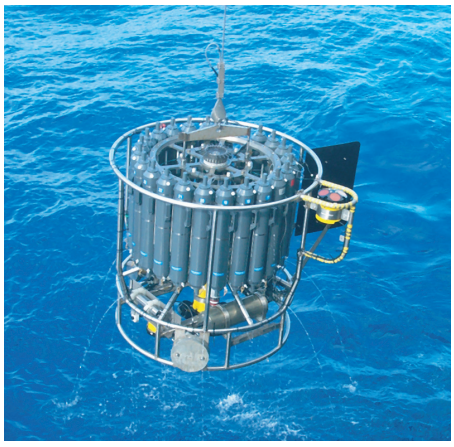

Berichte zur Erdsystemforschung 69/2009

*Reports on Earth System Science*

Berichte zur Erdsystemforschung 69/2009

# Development and application of a high-resolving atmosphere-microphysics-chemistry model for prediction of aerosol characteristics in the vicinity of sources

Álvaro M. Valdebenito B.

aus Santiago, Chile

Hamburg 2009

*Reports on Earth System Science* 69/2009

ISSN 1614-1199

Álvaro M. Valdebeníto B.
Max-Planck-Institut für Meteorologie
Bundesstrasse 53
20146 Hamburg
Germany

Als Dissertation angenommen
vom Department Geowissenschaften der Universität Hamburg

auf Grund der Gutachten von
Prof. Dr. K. Heinke Schlünzen
und
Prof. Dr. Gerhard Lammel

Hamburg, den 29. Oktober 2008
Prof. Dr. Jürgen Oßenbrügge
Leiter des Departments für Geowissenschaften

ISSN 1614-1199

# Development and application of a high-resolving atmosphere-microphysics-chemistry model for prediction of aerosol characteristics in the vicinity of sources

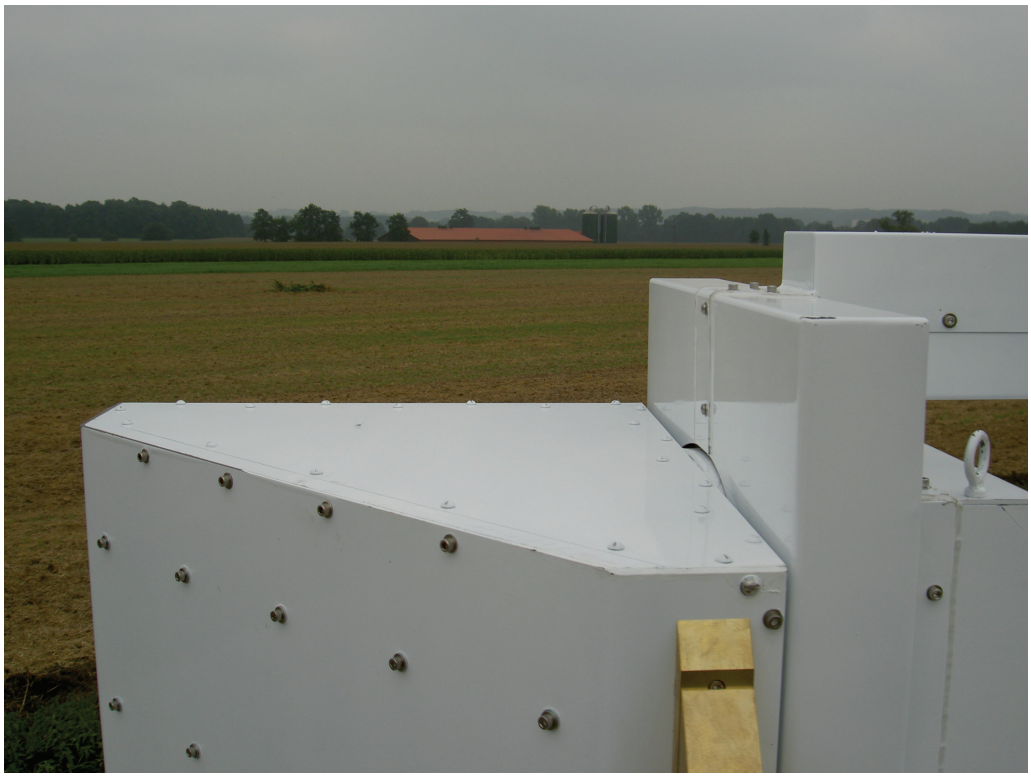

Álvaro M. Valdebenitó B.

Hamburg 2009

Dedicated to my family,
the one I was born into and the one I found away from home.

# ABSTRACT

This work describes the development and first results of a new high-resolution microphysics-chemistry-transport model (LES-AOP). The LES-AOP model was developed to simulate the aerosol optical properties during the PLUS1 measurement campaign, which was performed in the vicinity of a livestock farm in northern Germany. The model is an extension of a Large-Eddy Simulation (LES) model, where a simple aerosol module was developed to calculate the aerosol optical properties. Only a limited number of aerosol processes is included due to the high computational demand.

The project in which the model was developed aimed to combine high-resolution model results with 3-D lidar measurements performed by the University of Hohenheim. This combination would allow an insight view of the aerosol characteristics on high spatial and temporal scales, even at low aerosol concentrations (e.g. faint sources). One of the major model achievements is the prediction of the aerosol optical properties (with resolutions below 100 $\mathrm{m}$ and 1 $\mathrm{min}$) upon initialisation by meteorological and aerosol data. In addition, the model is able to positively detect faint aerosol plumes (with aerosol backscattering coefficient down to $10^{-6}/(\mathrm{sr\ m})$) and discard false positives identified by the lidar. Furthermore, it is possible from the model results and ground measurements to estimate budget-related quantities, such as the emission flux and mass change of the particulate matter.

# ZUSAMMENFASSUNG

Die vorliegende Arbeit beschreibt die Entwicklung und erste Ergebnisse eines neuen kleinskaligen Mikrophysik-Chemie-Transport-Modells (LES-AOP). Es wurde entwickelt, um die optischen Eigenschaften von Aerosolen während der PLUS1-Messkampagne zu simulieren, welche in der Nähe eines Tierhaltungsbetriebes in Norddeutschland durchgeführt wurde. Das Modell ist eine Erweiterung eines Grobstruktür-Simulation (LES) Modells um ein einfaches Aerosolmodul, welches die optischen Eigenschaften der Aerosole berechnet. Aufgrund des hohen Rechenaufwands wurde nur eine begrenzte Anzahl von Aerosolprozessen im Modell berücksichtigt.

Das Projekt, im Zuge dessen das Modell entwickelt wurde, hatte zum Ziel Ergebnisse hochauflösender Modelle mit 3-D Lidarmessungen der Universität Hohenheim zu kombinieren. Dieses Vorgehen ermöglicht einen Einblick in das Verhalten von Aerosolen mit hoher zeitlicher und räumlicher Auflösung selbst bei niedrigen Aerosolkonzentrationen (beispielsweise für schwache Quellen). Eine der Haupterrungenschaften des Modells ist die Vorhersage der optischen Eigenschaften der Aerosole (bei einer Auflösung von unter 100 $\mathrm{m}$ und 1 $\mathrm{min}$) nach Initialisierung desselben mit meteorologschen und Aerosol-Daten. Ferner ist das Modell in der Lage schwache Aerosolwolken (mit einem Rückstreukoeffizienten von bis zu $10^{-6}/(\mathrm{sr\ m})$) nachzuweisen und fehlerhafte Messungen des Lidars zu verwerfen. Es war ausserdem möglich mit Hilfe von Modellergebnissen und Bodenmessungen budgetbezogene Größen, wie den Emissionsfluss und die Massenänderung des Partikelmaterials, abzuschätzen.

x

# CONTENTS

# LIST OF FIGURES

## LIST OF TABLES

# ACRONYMS

| | |
|---|---|
| LES | Large-Eddy Simulation |
| SGS | Sub-Grid Scale |
| AOP | Aerosol Optical Properties |
| CRI | Complex Refractive Index |
| NSD | Aerosol Number (wet) Size Distribution |
| NMD | Aerosol Number (dry) Mass Distribution |
| LIDAR | LIght Detection And Ranging |
| OPC | Optical Particle Counter |
| LAMMA | Laser Ablation Micro Mass Analyzer |
| PPI | Plane Polar Indicator |
| RHI | Range-Height Indicator |

prehensive aerosol module. However, only two simulations where 3-D with a reduced spatial resolution of $\Delta x = \Delta y = 80$ m, $\Delta z = 25$ m, while most of their simulations were performed in 2-D with a $\Delta x = 50$ m, $\Delta z = 25$ m resolution. In this work all simulations are performed in 3-D with a spatial resolution of $\Delta x = \Delta y = 50$ m, $\Delta z = 20$ m. Newsom and Banta (2004a) developed a 4D-VAR algorithm for retrieval of coherent Doppler lidar using a LES model.

In this thesis, the following two chapters describe the large-eddy simulation model (LES, Chapter 2) and the extended LES model to aerosol optical properties (LES-AOP model, Chapter 3). Chapters four and five deal with the measurement campaign (PLUS1, Chapter 4) and the LES-AOP model simulations performed for two days of the campaign (Chapter 5). The final chapter summarises the conclusions and gives an outlook (Chapter 6).

# 2

# LARGE-EDDY SIMULATION MODEL

To simulate turbulent flow the Large-Eddy Simulation model (LES) explicitly calculates the large scale three-dimensional motions, capturing the largest and most energetic structures in the flow while parametrising the effect of the sub-grid-scale eddies (Chlond, 1992, 1998a). The model uses *Boussinesq* equations for the wind components, liquid water potential temperature and total water content (Chlond and Wolkau, 2000). This section is mainly based on Chlond (1992, 1998a,b); Chlond and Wolkau (2000). For a more detailed description of the LES model than the one presented here please refer to them and references therein.

## 2.1 EQUATIONS

The motion of a compressible fluid involving friction and gravity is described by the the *Navier Stokes* equations, which ensure the balance of mass, momentum and energy. Unfortunately, there is no unique general to the *Navier Stokes* equations. Therefore, the *Boussinesq* approximation provides a better framework for numerical simulation. In the *Boussinesq* approximation differences in density are neglected, unless they are multiplied by the gravitational acceleration.

In the following, all thermodynamic variables are separated into a reference term (upper index $^{00}$) and the deviation from the reference (upper index $^{*}$ ). The reference state of the atmosphere is assumed to be constant in time, horizontally homogeneous, stationary, hydrostatic and adiabatic. In addition, the reference air density is assumed constant with height, which is a reasonable assumption as the vertical dimension of the studied motion is small compared with the extent of the atmosphere to be simulated (Chlond, 1998a).

The simplified equations of motion, written in vector notation are:

$$\nabla \cdot \mathbf{u} = 0 \tag{2.1}$$

$$\frac{\partial \mathbf{u}}{\partial t} + \nabla \cdot (\mathbf{u} \otimes \mathbf{u}) = -\frac{1}{\rho^{00}} \nabla p^* - \frac{\mathbf{g}}{\rho^{00}} \rho^* - \mathbf{f} \times (\mathbf{u} - \mathbf{U}_g) + \nu \Delta \mathbf{u} \tag{2.2}$$

$$\frac{\partial \psi_k}{\partial t} + \nabla \cdot (\psi_k \, \mathbf{u}) = Q^{\psi_k} + \gamma^{\psi_k} \Delta \psi_k \tag{2.3}$$

where in Cartesian rotated coordinates $\mathbf{x} = (x_1, x_2, x_3) = (x, y, z)$, $\mathbf{u} = (u_1, u_2, u_3) = (u, v, w)$ stands for the wind velocity, $\mathbf{g} = (0, 0, g)$ is the gravitational vector, $\mathbf{f} = (0, 0, f)$ the Coriolis vector, and $\mathbf{U}_g = (U_g, V_g, 0)$ the geostrophic wind vector. Following the vector notation $\nabla$ represents the gradient operator, and $\Delta$ the Laplace operator. Additionally, $\cdot$ denotes the internal product, $\times$ the cross product, and $\otimes$ the tensor product (Gurtin, 1981). In equation (2.2, conservation of momentum) $p^*$ is the pressure deviation, $\rho^{00}$ the reference air density, $\rho^*$ the (moist) air density and $\nu$ the kinematic (shear) viscosity. The index $k$ in equation (2.3, conservation of the scalar quantitie $\psi_k$) refers to each specific scalar quantity $\psi_k$, $Q^{\psi_k}$ to its sources and sinks, and $\gamma^{\psi_k}$ to the respective diffusion coefficient.

The potential liquid water temperature $\theta_l$ and the total liquid water content $q$ are prognosticated using the conservation equation of scalar quantities (2.3, with e.g. $\psi_1 = \theta_l$ and $\psi_2 = q$), where the source and sink terms are described by:

$$Q^{\theta_l} = \left(\frac{\partial \theta_l}{\partial t}\right)_{\text{prec.}} + \left(\frac{\partial \theta_l}{\partial t}\right)_{\text{rad.}}$$

$$Q^{q} = \left(\frac{\partial q}{\partial t}\right)_{\text{prec.}}$$

where the lower indices prec. and rad. refer to precipitation and radiation.

The *Boussinesq* approximated equation of state reads:

$$\frac{\mathbf{g}}{\rho^{00}} \rho^* = \frac{\mathbf{g}}{\theta_v^{00}} (\theta_v - \theta_v^{00}) = \frac{\mathbf{g}}{\theta_v^{00}} \theta_v^*$$

where $\theta_v$ is the potential virtual temperature. The potential virtual temperature $\theta_v$ is calculated as in Sommeria and Deardorff (1977), following:

$$\theta_v = \theta \, (1 + 0.61 \, q_v - q_l) = \theta \, (1 + 0.61 \, q - 1.61 \, q_l)$$

where $\theta$ is the potential temperature, $q_v$ is the specific humidity and $q_l$ the liquid water content ($q = q_v + q_l$). A linearised version[1] of the potential liquid water temperature $\theta_l$ is used in this work (Chlond, 1998a):

$$\theta_l = \theta - \left(\frac{\theta}{T}\right) \frac{L_v}{c_p} q_l$$

where $T$ is the temperature $L_v$ the latent heat of vaporisation, $c_p$ specific heat of dry air under constant pressure and $q_l$ the liquid water content. In accordance with the *Boussinesq* approximation, and with help from the hydrostatic relation for the reference pressure ($p^{00}$), the term $\left(\frac{\theta}{T}\right)$ is calculated by:

$$\left(\frac{\theta}{T}\right) = \left(\frac{p_0}{p^{00}}\right)^{\kappa}$$

where $\kappa = 0.286$ denotes the adiabatic coefficient for dry air, and $p_0 = p^{00}(0) = 1000$ hPa the reference pressure at surface level. In presence of ice, the equations describing $q$, $\theta_v$ and $\theta_l$ take a slightly different form (Chlond, 1998a).

## 2.2 RESOLVED SCALE

Without further assumptions, the Direct Numerical Simulation (DNS) of equations (2.1), (2.2) and equation (2.3) for $\theta_l$ and $q$ would resolve all scales of motion down to the dissipation length. Unfortunately, the high computational cost of such an approach limits its scope to the simulation of flows with low to moderate Reynolds numbers. In the Large-Eddy Simulation (LES) approach only the large scale three-dimensional motions are resolved, while the small scale motions are filtered out from equations (2.1)–(2.3). The LES approach allows to simulate more intense turbulence than the DNS for the same computaqtional costs.

The filtering process used in the LES models separates the motion in resolved and nonresolved scales, introducing new variables to the equation of motion representing nonresolved scale. For a generic variable $\psi$, the filtered variable $\overline{\psi}$ represents the convolution with the filter operator $G$ over the complete fluid domain $D$:

$$\overline{\psi}(\mathbf{x}) = (G \circ \psi)(\mathbf{x}) = \int_D G(\mathbf{x} - \mathbf{y})\, \psi(\mathbf{y}) \mathrm{d}\, \mathbf{y}$$

The filtering process can be thought as a local averaging, with $G$ as some kind of weighting function. The purpose of the filtering is to remove high frequency

1 The potential liquid water temperature $\theta_l$ is defined in Betts (1973) as "... the potential temperature attained by evaporating all the liquid water in an air parcel through reversible wet adiabatic descent". The linear approximation described here is accurate to a few percent (Betts, 1973).

fluctuations ($\psi'$) from the total field ($\psi = \overline{\psi} + \psi'$). The choice of the filter operator is not unique (Gaussian filter, box filter, cutting filter, etc.), but its net effect on the resolved scale is of minor importance (Clark *et al.*, 1979).

Structures larger then the characteristic length of the filter (or large eddies) are resolved by the numerical integration of the filtered equations. Smaller structures are nonresolved, and their influence on the large eddies is parametrised. The nonresolved scale is referred in the literature as the sub-grid scale for historical reasons, although sub-filter would be a more appropriate term. In this study both terms are equivalent and will not be distinguished. The parametrisation of the sub-grid variables introduced by the filtering are presented in Section 2.3.

The filtered equations representing the resolved scales of motion are:

$$\nabla \cdot \overline{\mathbf{u}} = 0 \tag{2.4}$$

$$\frac{\partial \overline{\mathbf{u}}}{\partial t} + \nabla \cdot (\overline{\mathbf{u}} \otimes \overline{\mathbf{u}}) = -\frac{1}{\rho^{00}} \nabla \overline{\pi} - \frac{\mathbf{g}}{\theta_v^{00}} \overline{\theta_v^*} - \mathbf{f} \times (\overline{\mathbf{u}} - \mathbf{U}_g) - \nabla \cdot \boldsymbol{\sigma} \tag{2.5}$$

$$\frac{\partial \overline{\psi_k}}{\partial t} + \nabla \cdot (\overline{\psi_k}\, \overline{\mathbf{u}}) = \overline{Q^{\psi_k}} - \nabla \cdot \mathbf{F}^{\psi_k} \tag{2.6}$$

where the over-bar sign ($\overline{\ }$) denotes the filtered variables, $\boldsymbol{\sigma}$ represents the anisotropic part of the *subgrid-scale Reynolds stress tensor* ($\boldsymbol{\tau}$), $\overline{\pi}$ the modified pressure (which includes the isotropic part of $\boldsymbol{\tau}$) and $\mathbf{F}^{\psi_k} = (F_1^{\psi_k}, F_2^{\psi_k}, F_3^{\psi_k})$ the turbulent flux for the scalar quantity $\psi_k$. These terms are formally described by:

$$\begin{aligned}
\boldsymbol{\tau} &= \overline{\mathbf{u}' \otimes \mathbf{u}'} = \overline{\mathbf{u} \otimes \mathbf{u}} - \overline{\mathbf{u}} \otimes \overline{\mathbf{u}} \\
\boldsymbol{\sigma} &= \boldsymbol{\tau} - \frac{1}{3} \mathrm{tr}(\boldsymbol{\tau}) \mathbb{I} \\
\overline{\pi} &= \overline{p^*} + \frac{1}{3} \mathrm{tr}(\boldsymbol{\tau}) \\
\mathbf{F}^{\psi_k} &= \overline{\psi_k{}' \mathbf{u}'} = \overline{\psi_k \mathbf{u}} - \overline{\psi_k}\, \overline{\mathbf{u}}
\end{aligned}$$

where $\mathrm{tr}(\boldsymbol{\tau}) = \tau_{11} + \tau_{22} + \tau_{33}$ is the trace of $\boldsymbol{\tau}$, and $\mathbb{I}$ is the identity tensor. By writing $u_i = \overline{u}_i + u_i'$ and using the Kronecker delta ($\delta_{ij}$), $\boldsymbol{\tau}$, $\boldsymbol{\sigma}$ and $\mathbf{F}^{\psi_k}$ are described on the component level by:

$$\begin{aligned}
\tau_{ij} &= \overline{u_i' u_j'} = \overline{u_i u_j} - \overline{u}_i \overline{u}_j = \overline{\overline{u}_i \overline{u}_j} + \overline{\overline{u}_i u_j'} + \overline{u_i' \overline{u}_j} - \overline{u}_i \overline{u}_j \\
\sigma_{ij} &= \tau_{ij} - \frac{1}{3} \mathrm{tr}(\boldsymbol{\tau})\, \delta_{ij} = \overline{u_i' u_j'} - \frac{1}{3} \left( \overline{u_1'^2} + \overline{u_2'^2} + \overline{u_3'^2} \right) \delta_{ij} \\
F_j^{\psi_k} &= \overline{\psi_k{}' u_j'} = \overline{\psi_k u_j} - \overline{\psi_k}\, \overline{u}_j = \overline{\overline{\psi_k}\, \overline{u}_j} + \overline{\overline{\psi_k}\, u_j'} + \overline{\psi_k{}' \overline{u}_j} - \overline{\psi_k}\, \overline{u}_j
\end{aligned}$$

## 2.3 UNRESOLVED SCALE

The filtered equations of motion (2.4)–(2.6) can only be resolved when the unresolved scale (sub-grid scale or SGS) fluxes are determined in terms of the resolved-scale fields. Similar to the SGS model described in Deardorff (1980), the SGS model described here is based on transport of the SGS kinetic energy $\overline{e} = \frac{1}{2}\mathrm{tr}(\boldsymbol{\tau}) = \frac{1}{2}\left(\overline{u_1'^2} + \overline{u_2'^2} + \overline{u_3'^2}\right)$:

$$\frac{\partial \overline{e}}{\partial t} + \nabla \cdot (\overline{e} \otimes \overline{\mathbf{u}}) = -\boldsymbol{\sigma} \cdot (\nabla \otimes \overline{\mathbf{u}}) + \frac{g}{\theta_v^{00}} \overline{u_3' \theta_v'} - \nabla \cdot \overline{\left(e' + \frac{\pi'}{\rho^{00}}\right) \mathbf{u}'} - \frac{c_\varepsilon}{\Lambda} \overline{e}^{3/2} \quad (2.7)$$

where the first two right-hand-side terms correspond to the production of SGS kinetic energy due to local shear and buoyancy. The third term corresponds to transport and the fourth to viscous dissipation, where $c_\varepsilon$ is a stability-dependent coefficient and $\Lambda$ is the characteristic turbulent length scale.

Following a first order closure, the SGS fluxes are parametrised as:

$$\begin{aligned}
\boldsymbol{\sigma} &= -K_m \left( (\nabla \otimes \overline{\mathbf{u}}) + (\nabla \otimes \overline{\mathbf{u}})^T \right) \\
\mathbf{F}^{\theta_l} &= -K_h \nabla \overline{\theta}_l \\
\mathbf{F}^{q} &= -K_h \nabla \overline{q} \\
\overline{\left(e' + \frac{\pi'}{\rho^{00}}\right) \mathbf{u}'} &= -K_h \nabla \overline{e} \\
\overline{u_3' \theta_v'} &= K_1 \overline{u_3' \theta_l'} + K_2 \overline{u_3' q'} \\
&= K_1 F_3^{\theta_l} + K_2 F_3^{q} = -K_h \left( K_1 \frac{\partial \overline{\theta}_l}{\partial x_3} + K_2 \frac{\partial \overline{q}}{\partial x_3} \right)
\end{aligned}$$

where the upper index $^T$ denote the transpose operator, $K_m$ is the SGS eddy coefficient for momentum and $K_h$ the SGS eddy coefficient for heat and all other scalar quantities. The SGS eddy coefficients are proportional to the length scale ($\Lambda$) and the turbulent kinetic energy ($\overline{e}^{1/2}$), correspondingly:

$$\begin{aligned}
K_m &= c_m \Lambda \overline{e}^{1/2} \\
K_h &= c_h \Lambda \overline{e}^{1/2}
\end{aligned}$$

where $c_m$ and $c_h$ are stability-dependent coefficients.

$K_1$ and $K_2$ are simplified versions of the coefficients introduced in Sommeria and Deardorff (1977). Here, $K_1$ and $K_2$ coefficients are given by:

$$K_1 = 1 - \frac{b\,\alpha\left(\frac{L_v}{c_p} - 1.61\,\theta^{00}\left(\frac{T}{\overline{\theta}}\right)\right)}{1 + \alpha\frac{L_v}{c_p}}$$

$$K_2 = 0.61\,\theta^{00} + \frac{b\left(\frac{L_v}{c_p}\left(\frac{\theta}{\overline{T}}\right) - 1.61\,\theta^{00}\right)}{1 + \alpha\frac{L_v}{c_p}}$$

where $\alpha$ is defined as:

$$\alpha = \left(\frac{\partial q_s}{\partial T}\right)_{T=\overline{T}_l} = 0.622\,L_v\,\frac{q_s(\overline{T}_l)}{R_d\,\overline{T}_l^2}$$

and $R_d$ is the gas constant for dry air, $r$ the subgrid-scale cloud fraction and $\overline{T}_l = \left(\frac{T}{\overline{\theta}}\right)\overline{\theta}_l$.

Following Deardorff (1980) and Chlond (1998b), the length scale ($\Lambda$) is:

$$\Lambda = \begin{cases} \min\left(0.7\,z,\,\Delta\right) & N_{BV}^2 \leqslant 0 \\ \min\left(0.7\,z,\,\Delta,\,\frac{0.76\,\overline{e}^{1/2}}{N_{BV}}\right) & N_{BV}^2 > 0 \end{cases}$$

where $\Delta = (\Delta x + \Delta y + \Delta z)/3$ is the averaged grid scale, with $\Delta x$, $\Delta, y$ and $\Delta z$ are the respective grid intervals and $N_{BV}$ is the Brunt-Väisälä frequency defined by:

$$N_{BV}^2 = \frac{g}{\theta_v^{00}}\left(K_1\frac{\partial\overline{\theta}_l}{\partial z} + K_2\frac{\partial\overline{q}}{\partial z}\right)$$

Finally, the stability-dependent coefficients for viscous dissipation ($c_\varepsilon$), momentum ($c_m$) and scalar quantities ($c_h$) are:

$$c_\varepsilon = \begin{cases} 0.7 & N_{BV}^2 \leqslant 0 \\ 0.19 + \frac{0.51\,\Lambda}{\min\left(0.7\,z,\Delta\right)} & N_{BV}^2 > 0 \end{cases}$$

$$c_m = 0.1$$

$$c_h = \begin{cases} 3\,c_m & N_{BV}^2 \leqslant 0 \\ \left(1 + \frac{2\,\Lambda}{\min\left(0.7\,z,\Delta\right)}\right)c_m & N_{BV}^2 > 0 \end{cases}$$

## 2.4 GAS-PHASE CHEMISTRY

The gas-phase chemistry and aerosol nucleation modules, were introduced to the LES model by Müller (2004, unpublished). The documentation is scarce, mostly

consisting of comments in the code. The gas-phase and aerosol nucleation module consists of a photochemical mechanism, extended for ternary nucleation of $H_2SO_4$-$NH_3$-$H_2O$ particles. It consists of 37 species, including new aerosol particles, and 107 reactions. The photochemical mechanism is based on 95 reactions from the "condensed LCC mechanism" from Lurmann *et al.* (1987) with 2 extra reactions from the OZIPM version of the LCC mechanism from Lurmann *et al.* (1987), 8 extra reactions from Carter (1990), 1 extra reaction from Japar *et al.* (1990), and 1 extra reaction from Atkinson (1990). The resulting system of differential equations is integrated using a hybrid integration technique. Chemical reactions are divided into "stiff" and "normal" reactions. An implicit iterative scheme is used for the stiff reactions, while an explicit scheme is used for the normal ones. See Gong and Cho (1993) for an example of such an implicit/explicit technique.

## 2.5 NUMERICAL SOLUTION

The conservation equation of scalar quantities (2.6) applies to potential liquid water temperature ($\overline{\theta}_l$), total liquid water content ($\overline{q}$), sub-grid scale (SGS) kinetic energy ($\overline{e}$), and all other scalar quantities. Operator splitting is applied to equation (2.6), dividing it into "advection" and "rest" parts (Chlond, 1998a):

$$\frac{\partial \overline{\psi_k}}{\partial t} = \underbrace{-\nabla \cdot (\overline{\psi_k}\,\overline{\mathbf{u}})}_{\text{advection}} + \underbrace{\overline{Q^{\psi_k}} - \nabla \cdot \mathbf{F}^{\psi_k}}_{\text{rest}}$$

A numerical solution of the advection part of equation (2.6) is obtained via a hybrid scheme (Chlond, 1994). The hybrid scheme combines the Bott (1989a,b) third order flux scheme and an exponential upwind scheme (Spalding, 1972). The use of either of these two schemes, at any particular location of the model domain, is controlled by a self-adjusting switch (Chlond, 1994). The third order flux scheme is used on "smooth regions", away of sharp varying gradients which may cause unphysical oscillations. The exponential upwind scheme is used on the "sharp varying gradient regions" were the monotonicity of the exponential interpolation function is ensured by construction, and no flux limiters are needed in order to avoid spurious oscillations. The 1-D hybrid scheme is extended to a 3-D scheme by a directional splitting technique with alternating dimensions (e.g. $x$–$y$–$z$ on odd iterations and $z$–$y$–$x$ on even iterations).

The conservation equation of momentum (2.5) relates the changes in the wind components ($\overline{u}_i$) and modified pressure ($\overline{\pi}$) to buoyancy and sub-grid scale (SGS) stress. A numerical solution is attained via a predictor-corrector step. In the predictor step, the wind components are prognosticated using the hybrid scheme by Chlond (1994). Unlike the advection for scalar quantities, here the full equation

is taken into account, i.e. there is no division into "advection" and "rest" parts. In the corrector step, pressure change is diagnosed and the wind components corrected via red-black successive-over-relaxation (SOR). The red-black SOR is a particular implementation of the SOR iterative algorithm by Young (1950) in which the dependencies between adjacent gridpoints are decoupled, allowing efficient parallelisation via domain decomposition.

## 2.6 BOUNDARY CONDITIONS

The model domain extends horizontally and vertically over a finite domain of size $L_x \times L_y \times L_z$. The lateral boundaries are assumed to be periodic (lateral cyclic boundary condition). At the top of the model domain, a zero gradient condition applies to variables except $\overline{w}$, $\overline{q}$ and $\overline{\theta}_l$. It is imposed that the vertical velocity $\overline{w}$ is zero at the top and the gradients of $\overline{q}$ and $\overline{\theta}_l$ are constant over time (Neumann boundary condition). At the surface level, a zero gradient condition applies to $\overline{e}$ and $\overline{p}$.

In order to avoid reflections of gravity waves at the upper boundary a Rayleigh friction term is added to equation (2.6). This is done by introducing an artificial "sponge" layer in the upper third of the model domain (Müller and Chlond, 1996). The coefficient of Rayleigh damping $\nu$ increases gradually through the "sponge" layer according to:

$$\nu = \begin{cases} \nu_0 \, \sin^2\left(\frac{\pi}{2} \frac{z-z_s}{L_z-z_s}\right) & z_s < z \leqslant L_z \\ 0 & 0 < z \leqslant z_s \end{cases}$$

where $L_z$ is the vertical extent of the model domain, $z_s = 2L_z/3$ is the base of the "sponge" layer, and $\nu_0 = (300s)^{-1}$.

At the lower boundary, Monin-Obukhov similarity theory is used to relate the fluxes of various quantities to the corresponding difference between the surface value and the value at the lowermost model level at $z = z_r = \Delta z/2$:

$$\begin{aligned} \sigma_{i3} &= -u_* \frac{\overline{u}_i(z_r)}{\sqrt{\overline{u}_1^2(z_r) + \overline{u}_2^2(z_r)}} \quad i = 1, 2 \\ F_3^{\theta_l} &= -u_* \, \theta_* \\ F_3^{q} &= -u_* \, q_* \end{aligned} \tag{2.8}$$

where the scaling parameters $u_*$, $\theta_*$ and $q_*$ are defined as:

$$\begin{aligned} u_* &= \frac{\kappa\sqrt{\overline{u}_1^2(z_r) + \overline{u}_2^2(z_r)}}{\ln\left(\frac{z_r}{z_0^m}\right) - \Psi_m\left(\frac{z_r}{L}\right)} \\ \theta_* &= \frac{\kappa\left(\overline{\theta}_l(z_r) - \overline{\theta}_l(z_0^h)\right)}{\ln\left(\frac{z_r}{z_0^h}\right) - \Psi_h\left(\frac{z_r}{L}\right)} \\ q_* &= \frac{\kappa\left(\overline{q}_l(z_r) - \overline{q}_l(z_0^h)\right)}{\ln\left(\frac{z_r}{z_0^h}\right) - \Psi_h\left(\frac{z_r}{L}\right)} \end{aligned} \tag{2.9}$$

$\kappa$ is von Karman's constant, $z_0^m$ is the aerodynamic roughness length for momentum, $z_0^h$ is the aerodynamic roughness length for heat and all other scalar quantities, and $L$ is the Monin-Obukhov length at the surface:

$$L = \frac{u_*^2}{\kappa\,\frac{g}{\theta_v^{00}}(\theta_* + 0.61\,\theta_v^{00}\,q_*)}$$

and $\Psi_m$ and $\Psi_h$ are defined as:

$$\begin{aligned} \Psi_m\left(\frac{z'}{L}\right) &= \int_{z_0^m}^{z'}\left[1 - \phi_m\left(\frac{z}{L}\right)\right]\frac{dz}{z} \\ \Psi_h\left(\frac{z'}{L}\right) &= \int_{z_0^h}^{z'}\left[1 - \phi_h\left(\frac{z}{L}\right)\right]\frac{dz}{z} \end{aligned}$$

where, following Webb (1982) and Chlond (1998a), the stability function for momentum ($\phi_m$) and the stability function for heat and all other scalar quantities ($\phi_h$) are:

$$\begin{aligned} \phi_m\left(\frac{z}{L}\right) &= \begin{cases} 1 + 6.9\,\frac{z}{L} & \frac{z}{L} \geqslant 0 \\ \left(1 - 20.3\,\frac{z}{L}\right)^{-1/4} & \frac{z}{L} < 0 \end{cases} \\ \phi_h\left(\frac{z}{L}\right) &= \begin{cases} 1 + 9.2\,\frac{z}{L} & \frac{z}{L} \geqslant 0 \\ \left(1 - 12.2\,\frac{z}{L}\right)^{-1/2} & \frac{z}{L} < 0 \end{cases} \end{aligned} \tag{2.10}$$

## 2.7 INITIALISATION AND FORCING

In order to numerically solve the system of equations formed by the filtered equations of motion and the sub-grid scale (SGS) model, the initial state of the main thermodynamic variables, wind components and SGS kinetic energy needs to

be determined. In addition to the model constants, vertical boundary conditions and large scale variations are needed in order to integrate in time. Of the many slightly different LES model versions documented in Chlond (1992, 1998a,b) and Chlond and Wolkau (2000), the particular model implementation used in this work uses prescribed surface fluxes for the main thermodynamic variables ($F_3^{\theta_l}$ and $F_3^q$). In order to include the effect of the heterogeneity of the synoptic scale meteorology, a large-scale correction term (lower index LS) is included to the right hand side of equations (2.4)–(2.6). A summary of the model constants, initialisation and forcing variables can be found in Table 1.

| Variable | LES Levels | | |
|---|---|---|---|
| | Surface $0$ [m] | Mid Levels $z_{i+\frac{1}{2}}$ | Top $L_z$ |
| **Model Constants**[§] | | | |
| reference pressure | $p^{00}$ | — | — |
| reference potential liquid water temperature | $\theta_l^{00}$ | — | — |
| reference total liquid water content | $q^{00}$ | — | — |
| Coriolis parameter | $f$ | — | — |
| roughness length for momentum | $z_0^m$ | — | — |
| roughness length for heat[†] | $z_0^h$ | — | — |
| **Initialisation Variables** | | | |
| potential liquid water temperature | — | $\overline{\theta}_l$ | — |
| total liquid water content | — | $\overline{q}$ | — |
| SGS kinetic energy | — | $\overline{e}$ | — |
| $u$ wind component | — | $\overline{u}$ | — |
| $v$ wind component | — | $\overline{v}$ | — |
| $w$ wind component | — | $\overline{w}$ | — |
| **Forcing variables** | | | |
| vertical boundary conditions for $\overline{\theta}_l$ | $F_3^{\theta_l}$ | — | $\frac{d\overline{\theta}_l}{dz}$ |
| vertical boundary conditions for $\overline{q}$ | $F_3^q$ | — | $\frac{d\overline{q}}{dz}$ |
| large scale advection of $\overline{\theta}_l$ | — | $\left(\frac{\partial\overline{\theta}_l}{\partial t}\right)_{LS}$ | — |
| large scale advection of $\overline{q}$ | — | $\left(\frac{\partial\overline{q}}{\partial t}\right)_{LS}$ | — |
| large scale variation of $\overline{u}$ [§] | — | $\left(\frac{\partial\overline{u}}{\partial t}\right)_{LS}$ | — |
| large scale variation of $\overline{v}$ [§] | — | $\left(\frac{\partial\overline{v}}{\partial t}\right)_{LS}$ | — |
| large scale subsidence[§] | — | $\left(\frac{\partial\overline{w}}{\partial t}\right)_{LS}$ | — |
| $u$ geostrophic wind component | — | $U_g$ | — |
| $v$ geostrophic wind component | — | $V_g$ | — |

[§] Constant value through the model domain.

[†] $z_0^h$ is the roughness length for heat and all other scalar quantities.

Table 1: Summary of LES model constants, initialisation and forcing variables. The model mid levels are located at $z_{i+\frac{1}{2}} = (i+\frac{1}{2})\Delta z$ for $i = 0, \ldots, n_z - 1$, where $z = 0$ corresponds to the surface level, $z = L_z$ to the model top, and $n_z = L_z/\Delta z$ to the number of model levels.

# 3

## EXTENSION OF THE LES MODEL BY AN AEROSOL MODULE FOR CALCULATION OF AEROSOL OPTICAL PROPERTIES

The Large-Eddy Simulation (LES) model (Chapter 2), has been extended to simulate aerosol optical properties. The aerosol optical properties to be simulated by the aerosol-extended model (LES-AOP) are described in Section 3.1. The discussion of the choice of aerosol processes to be included in the LES-AOP model can be found in Section 3.2. The aerosol module is described in Section 3.3 and detailed descriptions of some particular model components can be found in subsequent sections.

The LES-AOP model simulates the changes of the aerosol particle number (wet) size distribution (NSD) in every grid point of the model domain and every time step. It is initialised from ground measurements and calculates the aerosol optical properties off-line during the post processing. The LES-AOP model treatment of the aerosols can be divided in three steps (Figure 1):

AEROSOL NSD INITIAL CONDITION: from in-situ measurements, e.g. data from a cascade impactor, a near-ground NSD is derived. The 3-dimensional fields representing the aerosol NSD initial condition of the model simulation are calculated from this near-ground NSD and some assumptions about the aerosol vertical profile (Section 3.8).

AEROSOL NSD TIME EVOLUTION: starting from the aerosol fields generated in the *Initial Condition* step, the changes over time and space of the aerosol NSD (Section 3.2) are simulated in this step.

AEROSOL OPTICAL PROPERTIES: the aerosol extinction and backscattering coefficient fields (Section 3.1) are calculated. These aerosol optical properties are calculated off-line from the aerosol NSD and meteorological conditions simulated over time and space on the *Time Evolution* step.

Figure 1 shows the schematic representation of the treatment of the aerosols in the LES-AOP model. Meteorological conditions are covered by the original LES

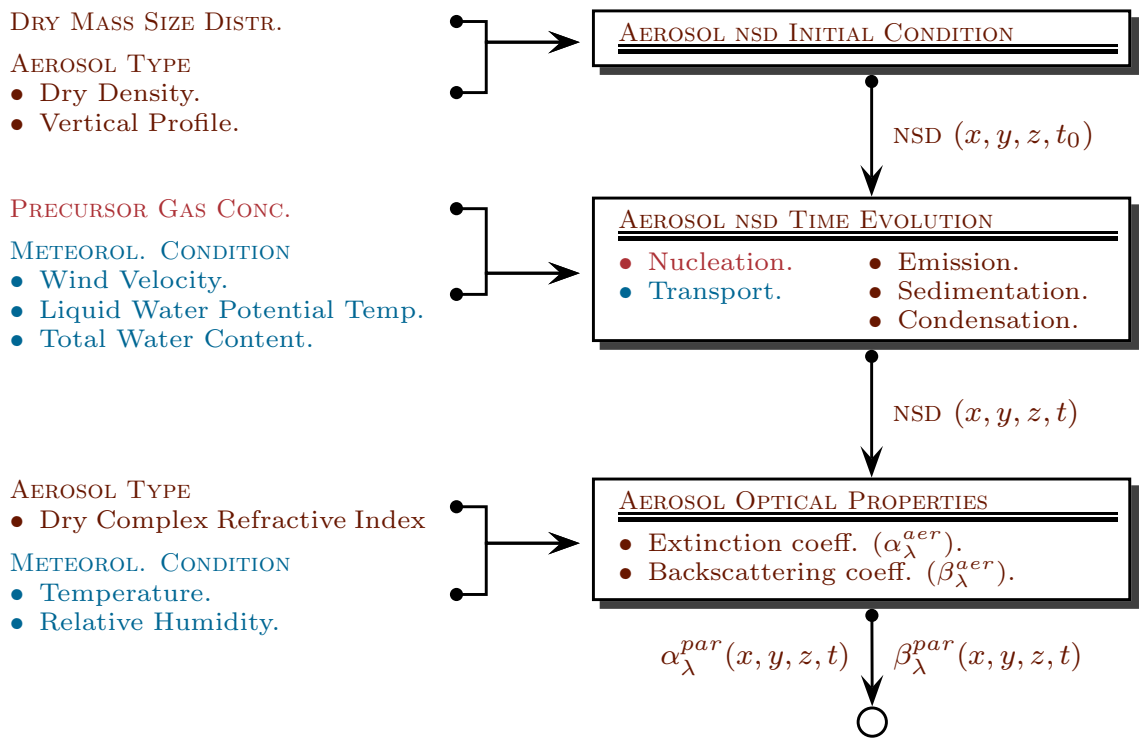


Figure 1: Schematic representation of the LES model extended to Aerosol Optical Properties (LES-AOP). Original LES model in BLUE. Gas phase chemistry and aerosol nucleation RED. LES-AOP model developed as part of this work in BROWN.

model (Chapter 2). Gas phase chemistry and aerosol nucleation were included to the LES model before the start of this work (Section 2.4). Aerosol transport was originally implemented following the transport for scalar quantities of the LES model, and later modified to allow non-cyclic boundary conditions (Section 3.7.2). The aerosol NSD representation, optical properties and a few aerosol processes are included in the LES-AOP model as part of this work.

## 3.1 AEROSOL OPTICAL PROPERTIES

Under several assumptions, aerosol optical properties such as the aerosol extinction and backscattering coefficients ($\alpha^{par}$ and $\beta^{par}$) can be retrieved from the lidar signal (Fernald, 1984; Fernald *et al.*, 1972; Klett, 1981, 1985). This is the meeting point between the computational simulation and the lidar field campaign data. A description of the retrieval algorithm and its working assumptions can be found in Section 4.5.

For an aerosol described as a mixture of different aerosol species, $\alpha^{par}$ and $\beta^{par}$ can be calculated from the NSD of each species, by the following equations:

$$\alpha^{par} = \sum_{aer} \int_{r_p} Q_{ext}^{aer}(r_p)\, \pi r_p^2\, n^{aer}(r_p)\, d\, r_p \tag{3.1}$$

$$\beta^{par} = \sum_{aer} \int_{r_p} Q_{bsc}^{aer}(r_p)\, \pi r_p^2\, n^{aer}(r_p)\, d\, r_p \tag{3.2}$$

where $aer$ stands for the aerosol species, $Q_{ext}^{aer}$ and $Q_{bsc}^{aer}$ for the extinction and backscattering efficiencies, $n^{aer}(r_p)$ is the number of particles with (wet) radius $r_p$. Making use of the Mie theory (Boheren and Huffman, 1983), $Q_{ext}^{aer}$ and $Q_{bsc}^{aer}$ are calculated as function of the particle radius, the lidar wavelength, the particulate matter composition, structure (homogeneous or stratified spheres) and complex refractive index. For a more detailed description see Appendix A.

The Mie calculations involved in $Q_{ext}^{aer}$ and $Q_{bsc}^{aer}$ can be even more computationally demanding than all the other aerosol processes together, making the full on-line calculation of $\alpha^{par}$ and $\beta^{par}$ impractical. Fortunately, under the assumption that the aerosol NSD is constant over each size bin, equations (3.1) and (3.2) are rewritten as shown in equations (3.6) and (3.7). The values for the mean extinction and backscattering coefficients, equations (3.3) and (3.4), are pre-calculated for each size bin and stored in a look-up table (on aerosol structure, composition, hygroscopicity, etc., Section 3.3.3) allowing efficient computing time by the usage of the pre-calculated data during the post-processing.

Assuming that for each aerosol species *"the particles are uniformly distributed over each size bin"*, i.e, for each aerosol species ($aer$) the number density is constant over each size bin ($bin$):

$$n^{aer}(r_p) = \sum_{bin} n_{bin}^{aer} \cdot \mathbb{1}_{[a_{bin}, b_{bin}]}(r_p)$$

where $bin$ is an interval of the form $[a_{bin}, b_{bin}]$, and $\mathbb{1}$ is the indicatrix function defined as:

$$\mathbb{1}_{[a_{bin}, b_{bin}]}(r_p) = \begin{cases} 1 & \text{if } a_{bin} \leqslant r_p \leqslant b_{bin} \\ 0 & \text{otherwise} \end{cases}$$

then the integral on the right hand side of equations (3.1) and (3.2) can be written as:

$$\int_{r_p} Q_{ext}^{aer}(r_p)\, \pi r_p^2\, n^{aer}(r_p)\, d\, r_p = \sum_{bin} \alpha_{bin}^{aer}\, N_{bin}^{aer}$$

$$\int_{r_p} Q_{bsc}^{aer}(r_p)\, \pi r_p^2\, n^{aer}(r_p)\, d\, r_p = \sum_{bin} \beta_{bin}^{aer}\, N_{bin}^{aer}$$

where $\alpha_{bin}^{aer}$ and $\beta_{bin}^{aer}$ are the extinction and backscattering coefficients for the mean cross-section, and $N_{bin}^{aer}$ the total particle number over bin, defined by:

$$\alpha_{bin}^{aer} = \frac{1}{b_{bin} - a_{bin}} \int_{a_{bin}}^{b_{bin}} Q_{ext}^{aer}(r_p)\, \pi r_p^2 \, d\, r_p \tag{3.3}$$

$$\beta_{bin}^{aer} = \frac{1}{b_{bin} - a_{bin}} \int_{a_{bin}}^{b_{bin}} Q_{bsc}^{aer}(r_p)\, \pi r_p^2 \, d\, r_p \tag{3.4}$$

$$N_{bin}^{aer} = (b_{bin} - a_{bin})\, n_{bin}^{aer} = \int_{a_{bin}}^{b_{bin}} n^{aer}(r_p)\, d\, r_p \tag{3.5}$$

Finally $\alpha_{bin}^{aer}$ and $\beta_{bin}^{aer}$ can be pre-calculated and stored in a look-up table (Section 3.3.3) and the aerosol extinction and backscattering coefficients, equations (3.1) and (3.2), can be simply calculated as:

$$\alpha^{par} = \sum_{aer} \sum_{bin} \alpha_{bin}^{aer}\, n_{bin}^{aer} \tag{3.6}$$

$$\beta^{par} = \sum_{aer} \sum_{bin} \beta_{bin}^{aer}\, n_{bin}^{aer} \tag{3.7}$$

The extinction and backscattering efficiencies for homogeneous and heterogeneous aerosol particles are calculated using the source code provided by Boheren and Huffman (1983, Appendix A and B). The inherent assumptions behind this code, and the implementation of equations (3.3), (3.4) (3.6) and (3.7) in the aerosol module are:

SINGLE SCATTERING: the light *"bounces only one time"* between the source and the observer. This is a good approximation when the distance between the particles is much larger than the wavelength of the light. For aerosols this is the case, with the exceptions of haze or inside a cloud.

PARALLEL LIGHT: this is a more than reasonable assumption for a distant source, like the sun. It is granted in the case of a laser beam, like in the lidar case.

ADDITIVITY: the extinction, absorption and backscattering coefficients of a mixture of particles can be obtained as the sum of the coefficients of each individual particle. Which is valid under *single scattering* conditions.

SPHERICALLY SYMMETRIC PARTICLES: the aerosol particles have a spherically symmetric structure with one (homogeneous) or two layers (heterogeneous).

HOMOGENEOUS LAYERS: the one or two layers of the aerosol structure are of homogeneous composition. The water insoluble component does not take up water. The water soluble component is fully dissolved while taking up water.

HETEROGENEOUS PARTICLES: have a core layer composed of insoluble material and a shell layer composed of water soluble material and water.

The analytical solution for scattering of light by spherical homogeneous particles provided by the *Mie theory* is by now the classical approach (e.g. Hess *et al.*, 1998; Köpke *et al.*, 1997; Wiscombe, 1979, 1980). Since its publication, the implementation by Boheren and Huffman (1983) for spherical particles and coated spheres (two-layered shell structure) is the most widely used.

The effect of particle shape and structure have been studied in several publications. In Mishchenko *et al.* (1997) the authors study the effect of particle shape on the optical properties of *dust-like tropospheric aerosols*, they conclude that the effects of non-sphericity on the backscattering coefficient can be large and should be explicitly taken into account when inverting lidar measurements of dust-like aerosols. The question of external aggregation is addressed by Mishchenko *et al.* (2004), where the authors conclude that two particle external aggregation is "likely to have a weak effect on scattering".

## 3.2 AEROSOL PROCESSES

Among the processes that change the aerosol particle size distribution, only a fraction have been included in the aerosol module. The description of these and a discussion about the excluded processes are the subject of this section.

The equation describing the temporal variation of the aerosol NSD is as follows:

$$\frac{dn}{dt}(r_p) = \overbrace{\left(\frac{\partial n}{\partial t}(r_p)\right)_{\substack{\text{macrophysics}\\ \text{nucleation}\\ \text{condensation}\\ \text{coagulation}}}}^{} + \overbrace{\left(\frac{\partial n}{\partial t}(r_p)\right)_{\substack{\text{transport}\\ \text{advection}\\ \text{turbulent diffusion}\\ \text{Brownian diffusion}}}}^{} + \underbrace{\left(\frac{\partial n}{\partial t}(r_p)\right)_{\substack{\text{sedimentation}\\ \text{gravitational settling}\\ \text{dry deposition}\\ \text{wet deposition}}}}_{} + \left(\frac{\partial n}{\partial t}(r_p)\right)_{\substack{\text{surface}\\ \text{emission}}}$$

NUCLEATION is the formation of new particles from precursor gases. Rates for ternary nucleation of $H_2SO_4$-$NH_3$-$H_2O$ as function of atmospheric temperature and concentration of precursor gases are obtained via a photochemical mechanism (Section 2.4).

CONDENSATION of water on the particles is described by the equilibrium between water vapour and condensed water represented by a simple *Köhler curve*, which combines the *Kelvin effect* and *Raoult's law* for spherical particles:

$$\ln(S) = \frac{A}{r_p} - \frac{B r_{dry}^3}{r_p^3 - r_{dry}^3} \tag{3.8}$$

where $S$ is a coefficient that takes into account the saturation ($S$ = relative humidity$[-]$), $A$ the curvature effect and $B$ the solute effect (hygroscopicity).

$$\begin{aligned} S &= \frac{e_a}{e_{sat,w}} \\ A &= \frac{2\sigma_{s,a}\,\overline{v}_w}{R_w\,T} \\ B &= \varepsilon_m \frac{\upsilon\,\phi_s\,\overline{v}_w}{\overline{v}_s} \end{aligned} \tag{3.9}$$

where $e_a$ and $e_{sat,w}$ are the water vapour pressure and the saturation vapour pressure; $R_w$ the specific gas constant for pure water vapour; $\varepsilon_m$ the mass fraction of water soluble material in the dry aerosol; $\upsilon$ the total number of ions of the water soluble material when fully dissociated; $\phi_s$ the practical osmotic coefficient of the water soluble material; $\overline{v}_w$ and $\overline{v}_s$ are the molar volume of water and the aerosol water soluble part, which can be calculated by:

$$\begin{aligned} \overline{v}_w &= \frac{M_w}{\rho_w} \\ \overline{v}_s &= \frac{M_s}{\rho_s} \end{aligned}$$

where $M_w$ and $M_s$ represent the molar weight, $\rho_w$ and $\rho_s$ the densities of the water and the aerosol water soluble part. Values for $\phi_s$ can be found in Robinson and Stokes (1959), for more detailed information refer to Hänel (1976); Seinfeld and Pandis (1998).

In the aerosol module the hygroscopicity can be described by a polynomial expansion of an empirical growth curve or by the idealised hygroscopicity of a pure salt. The values used in this work are listed in Table 16 and Table 17 (Appendix B). An example of the effect on the particle size of these two representations can be found in Figure 2. Due to the wide size spectra covered by the aerosol module, it is difficult to appreciate the differences of the particle (wet) radius given by the two parameterisations (Figure 2a,b). However, this difference becomes evident in the particle growth factor figures (Figure 2c,d). It is clear that the idealised pure salt hygroscopicity for $(NH_4)_2SO_4$ results in particles of roughly $20-50$ % larger radius than the empirical growth curve for continental aerosol.

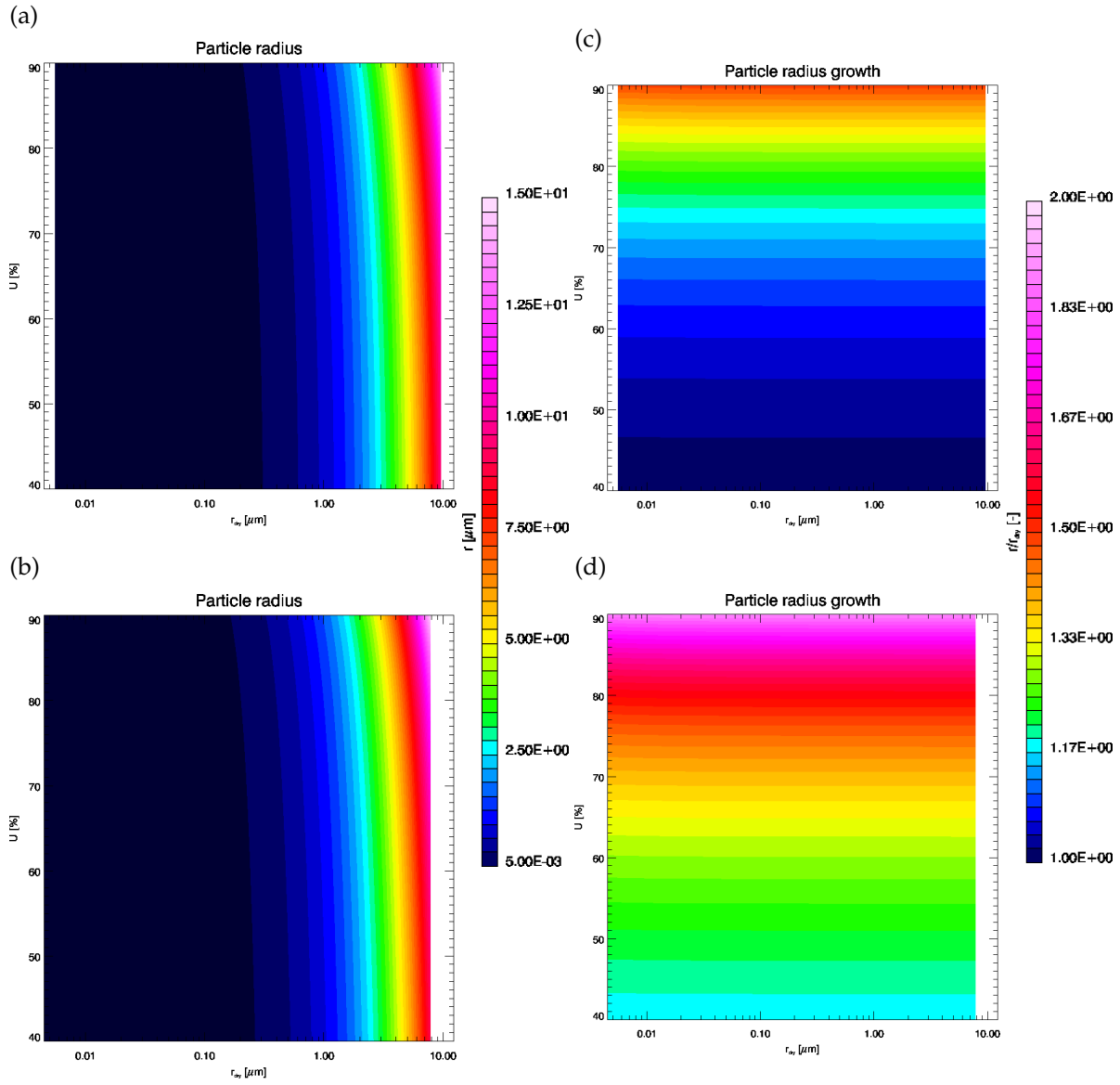


Figure 2: Example of particle growth for different hygroscopicity parametrisations. Particle (wet) radius (a,b); and particle growth factor (c,d) for different dry radius and relative humidities at 20°C. Empirical growth curve for continental aerosol from Deuselbach-large-particles in Winkler (1988) (a,c). Idealised pure salt hygroscopicity for $(NH_4)_2SO_4$ from osmotic coefficients found in Robinson and Stokes (1959) (b,d). See Appendix B for more details on the hygroscopicity parametrisations.

COAGULATION of particles is neglected. From the early design stage, the LES-AOP model was targeted towards the simulation of an isolated aerosol ground source (Chapter 5), forced from ground measurements (Section 4.4.1). Its results were to be compared with 3-D lidar observations near to the source (Section 4.4.2). Background and polluted aerosol fields were to be compared in the near ground levels close to the aerosol source, which is where the focus of this study lies.

The surface boundary condition (Section 3.7.1) was conveniently set in order to force the aerosol fields towards the observed near-ground NSD and composition. Therefore, near to the ground, the relative importance of the coagulation process is secondary to the selection of the surface boundary condition. For the polluted aerosol fields, the transport time between source location and the out-flow boundary of the model domain is relatively short (8–20 minutes), and the observational characterisation of the aerosol in the source plume is rather limited, specially regarding the NSD. All of this, in addition to the high computational cost of the coagulation, make it an unattractive component for this first application of the LES-AOP model.

Later on, the lidar measurements indicated that the source plume stayed close to the ground, and the ground measurements indicated that no gas to particle conversion took place downwind from the source (Table 6). Thus, reinforcing the notion that the inclusion of particle coagulation into the LES-AOP model may have a small, if any, influence on the model results. For a different use, e.g. the study of the temporal evolution of the background aerosol, the LES-AOP model may however, need the inclusion of the coagulation process. But that discussion is outside the scope of this work. The effect of particle coagulation on the NSD, in terms of the coagulation coefficient (K), is described by (Debry and Sportisse, 2007; Seigneur *et al.*, 1986; Zhang *et al.*, 1999):

$$\left(\frac{\partial n}{\partial t}(r_p)\right)_{coag.} = \frac{1}{2}\int_{r<r_p} K(r^3, r_p^3 - r^3)\, n(r)\, n(\sqrt[3]{r_p^3 - r^3})\, dr - n(r_p)\int_{r>r_p} K(r^3, r_p^3)\, n(r)\, dr$$

ADVECTION was originally included following the implementation of transport of scalar quantities of the LES model (Chapter 2) and has then been modified to allow non-cyclic lateral boundary conditions (Section 3.7.2). The contribution of *advection* to the change of the NSD is:

$$\left(\frac{\partial n}{\partial t}(r_p)\right)_{advection} = -\nabla \cdot (\mathbf{u}\, n(r_p))$$

TURBULENT DIFFUSION is implemented following the numeric scheme for scalar quantities of the LES model (Chapter 2). The effect of *turbulent diffusion* on the NSD is:

$$\left(\frac{\partial n}{\partial t}(r_p)\right)_{\substack{\text{turbulent}\\\text{diffusion}}} = -\nabla \cdot (D_t \, \nabla n(r_p))$$

BROWNIAN DIFFUSION is the macroscopic representation of the particle Brownian motion, the result of the almost constant collisions between particles. It is specially important for the smaller particles and is described by:

$$D_b(r_p) = \frac{k_B T C_c(r_p)}{6\pi \rho_{air} \nu_{air} r_p} \tag{3.10}$$

where $r_p$ stands for the particle radius, $k_B$ is the *Boltzmann's constant*, $\rho_{air}$ and $\nu_{air}$ the air density and kinematic viscosity and $C_c(r_p)$ the *Cunningham Correction Factor* which takes into account the effects of non-continuity of the medium, specially important when the particle radius is of the same order of magnitude as the mean free path of the air (Section C.2). The effect of the *Brownian diffusion* on the NSD is described by:

$$\left(\frac{\partial n}{\partial t}(r_p)\right)_{\substack{\text{Brownian}\\\text{diffusion}}} = -\nabla \cdot (D_b(r_p) \, \nabla n(r_p))$$

GRAVITATIONAL SETTLING is described by the settling velocity ($v_s$, Section 3.4):

$$\left(\frac{\partial n}{\partial t}(r_p)\right)_{\substack{\text{gravitational}\\\text{settling}}} = -v_s(r_p) \, n(r_p)$$

DRY DEPOSITION of particles on the ground surface and its vegetation cover, is taken into account on the lowermost model level by the deposition velocity ($v_d$, Section 3.5), as part of the aerosol surface flux (ASF, Section 3.7.1):

$$\left(\frac{\partial n}{\partial t}(r_p)\right)_{\substack{\text{dry}\\\text{deposition}}} = \begin{cases} v_d(r_p) \, n(r_p) & \text{lowermost model level} \\ 0 & \text{otherwise} \end{cases}$$

WET DEPOSITION has been neglected. The LES-AOP model intends to simulate aerosol optical properties provided by a volume scanning lidar, like the lidar system of the University of Hohenheim (UHOH) employed on the PLUS1 measurement campaign (Section 4.4.2). The UHOH scanning aerosol lidar system is unable to "see inside clouds", therefore aerosol in-cloud processes have been neglected. Another limitation of the UHOH scanning aerosol lidar system is that it can not operate when raining, therefore below cloud scavenging has been neglected.

SURFACE EMISSION and re-suspension of particles is taken into account on the lowermost model level by the aerosol surface flux (ASF, Section 3.7.1).

## 3.3 AEROSOL MODULE

The changes of the aerosol NSD included in the LES-AOP model can be summarised by the following equation:

$$\frac{\mathrm{d}\,n}{\mathrm{d}\,t}(r_p) = \overbrace{\left(\frac{\partial n}{\partial t}(r_p)\right)_{\text{macrophysics}}}^{\substack{\text{nucleation}\\ \text{condensation}}} + \overbrace{\left(\frac{\partial n}{\partial t}(r_p)\right)_{\text{transport}}}^{\substack{\text{advection}\\ \text{turbulent diffusion}\\ \text{Brownian diffusion}}} + \underbrace{\left(\frac{\partial n}{\partial t}(r_p)\right)_{\text{sedimentation}}}_{\substack{\text{gravitational settling}\\ \text{dry deposition}}} + \left(\frac{\partial n}{\partial t}(r_p)\right)_{\substack{\text{surface}\\ \text{emission}}} \tag{3.11}$$

The processes were already discussed in detail in Section 3.2. Only those processes that are considered in the LES-AOP are kept in equation (3.11).

### 3.3.1 *Representation of the Aerosol Population*

The aerosol module focuses on the aerosol optical properties such as the aerosol extinction and backscattering coefficients (Section 3.1). These properties are dependent on particle size, number composition and structure (Appendix A). In this model, aerosol particles are first differentiated according to their composition and structure. Particles are divided accordingly into distinct aerosol species. All particles in a particular species are assumed to have the same structure, dry density, hygroscopic properties and dry complex refractive index.

Particles belonging to different aerosol species scatter light independently of each other. Secondly, inside of each species, particles are differentiated according to their dry size (or the equivalent dry mass). Therefore, the aerosol NSD of each species is tracked independently, i.e. one NSD for each species. Particles of the same dry size can have different dry composition if they belong to different species. The differentiation of particles in the same species according to their dry size will be referred in the following as the *bin scheme*. The size *bin scheme* is a discrimination of the continuous number NSD of each aerosol species. A size bin is a discrete interval of the size spectrum, where it is assumed that all the particles in a size bin are spherical and identical, i.e. the particles have the same structure, composition and radius.

Changes in the temperature or relative humidity will cause a change in the size and composition of the aerosol particles, due to gain or loss of water, affecting the aerosol NSD and the aerosol optical properties (Hänel, 1976; Tang, 1996). Due to this and the high computing demand of the aerosol optical properties[1], a set of equivalent wet size bin schemes and basic optical properties are pre-calculated to match the same dry mass discretisation under different temperatures and relative humidities. For these pre-calculations, the aerosol NSD initialisation and later calculation of the aerosol optical properties, each aerosol species should be characterised by a set of parameters like dry density, initial vertical profile[2], dry complex refractive index and other parameters describing the hygroscopicity of the aerosol species.

The number of aerosol species, the bin scheme resolution and basic properties of each aerosol species, are user configurable. For each aerosol specie, the hygroscopicity parametrisation and the water soluble fraction of the total aerosol mass can vary over particle dry size, but it is assumed that it will remain constant over the simulation time. The aerosol particles are indistinguishable beyond the dry size resolution of the bin scheme, where all the members are assumed to be identical. Sets of dry density and dry complex refractive index data for different aerosol species are taken from Hess *et al.* (1998) and Hale and Querry (1973), and can be found in Table 15. The detailed description of parameters describing the hygroscopicity of the different aerosol species can be found in Appendix B.

### 3.3.2 *Aerosol Structure and Mixture*

The assumptions of the particle structure and mixing plays an important role in the calculation of the aerosol optical properties (Mishchenko *et al.*, 1997, 2004). The concept of aerosol mixture is not employed consistently across the aerosol literature. Buseck and Pósfai (1999) classifies aerosol mixtures into *external*, *internal homogeneous* and *internal inhomogeneous* mixtures, according to the phases present inside the particles. Mishchenko *et al.* (2004) classifies aerosol mixtures into *external*, *semi-external* and *internal* mixtures, according to the way particles scatter light. Mineral dust particles can be both a *semi-external* mixture according to Mishchenko *et al.* (2004) and an *internal inhomogeneous* mixture according to Buseck and Pósfai (1999). Figure 3 attempts to reconcile both classifications.

1 A fully on-line simulation of optical properties for 1h over a $1km^3$ model domain with a $50m \times 50m \times 20m \times 5s$ resolution would take roughly 26 CPU-days with the extended LES model.

2 For initialisation purposes, an exponential decrease with height is assumed for the number for particles.

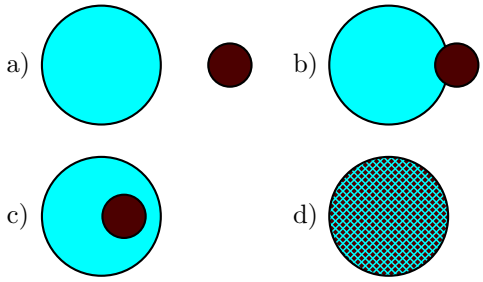


Figure 3: Schematic representation of different types of aerosol mixture: (a) external mixture; (b) semi-external mixture (particle clusters with touching components, Mishchenko *et al.*, 2004); (c) heterogeneous internal mixture; (d) homogeneous internal mixture.

As mentioned before, internal and external mixture is not used consistently in the literature. Externally mixed aerosol often implies homogeneous particles. Internally mixed aerosol often implies only one NSD. In this sense, the aerosol module can be configured to represent an internally or externally mixed aerosol population, but it is not limited to these descriptions. The aerosol population may be described by more than one species, each one with one NSD. Within each species, particles are not necessarily of homogeneous structure. In the aerosol module, particles are represented by one of the following structures:

HOMOGENEOUS STRUCTURE: spherical particle of homogeneous composition, which can be either water insoluble (Figure 4a) or water soluble (Figure 4b).

HETEROGENEOUS STRUCTURE: spherically symmetrical particle, with a simple two layer shell structure, namely a water insoluble *core* and a water soluble *shell* (Figure 4c). When one of the layers is missing, the resulting structure is equivalent to the spherical aerosol of homogeneous composition.

### 3.3.3 *Aerosol Particle Size Distribution*

The high computing cost of the calculation of the aerosol optical properties makes the on-line calculation during the model simulation practically impossible. Instead some kind of look up table needs to be implemented for this purpose.

The aerosol optical properties are functions of the number concentration, size, structure and composition of the aerosol particles. Assuming that the aerosol population can be represented by a set of different aerosol species, and that the dry composition, structure and hygroscopic properties of the particles belonging to a

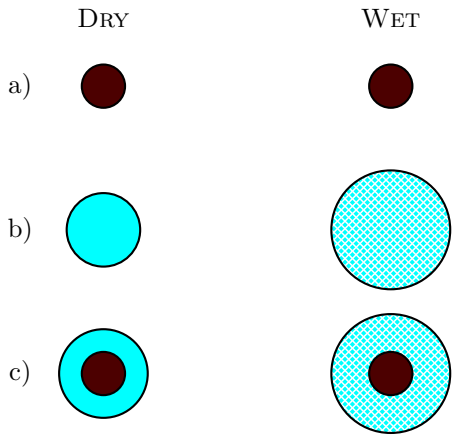


Figure 4: Schematic representation of different types of aerosol structure: (a) homogeneous structure of water insoluble composition; (b) homogeneous structure of water soluble composition; (c) heterogeneous structure with a water insoluble *core* and a water soluble *shell*.

specific species does not change during the model simulation, the only remaining variables to simulate are the size, number concentration and water content of particles of each species. For each species, this can be done by either simulating the changes of the aerosol number (wet) size distribution (NSD, the number of particles over the particle wet size per volume of air), or by simulating the changes of the aerosol number (dry) mass distribution (NMD, the number of particles over the particle dry mass per volume of air).

The description of the dry composition, structure and hygroscopicity (Appendix B) of the particles belonging to a particular species, and equation (3.8), links together the NSD and the NMD of the species. This makes NSD and NMD two equivalent ways of representing all the size information needed to calculate the aerosol optical properties. The NMD has the advantage over the NSD to remain unaffected to changes of the ambient temperature and relative humidity. On the other hand the NSD is a needed step in the calculation of the aerosol optical properties and sedimentation.

Aerosol optical properties can be calculated from a sectional, modal or moment representation of the aerosol NSD (or NMD). The method of moments proposed by McGraw *et al.* (1995) allows to efficiently calculate aerosol optical properties from the lower-order moments of an aerosol NSD. Unfortunately in the case of the aerosol backscattering coefficient, this method can lead to errors as high as 44%. The advantage of a sectional over a modal representation of the NSD (or NMD), is that it allows a better size resolution of the description of the aerosol composition

(Zhang *et al.*, 1999), and therefore a more accurate representation of the aerosol optical properties.

The sectional representation of the aerosol NSD (or NMD) is often selected (e.g. Debry and Sportisse, 2007; Koo *et al.*, 2003; von Salzen and Schlünzen, 1999a,b; Warren and Seinfeld, 1985; Zhang *et al.*, 1999) because of its accuracy on the representation of the aerosol NSD and composition, as well as the different processes that affect the NSD dynamics. In a sectional representation of the NSD, for each species ($aer$), the wet size spectra is divided in a set of intervals called wet size bins. For a wet size bin ($bin$) of the form $[a_{bin}^{aer}, b_{bin}^{aer}]$, $a_{bin}^{aer}$ and $b_{bin}^{aer}$ represent the lower and upper edges of the size bin. In a similar manner, in a sectional representation of the NMD, the dry mass spectra of each species is divided in a set of intervals called dry mass bins. For a dry mass bin of the form $[p_{bin}^{aer}, q_{bin}^{aer}]$, $p_{bin}^{aer}$ and $q_{bin}^{aer}$ represent the lower and upper edges of the mass bin. Using equation (3.8), an equivalent wet size bin can be calculated as function of the atmospheric temperature and the relative humidity, and the properties that characterise the species (composition, structure and hygroscopic properties). Among the multiple possibilities for a sectional representation of the NSD (or NMD), the following three were considered for the aerosol module:

NSD FIX EDGE SECTIONAL REPRESENTATION: the edges of each wet size bin ($[a_{bin}^{aer}, b_{bin}^{aer}]$) are fixed during the simulation. It has the inconvenience that changes on temperature and relative humidity produce fluxes of particles between neighbouring size bins. Therefore introducing numerical diffusion to the system and smoothing out the NSD, unless a relatively large number of size bins is used (Kim and Seinfeld, 1990; Seigneur *et al.*, 1986).

NSD MOVING EDGE SECTIONAL REPRESENTATION: the edges of the size bins are allowed to move following the changes of the particle size. In accordance with the assumption that all particles in a wet size bin are equal and indistinguishable, all the particles are assumed to remain in the same wet size bin as the edges of the wet size bin moves. Therefore there are no fluxes of particles between neighbouring wet size bins.

NMD FIX EDGE SECTIONAL REPRESENTATION: the edges of each mass bin are fixed during the simulation. However, the equation (3.8) relates the fix edge representation of the NMD with the moving edge representation of the NSD, making them equivalent under the assumption that the dry composition, structure and hygroscopic properties that characterise each species, do not change over the simulation time.

The fix edge representation of the NMD has been selected to respresent the NSD. Taking advantage of its equivalence with the moving edge representation of the

NSD, a look up table was created for wet size dependent values such as the characteristic wet size, density and basic optical properties. This construction will be referred to in the following as the *bin scheme*.

For each species, the *bin scheme* consists of a discretisation of the dry mass spectra (into dry mass bins) and a look up table for variables dependent on the particle size, atmospheric temperature and relative humidity. For a discrete set of temperatures (T) and relative humidities (U), ranged between $0-40[°C]$ and $10-100[\%]$, the edges of the corresponding wet size bins are calculated using equation (3.8), and stored in the look up table. For each dry mass bin (bin) of each species (aer), the characteristic particle dry mass ($m_{bin}^{aer}$) is calculated as the geometrical mean of the edges of the dry mass bin ($\left[p_{bin}^{aer}, q_{bin}^{aer}\right]$), and the characteristic particle radius ($r_{bin}^{aer,T,U}$) is calculated as the geometrical mean of the edges of the corresponding wet size bin ($\left[a_{bin}^{aer,T,U}, b_{bin}^{aer,T,U}\right]$). The characteristic particle density ($\rho_{bin}^{aer,T,U}$) is calculated from the characteristic dry mass and radius. The mean bin extinction and backscattering coefficients ($\alpha_{bin}^{aer,T,U}$ and $\beta_{bin}^{aer,T,U}$) can be calculated assuming that, for each species, the particles are uniformly distributed over each wet size bin. Finally, the principal members of the look up table can be written as:

$$
\begin{aligned}
m_{bin}^{aer} &= \sqrt{p_{bin}^{aer} \quad q_{bin}^{aer}} \\
r_{bin}^{aer,T,U} &= \sqrt{a_{bin}^{aer,T,U}\, b_{bin}^{aer,T,U}} \\
\rho_{bin}^{aer,T,U} &= \rho_w + \left(\rho_{dry}^{aer} - \rho_w\right) \frac{m_{bin}^{aer}}{\frac{4}{3}\pi\rho_{dry}^{aer}} \left(r_{bin}^{aer,T,U}\right)^{-3} \\
\alpha_{bin}^{aer,T,U} &= \frac{1}{b_{bin}^{aer,T,U} - a_{bin}^{aer,T,U}} \int_{a_{bin}^{aer,T,U}}^{b_{bin}^{aer,T,U}} Q_{ext}^{aer}(r_p)\, \pi r_p^2 \, \mathrm{d}\, r_p \\
\beta_{bin}^{aer,T,U} &= \frac{1}{b_{bin}^{aer,T,U} - a_{bin}^{aer,T,U}} \int_{a_{bin}^{aer,T,U}}^{b_{bin}^{aer,T,U}} Q_{bsc}^{aer}(r_p)\, \pi r_p^2 \, \mathrm{d}\, r_p
\end{aligned}
$$

Assuming that the characteristic properties of each species remain constant during the model simulation, the *bin scheme*, originally a fix edge sectional representation of the NMD, is equivalent to a moving edge representation of the NSD, where the particle sizes are only updated for discrete changes of temperature or relative humidity. In the following sections of this work, the wet size bins provided by the *bin scheme* will be referred to as size bins.

## 3.4 GRAVITATIONAL SETTLING

Gravitational Settling represents the falling of the particles due to gravity. Opposite to the gravitational force is the drag force, resulting from the movement of the particle in a viscous fluid (air in this case). The balance of these forces determines the falling (terminal) velocity of the particle or *settling velocity* ($v_s(r_p)$), which under the *Stokes law* regime (Appendix C) can be described by:

$$v_s(r_p) = \frac{2\rho_p(r_p)\, g\, C_c(r_p)}{9\rho_{air}\nu_{air}} r_p^2 \tag{3.12}$$

where $g$ represents the gravitational acceleration, $\rho_p(r_p)$ the particle density. For a more detailed description see Pruppacher and Klett (1978); Seinfeld and Pandis (1998).

In the aerosol module the *Gravitational Settling* (equation (3.12)), is valid under the following main assumptions and simplifications:

- Rigid, spherical particles.
- *Stokes Law* regime: Reynolds number $Re < 0.1$.

SHAPE FACTORS can be included to equation (3.12) to correct against the assumption of "rigid spherical particles" (Dressel, 1985; Scheuch and Heyder, 1990). They relay on experimental information about the particle shape. Rigid spherical particles is a relatively common assumption in aerosol models (e.g. Stier *et al.*, 2005; Upadhyay and Ezekoye, 2006). Due to the lack of information about the shape of the in-situ aerosol, the shape factors are neglected.

THE STOKES LAW REGIME SIMPLIFICATION has negligible effect on the settling velocity for particles in the size range covered by the aerosol module. Figure 5a and 5b shows the Reynolds number for spherical particles of 1.91 $g/cm^3$ density, over particle radius and temperature. Figure 5c shows the corresponding particle settling velocity, while Figure 5d shows the relative error of the settling velocity associated to the *Stokes Law* assumption (equation (C.1)). It can be seen in Figure 5b that particles of radius $\leqslant 12$ $\mu m$ have Reynolds numbers within the *Stokes Law* regime ($\leqslant 0.1$). From Figure 5d it is clear that, for temperatures above 0 $C^\circ$, the *Stokes Law* assumption for particles of radius $\leqslant 15$ $\mu m$ produce an overestimation smaller than 2% of the settling velocity.

THE CORRECTION OF THE *"continuum medium"* ASSUMPTION is represented in equation (3.12) by the *Cunningham correction factor* ($C_c$, Section C.2). Table 2 shows

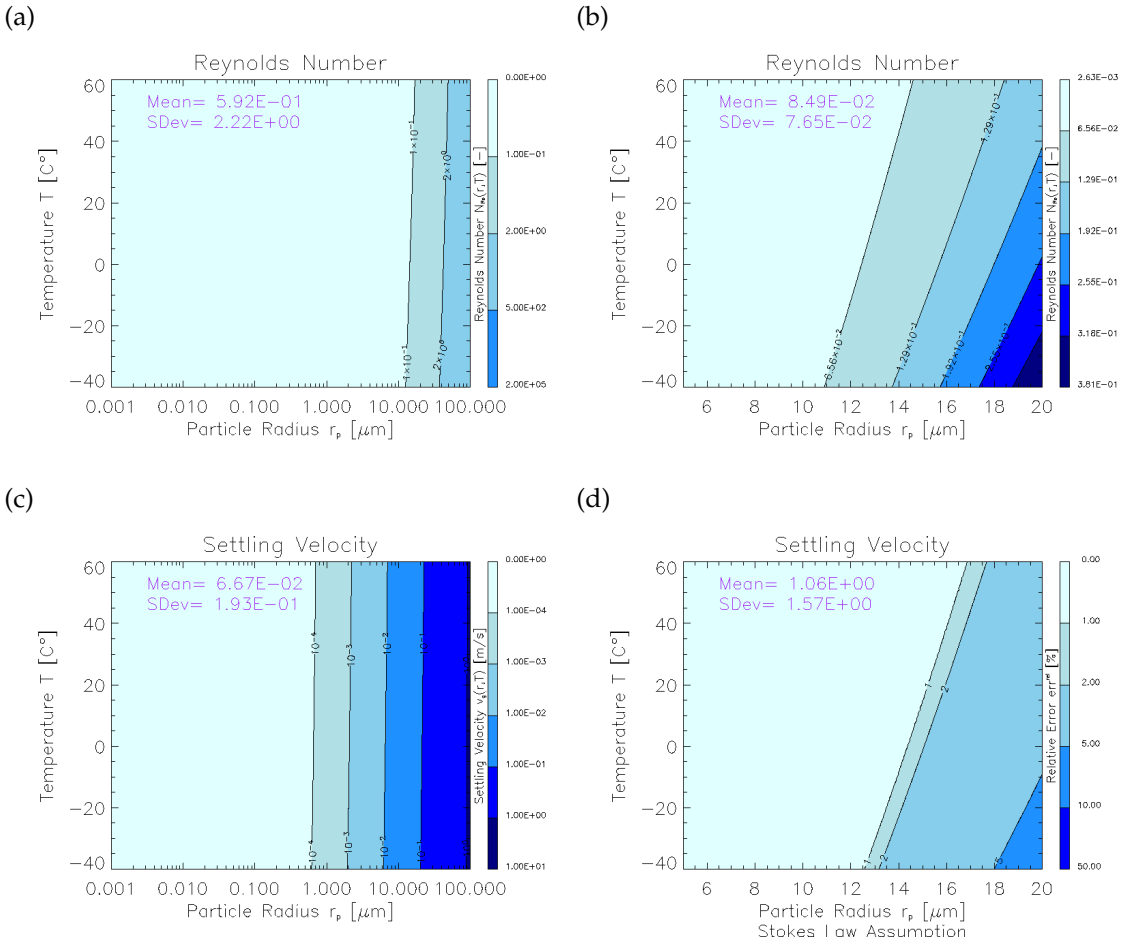


Figure 5: Reynolds number (a,b) particle settling velocity (c) and relative error caused by the *Stokes Law* assumption on the settling velocity (d). Simulated for spherical particles of density 1.91 $g/cm^3$.

the *Cunningham correction factor* over particle aerodynamic diameter ($d_a = 2r_p\sqrt{\rho_p}$). In relative terms, $C_c$ represents an important correction of the settling velocity for small particles, decreasing with increasing particle size until it becomes negligible for large particles. However, one can conclude from Figure 5c and Table 2 that the correction of the settling velocity in absolute terms is not larger than a few $mm/s$, and may be neglected when compared with the vertical wind component. $C_c$ was kept in the final formulation of the *Settling Velocity* (equation (3.12)) only for completeness and consistency with the formulation of the *Brownian diffusivity*. For particles of radius smaller than 2 $\mu m$, Figure 5c shows settling velocities smaller than 1 $mm/s$. For particles of radius bigger than 1.8 $\mu m$ ($d_a \approx 5$ $\mu m$, assuming

1.91 $g/cm^3$ density as in Figure 5), Table 2 shows that the correction introduced by $C_c$ is smaller than 3.2%.

| $d_a[\mu m]$ | 0.1 | 0.2 | 0.5 | 1.0 | 2.0 | 5.0 | 10.0 | 20.0 | 50.0 |
|---|---|---|---|---|---|---|---|---|---|
| $C_c[-]$ | 2.85 | 1.865 | 1.326 | 1.164 | 1.082 | 1.032 | 0.016 | 1.008 | 1.003 |

Table 2: *Cunningham correction factor* ($C_c$), for spherical particles of aerodynamic diameter ($d_a = 2r_p\sqrt{\rho_p}$) in air at 20C°, 1atm. Extract from Seinfeld and Pandis (1998).

VALUES for the settling velocity are pre-calculated for a fixed air density and stored in a look-up table (with aerosol structure, composition, hygroscopicity, particle radius, etc.) and then corrected to include the changes on the air density:

$$v_s(\rho_{air}) = \frac{2\rho_p\, g\, C_c}{9\rho_{air}\nu_{air}} r_p^2 = \frac{2\rho_p\, g\, C_c}{9\rho^*_{air}\nu_{air}} r_p^2 \cdot \frac{\rho^*_{air}}{\rho_{air}} = v_s(\rho^*_{air}) \cdot \frac{\rho^*_{air}}{\rho_{air}}$$

## 3.5 DEPOSITION

*Dry Deposition* is the removal from the atmosphere due to deposition on the ground surface and vegetation cover. This process can be described by the deposition velocity for particles ($v_d(r_p)$), which can be defined following a resistance scheme (Appendix D):

$$v_d(r_p) = \frac{1}{R_a + R_b(r_p) + R_a\, R_b(r_p)\, v_s(r_p)} + v_s(r_p) \tag{3.13}$$

where $R_a$ and $R_b(r_p)$ stands for the aerodynamic transport resistance and the boundary layer resistance for particles of size $r_p$, while $v_s(r_p)$ is the settling velocity given in the equation (3.12). Equation (3.13) describes the deposition velocity under the following assumptions and simplifications:

THE STABILITY DEPENDENT FUNCTION ($\phi_c$, Appendix D) is equal to the stability function for heat: $\phi_c = \phi_h$, following the parametrisation for $\phi_h$ described in Section 2.6 and Chlond (1998a). The usage of $\phi_h$ for aerosol is consistent with the treatment of scalar quantities in the LES model (Chapter 2).

PARTICLES ADHERE to the surface upon contact ($R_c = 0$, Appendix D). This is a common assumption for aerosol particles (Seinfeld and Pandis, 1998), but

obliges to consider particle resuspension separately. The importance of particle emission and resuspension increases with the length of the simulation, as they oppose the effect of deposition on the NSD.

Particle deposition, resuspension and emission are treated in the LES-AOP model by the aerosol surface flux (ASF, Section 3.7.1).

## 3.6 NUMERICAL SOLUTION

Transport and turbulent diffusion follow the parametrisation for scalar quantities of the LES model, described in Chapter 2. For each one of the aerosol fields (one field for each size bin of each species, denoted $n_{bin}^{aer}$), the conservation equation of scalar quantities (Section 2.2, with $\psi_k = n_{bin}^{aer}$) is handled via operator splitting (Section 2.5), dividing the equation into "advection" and "rest" parts. The advection part is solved using Chlond (1994) hybrid scheme. The rest part is solved explicitly using the sub-grid scale (SGS) parametrisation for the SGS fluxes and the SGS eddy coefficient scalar quantities described in Section 2.3. The lateral boundary conditions are described in Section 3.7.2, and surface fluxes in Section 3.7.1.

## 3.7 AEROSOL BOUNDARY CONDITIONS

The basic configuration of the aerosol module follows the LES boundary conditions for scalar quantities (Section 2.6). These boundary conditions (BC) are: zero gradient over the upper boundary ($\Gamma_{top}$); prescribed surface flux over the lower boundary ($\Gamma_{ground}$); and lateral cyclic BC for the lateral boundaries ($\Gamma_{side}$). The lateral boundary can be further divided into the lateral in-flow boundary ($\Gamma_{in}$) and lateral out-flow boundary ($\Gamma_{out}$).

The BC inhereted from the LES parametrisations for scalar quantities, for the number density $n_p$ of particle or radius $r_p$ in a model domain of dimensions $L_x \times L_y \times L_z$, can be summarised as:

$$
\left.
\begin{aligned}
\frac{\partial n_p}{\partial z}(x, y, L_z) &= 0 \\
\frac{\partial^i n_p}{\partial x^i}(0, y, z) &= \frac{\partial^i n_p}{\partial x^i}(L_x, y, z) \\
\frac{\partial^i n_p}{\partial y^i}(x, 0, z) &= \frac{\partial^i n_p}{\partial y^i}(0, L_y, z)
\end{aligned}
\right\} \forall i = 0, 1, \ldots
$$

$$
K_h \frac{\partial n_p}{\partial z}(x, y, 0) = F_3^{n_p}(x, y)
$$

The lateral cyclic BC are of great importance in the LES approach. LES simulations are restricted to a small model domain by its large computational demand. In a small model domain, particle concentration fields would be totally determined by the BC at the lateral in-flow boundary. Lateral cyclic BC provides a way around the problem of finding of a suitable lateral in-flow BC, by assuming horizontal periodicity of the concentration fields. Horizontal periodicity is not applicable in the case of an isolated aerosol source location, as in the days of the PLUS1 measurement campaign simulated in Chapter 5. Suitable cyclic and non-cyclic lateral BC for the aerosol fields are described in Section 3.7.2.

The prescribed aerosol surface flux (ASF, Section 3.7.1) is derived from ground measurements and is a key component of the forcing of the aerosol module. Much care was put into the design of boundary conditions for the aerosol fields, that preserve the heterogeneity generated by the LES part of the model, at high computational cost.

### 3.7.1 *Prescribed Aerosol Surface Flux*

The aerosol surface flux (ASF) account for the emission, deposition and re-suspension of particles from and to the ground surface and its vegetation cover. It represents the lower boundary condition of the LES-AOP model, and links the ground measurements with the model simulation. The forcing of the aerosol module from ground measurements is a key design feature of the aerosol module.

As in the formulation of the dry deposition velocity (Appendix D), for any surface location, the vertical flux of particles is assumed to be constant between the ground surface and the lowermost model mid-level. It is also assumed that this flux can be calculated from the difference between the number concentration at two different levels. For a surface location designed by $(x, y)$, the lowermost model mid-level ($z_r = 10$ m, in this model configuration) and the near-ground level at the same height as the aerosol measurements ($z_g \approx 2$ m), the net particle in-flow ($F_3^{n_p}$) can be written as:

$$F_3^{n_p} = -\frac{n_p^{z_r} - n_p^{z_g}}{R_g} - v_s n_p^{z_r} \tag{3.14}$$

where $n_p^{z_r} = n_p(x, y, z_r, r_p)$ and $n_p^{z_g} = n_p(x, y, z_g, r_p)$ are the number concentration of particles of size $r_p$ at $z_r$ and $z_g$, $R_g = R_g(x, y)$ is the resistance to the transport between $z_r$ and $z_g$, and $v_s = v_s(x, y, z_r, r_p)$ is the gravitational settling velocity at $z_r$, as described in equation (3.12). For simplicity, references to the surface location $(x, y)$ and particle size ($r_p$) will be omitted in the remaining part of this section, unless they are required for clarity.

The formulation of $R_g$ follows almost exactly the formulation for the aerodynamic transport resistance ($R_a$, Appendix D). With only one difference, $R_a$ accounts for the transport between $z_r$ and the roughness length $z_0$, while $R_g$ accounts only for the transport between $z_r$ and $z_g > z_0$. Following the Monin-Obukhov similarity theory:

$$R_g = \frac{1}{\kappa u_*} \int_{z_g}^{z_r} \phi_h \left(\frac{z}{L}\right) \frac{dz}{z} \tag{3.15}$$

where L is the Monin-Obukhov lenght (Section 2.6), and $\phi_h$ is the stability function for heat and all other scalar quantities, defined by equation (2.10) in Section 2.6.

One should notice that equation (3.14), without the settling term, is equivalent to the LES parametrisation of surface fluxes for scalar variables described in Section 2.6, e.g. equations (2.8) and (2.9). Here, the lower limit of the integration is at the height where the aerosol measurement took place ($z_g$), instead of the roughness length ($z_0^h$) as in equation (2.9). Finally, by integrating equation (3.15):

$$R_g = \begin{cases} \frac{1}{\kappa u_*} \left[ \ln\left(\frac{z_r}{z_g}\right) + 9.2 \frac{z_r - z_g}{L} \right] & (\textit{stable}) \\ \frac{1}{\kappa u_*} \ln\left(\frac{z_r}{z_g}\right) & (\textit{neutral}) \\ \frac{1}{\kappa u_*} \left[ \ln\left(\frac{z_r}{z_g}\right) + \ln\left(\frac{(\eta_g+1)^2}{(\eta_r+1)^2}\right) \right] & (\textit{unstable}) \end{cases}$$

where $\eta_r = \sqrt{1 - 12.2\frac{z_r}{L}}$ and $\eta_g = \sqrt{1 - 12.2\frac{z_g}{L}}$.

In a perfect world, aerosol ground measurements would contain information about the NSD and composition in the same horizontal and temporal resolutions as the model. Alas, in reality spatial and temporal resolutions of model and measurements seldom match. The aerosol ground measurements of the PLUS1 measurement campaign (Section 4.4.1), used to initialise and force the LES-AOP model in Chapter 5, are no exceptions. The ground measurements of the two sites (upwind from farm and in the farm plume), have a time resolution much larger than the model time step (hours compared to seconds). Additionaly, in order to provide a suitable lower boundary condition on the model spatial resolution (50 m × 50 m) only two measurement points are not enough. Therefore, further assumptions are needed in order to extend the information derived from the ground measurements to the whole surface of the model domain ($\Gamma_{ground}$).

For an isolated aerosol source location (as in PLUS1), there are two different types of aerosol measurements concerning the ASF, which give rise to two different regimes of particles fluxes. In the source region ($\Gamma_{src}$) and in the background region ($\Gamma_{bgd}$) the net in-flux of particles ($F_{src}^{n_p}$ and $F_{bgd}^{n_p}$) is derived from a representative

value of $n_p^{z_g}$ over each respective region ($n_{src}$ and $n_{bgd}$). The value of $n_{src} = n_{src}(r_p)$ is estimated from measurements of the polluted aerosol, in the source plume. And, $n_{bgd} = n_{bgd}(r_p)$ is estimated from measurements of the background aerosol, outside the source plume, e.g. upwind from the source location.

There is no unique way to extend $n_{src}$ to $\Gamma_{src}$ (or $n_{bgd}$ to $\Gamma_{bgd}$). Assuming that $n_{src}$ represents the spatial average of $n_p^{z_g}$ over $\Gamma_{src}$, and that the horizontal heterogeneities at $z_g$ and $z_r$ are proportional to each other, i.e.:

$$\left\langle n_p^{z_g} \right\rangle_{src} = n_{src}(r_p)$$
$$n_p^{z_g} - \left\langle n_p^{z_g} \right\rangle_{src} = \left( n_p^{z_r} - \left\langle n_p^{z_r} \right\rangle_{src} \right) \alpha_{src}$$

where $\langle \ \rangle_{src}$ denotes the horizontal average over $\Gamma_{src}$, and $\alpha_{src}$ is the proportionality constant. Then the problem of extending $n_{src}$ to $\Gamma_{src}$ is reduced to find an appropriate value for $\alpha_{src}$, e.g.:

- $\alpha_{src} = 0$ then $n_p^{z_g} = \left\langle n_p^{z_g} \right\rangle_{src}$. A constant value of $n_p^{z_g}$ over $\Gamma_{src}$ will unavoidably damp the horizontal heterogeneity of the number concentration near to the ground.
- $\alpha_{src} = 1$ then $n_p^{z_g} = n_p^{z_r} - \left\langle n_p^{z_r} \right\rangle_{src} + \left\langle n_p^{z_g} \right\rangle_{src}$. This is equivalent to assume that the horizontal heterogeneity of the number concentration at $z_g$ and $z_r$ are equal.
- $\alpha_{src} = \frac{\left\langle n_p^{z_g} \right\rangle_{src}}{\left\langle n_p^{z_r} \right\rangle_{src}}$ then $n_p^{z_g} = \frac{\left\langle n_p^{z_g} \right\rangle_{src}}{\left\langle n_p^{z_r} \right\rangle_{src}} n_p^{z_r}$. Therefore, implying that $n_p^{z_g}$ is proportional to $n_p^{z_r}$.

In this work it is assumed that $n_p^{z_g}$ is proportional to $n_p^{z_r}$. Therefore, $n_p^{z_g} = \frac{\left\langle n_p^{z_g} \right\rangle_{src}}{\left\langle n_p^{z_r} \right\rangle_{src}} n_p^{z_r}$. Then, from (3.14), the net particle in-flux for $(x, y) \in \Gamma_{src}$ is:

$$F_{src}^{n_p} = -\frac{\left\langle n_p^{z_r} \right\rangle_{src} - \left\langle n_p^{z_g} \right\rangle_{src}}{R_g \left\langle n_p^{z_r} \right\rangle_{src}} n_p^{z_r} - v_s \, n_p^{z_r} \tag{3.16}$$

During the early testing of the ASF, $F_{bgd}^{n_p}$ was calculated in an equivalent way as $F_{src}^{n_p}$. The tests for background aerosol only (no source region) showed a steady unrealistic decrease of the particle number concentration during the whole model simulation. It was attributed to an over representation of the gravitational settling in the net flux when compared to the emission and re-suspension processes. This tendency was reduced, but not totally eliminated (discussion in Section 5.2), by

neglecting the gravitational settling term in equation (3.14) during the calculation of $F_{bgd}^{n_p}$. Finally, the expression for $F_{bgd}^{n_p}$ over $\Gamma_{bgd}$ is:

$$F_{bgd}^{n_p} = -\frac{\left\langle n_p^{z_r} \right\rangle_{bgd} - \left\langle n_p^{z_g} \right\rangle_{bgd}}{R_g \left\langle n_p^{z_r} \right\rangle_{bgd}} n_p^{z_r} \tag{3.17}$$

If no measurement information is provided ($\Gamma_{bgd}$ and $\Gamma_{src}$ are empty), the ASF is configured to neglect particle emission and re-suspension, and accounting only for the dry deposition flux $F_{dep}^{n_p} = -v_d\, n_p^{z_r}$. In the presence of measurement information, the background region is assumed to be the complement of the source region ($\Gamma_{bgd} = \Gamma_{ground} \backslash \Gamma_{src}$). And, if the area of the aerosol source $\Gamma_{src}$ is not larger than the area corresponding to one grid point, $F_{src}^{n_p}$ can be calculated directly from (3.14), without the need of averaging over $\Gamma_{src}$. Finally, the formulation of the ASF can be summarised by:

$$F_3^{n_p} = \begin{cases} F_{src}^{n_p} & \text{for } (x, y) \in \Gamma_{src} \\ F_{bgd}^{n_p} & \text{for } (x, y) \in \Gamma_{bgd} \\ F_{dep}^{n_p} & \text{otherwise} \end{cases} \tag{3.18}$$

### 3.7.2 *Cyclic and Non-cyclic Lateral Boundary Conditions*

The lateral cyclic boundary conditions are key elements of the design of the LES model (Section 2.6). In the case of an isolated aerosol source location, the selection of suitable lateral in-flow BC represent a big challenge. The high computational demand of the LES approach limits the size of the model domain, making the extention of the model domain to a size large enough to assume independence of the lateral BC practically impossible.

Four different alternatives for providing lateral BC in the case of an isolated aerosol source location were investigated, and will be described in the following parts of this section using the following terminology:

BACKGROUND aerosol fields (BGD) as the set of aerosol fields obtained with only background aerosol ($\Gamma_{bgd} = \Gamma_{ground}$).

POLLUTED aerosol fields (POL) as the set of aerosol fields obtained when both background and isolated source information are fed into the ASF ($\Gamma_{ground} = \Gamma_{bgd} \cup \Gamma_{src}$).

EMITTED aerosol fields (EMS) as the set of aerosol fields obtained when only the difference between background and source flux is taken into account ($F_{ems}^{n_p} = F_3^{n_p} - F_{bgd}^{n_p}$).

SOURCE CONTRIBUTED aerosol fields (DFF) as the set of aerosol fields obtained as the difference between POL and BGD aerosols.

In order to compare model results with measurements, POL fields will be needed. In order to study the structure of the source plume, DFF fields (and therefore BGD fields) will be needed. It should be noted that DFF and EMS do not necessarily coincide. The number concentration of BGD, POL, EMS and DFF aerosol fields will be referred to as $n_p^{bgd}$, $n_p^{pol}$, $n_p^{ems}$ and $n_p^{dff}$ respectively. Specific mention to the aerosol specie ($aer$) and size bin ($bin$) will be omitted.

As BGD do not include information from the aerosol source there is no need to deviate from the lateral cyclic BC. Then, the BC for BGD are:

$$\begin{aligned}
\frac{\partial n_p^{bgd}}{\partial z} &= 0 && \text{at } \Gamma_{top} \\
\left.\begin{aligned}
\frac{\partial^i n_p^{bgd}}{\partial x^i}(0,y,z) &= \frac{\partial^i n_p^{bgd}}{\partial x^i}(L_x,y,z) \\
\frac{\partial^i n_p^{bgd}}{\partial y^i}(x,0,z) &= \frac{\partial^i n_p^{bgd}}{\partial x^i}(x,L_y,z)
\end{aligned}\right\} & \quad \forall i = 0,1,\ldots \text{ at } \Gamma_{side} \\
K_h \frac{\partial n_p^{bgd}}{\partial z} &= F_{bgd}^{n_p} && \text{at } \Gamma_{ground}
\end{aligned} \tag{3.19}$$

*Additive Solution*

Under this configuration, it is assumed that all fluxes between bins are neglectable, and that the freshly emitted and background aerosols do not interact with each other. Then, the farm POL fields can be obtained as the sum of BGD and EMS fields, i.e.:

$$\begin{aligned}
n_p^{src} &= n_p^{bgd} + n_p^{dff} \\
n_p^{dff} &= n_p^{ems}
\end{aligned}$$

The BC for $n_p^{bgd}$ are described by equation (3.19) and the BC for $n_p^{ems}$ are:

$$\begin{aligned}
\frac{\partial n_p^{ems}}{\partial z} &= 0 && \text{at } \Gamma_{top} \\
n_p^{ems} &= 0 && \text{at } \Gamma_{in} \\
\frac{\partial n_p^{dff}}{\partial \Gamma_{out}} &= 0 && \text{at } \Gamma_{out} \\
K_h \frac{\partial n_p^{ems}}{\partial z} &= F_3^{n_p} - F_{bgd}^{n_p} && \text{at } \Gamma_{ground}
\end{aligned}$$

The advection of the EMS fields, which are mostly zero, resulted to be numerically unstable. The source of the instability was not found. Therefore, this option was abandoned.

*Boundary Recycling from Internal Domain*

Given a dominant wind direction, the in-flow BC can be obtained from the interior of the model domain, upwind from the source. Additionally, the lateral in-flow boundary ($\Gamma_{in}$) should be uncorrelated to the vertical cross-section at the interior of the model domain from where the in-flow BC was obtained. This condition can only be verified a-posteriori. Examples of similar methods can be found in the literature under the name of *boundary recycling*, e.g. Mayor *et al.* (2002).

For simplicity, lets assume that the dominant wind direction coincide with the positive direction of the $x$ axis, i.e. $u \gg |v|$, and that the source is located at $x > L_x/2$. Then, the BC at $y = 0$ and $y = L_y$ can be assumed to be periodic. And, the BC at $x = 0$ can be obtained from the vertical cross section at $x = L_x/2$. Thus effectively dividing the model domain into two sub-regions, the background or recycling sub-region ($x \leqslant L_x/2$) and the emission sub-region ($x > L_x/2$). Then, the BC for $n_p^{pol}$ are:

$$
\begin{aligned}
\frac{\partial n_p^{pol}}{\partial z} &= 0 && \text{at } \Gamma_{top} \\
\left.\begin{aligned}
\frac{\partial^i n_p^{pol}}{\partial x^i}(0,y,z) &= \frac{\partial^i n_p^{pol}}{\partial x^i}(L_x/2,y,z) \\
\frac{\partial n_p^{pol}}{\partial x}(L_x,y,z) &= 0 \\
n_p^{pol}(x,0,z) &= n_p^{pol}(x,L_y,z)
\end{aligned}\right\} & && \begin{aligned} &\forall i = 0,1,\ldots \\ &\text{at } \Gamma_{side} \end{aligned} \\
K_h \frac{\partial n_p^{pol}}{\partial z} &= F_3^{n_p} && \text{at } \Gamma_{ground}
\end{aligned}
$$

Under this configuration, there is no need for a separate model simulation to obtain the BGD fields, as they can be extracted from the background sub-region of POL fields. For $x \leqslant L_x/2$ the BGD and DFF fields can be defined as:

$$
\begin{aligned}
n_p^{bgd}(x,y,z) &= n_p^{pol}(x,y,z) \\
n_p^{dff}(x,y,z) &= n_p^{pol}(x + L_x/2,y,z) - n_p^{pol}(x,y,z)
\end{aligned}
$$

Unfortunately, all attempts to force the LES model to show dominant wind direction failed. Thus making this method inapplicable.

*Boundary Recycling from a Unit Field*

Under this configuration, it is assumed that only the total particle number varies in time and space, while the shape of the size distribution and the dry composition remains constant. By neglecting all size dependent processes but water uptake which is inbuilt in the bin scheme, the background aerosol can be represented as:

$$n_p^{bgd}(x,y,z,r_p) = n_1^{bgd}(x,y,z)\, n_{bgd}(r_p) \tag{3.20}$$

The BC for $n_1^{bgd}$ are:

$$\begin{aligned}
\frac{\partial n_1^{bgd}}{\partial z} &= 0 && \text{at } \Gamma_{top} \\
\left.\begin{aligned}
\frac{\partial^i n_1^{bgd}}{\partial x^i}(0,y,z) &= \frac{\partial^i n_1^{bgd}}{\partial x^i}(L_x/2,y,z) \\
\frac{\partial^i n_1^{bgd}}{\partial y^i}(x,0,z) &= \frac{\partial^i n_1^{bgd}}{\partial y^i}(x,L_y/2,z)
\end{aligned}\right\} & \quad \forall i = 0,1,\ldots \text{ at } \Gamma_{side} \\
K_h \frac{\partial n_1^{bgd}}{\partial z} &= F_{bgd}^{n_1} && \text{at } \Gamma_{ground}
\end{aligned}$$

where $F_{bgd}^{n_1}$ follows equation (3.17) for $\left\langle n_1^{z_g} \right\rangle_{bgd} = 1$. Then, the BC for $n_p^{pol}$ are:

$$\begin{aligned}
\frac{\partial n_p^{pol}}{\partial z} &= 0 && && \text{at } \Gamma_{top} \\
\frac{\partial^i n_p^{pol}}{\partial {\Gamma_{in}}^i} &= \frac{\partial^i n_1^{bgd}}{\partial {\Gamma_{in}}^i}\, n_{bgd}(r_p) && \forall i = 0,1,\ldots && \text{at } \Gamma_{in} \\
\frac{\partial n_p^{pol}}{\partial \Gamma_{out}} &= 0 && && \text{at } \Gamma_{out} \\
K_h \frac{\partial n_p^{pol}}{\partial z} &= F_3^{n_p} && && \text{at } \Gamma_{ground}
\end{aligned}$$

This is a very efficient option regarding the computational cost of the generation of suitable BC for the POL fields. The in-flow BC for all POL fields are generated by simulating only one extra field (the unit field $n_1^{bgd}$). However, the BGD fields obtained from equation (3.20) may be oversimplified. And, if a separate simulation is needed it may be cheaper to take the in-flow BC for POL from a "full" BGD simulation. This option is described by the next solution.

*Boundary Recycling from Background Aerosol Fields*

This is the most complete of the solutions. Similar to the previous one, but with a full set of $n_p^{bgd}$ instead of only one. The BC for $n_p^{bgd}$ are described by equation (3.19) and the BC for $n_p^{pol}$ are:

$$\begin{aligned}
\frac{\partial n_p^{pol}}{\partial z} &= 0 && \text{at } \Gamma_{top} \\
\frac{\partial^i n_p^{pol}}{\partial {\Gamma_{in}}^i} &= \frac{\partial^i n_p^{bgd}}{\partial {\Gamma_{in}}^i} \quad \forall i = 0, 1, \ldots && \text{at } \Gamma_{in} \\
\frac{\partial n_p^{pol}}{\partial \Gamma_{out}} &= 0 && \text{at } \Gamma_{out} \\
K_h \frac{\partial n_p^{pol}}{\partial z} &= F_3^{n_p} && \text{at } \Gamma_{ground}
\end{aligned}$$

As the background aerosol is constantly recirculating, this parametrisation provides the most complete background characterisation and most complete lateral in-flow BC for the polluted aerosol. This is the selected option for the model simulations in Chapter 5.

During the testing phase of the boundary recycling schemes, unphysical oscillations where observed on the out-flow boundary. These where caused by the third order flux scheme part (Bott, 1989a,b) of the hybrid advection scheme (Chlond, 1994). In order to avoid the oscillations, the hybrid advection scheme was modified and set to follow its exponential upwind scheme part (Spalding, 1972) on all boundaries.

## 3.8 INITIALISATION AND FORCING

Initial condition of the aerosol fields, as well as of the BC, have a strong influence on the result of the model simulations. This is the case specially in the lateral cyclic boundary and the boundary recycling schemes described in Section 3.7.2, as they will previal in time due to the recycling mechanism.

In the aerosol module of the LES-AOP model, initial condition and forcing are derived from ground measurements, as a key design feature. The forcing of the aerosol fields is prescribed through the aerosol surface flux (ASF), described in Section 3.7.1. This section will focus on the general description of the ground measurements, the near-ground NSD derived from them, and the initial conditions for the aerosol fields. An application of this method can be found in Section 5.1.

As previously stated, it is assumed that, for each species (aer), particles are uniformly distributed over each size bin (bin), and that particles are indistinguishable beyond the size resolution of the bin scheme (Section 3.3.3). Under

this assumption, at the height where measurements took place ($z_g$), the initial particle number (wet) size distribution ($n^{aer}$), and the measured (dry) mass (wet) size distribution ($m^{aer}$), can be written in terms of the bin characteristic values as follows:

$$n^{aer}(r_p) = \sum_{bin} \mathbb{1}_{[a^{aer}_{bin}, b^{aer}_{bin}]}(r_p)\, n^{aer}_{bin} \tag{3.21}$$

$$m^{aer}(r_p) = \sum_{bin} \mathbb{1}_{[a^{aer}_{bin}, b^{aer}_{bin}]}(r_p)\, m^{aer}_{bin}\, n^{aer}_{bin} \tag{3.22}$$

where $n^{aer}_{bin}$ represents the initial particle number concentration (at $z_g$), and $m^{aer}_{bin}$ the characteristic particle dry mass, and $\mathbb{1}$ is the indicatrix function defined as:

$$\mathbb{1}_{[a,b]}(x) = \begin{cases} 1 & \text{if } a \leqslant x \leqslant b \\ 0 & \text{otherwise} \end{cases}$$

In this framework $n^{aer}_{bin}$ can be estimated from $m^{aer}$. In the LES-AOP model, $m^{aer}$ is described by one of the following characterisations:

LOG-NORMAL DESCRIPTION of the measured mass size distribution, were the mass size distribution is characterised as the sum of log-normal distributions of geometrical mean $\mu_i^{aer}$, geometrical standard deviation $\sigma_i^{aer}$ and total mass $M_i^{aer}$. Then, the measured mass distribution for the $aer$ species can be written as:

$$m^{aer}(r_p)\, d\, r_p = \sum_i \frac{M_i^{aer}\, e^{-\frac{1}{2}\left(\frac{\log_{10} r_p/\mu_i^{aer}}{\log_{10}\sigma_i^{aer}}\right)^2}}{\sqrt{2\pi}\log_{10}\sigma_i^{aer}}\, d\log_{10}(r_p)$$

and the initial number concentration at $z_g$ can be obtained from the following equation:

$$\int_{a^{aer}_{bin}}^{b^{aer}_{bin}} m^{aer}(r_p) d\, r_p = (b^{aer}_{bin} - a^{aer}_{bin})\, m^{aer}_{bin}\, n^{aer}_{bin}$$

CUT-OFF DESCRIPTION of the stages of a cascade impactor, where $M_i^{aer}$ corresponds to the mass accumulated between the stage cut-off aerodynamic diameters $d_i$ (starting with $d_0 = 0$), i.e.:

$$\int_{d_{i-1}}^{d_i} m^{aer}(r_p)\, d\, d_a(r_p) = M_i$$

where $d_a(r_p) = 2r_p\sqrt{\rho_p^{aer}(r_p)}$ is the aerodynamic diameter and $\rho_p^{aer}(r_p)$ is density (in $g/cm^3$) of the particles of radius $r_p$. Distributing $M_i$ evenly

among the size bins covered by the impactor stage, the initial number concentration at $z_g$ can be obtained from:

$$\frac{M_i}{\sum_{bin} \mathbb{1}_{[d_{i-1},d_i]}(d_a(r_{bin}^{aer}))} = (b_{bin}^{aer} - a_{bin}^{aer})\, m_{bin}^{aer}\, n_{bin}^{aer}$$

MIXED DESCRIPTION of the measured mass size distribution is described as the sum (or difference) of log-normal and cut-off descriptions, and the initial number concentration at $z_g$ is calculated accordingly.

Finally, assuming horizontal homogeneity of the initial state, the initial NSD ($n_p$) can be calculated as:

$$n_p(x, y, z, bin, aer, t_0) = \frac{a(z, t_0)}{a(z_g, t_0)}\, n_{bin}^{aer}\, e^{-h/h^{aer}}$$

where $z$ is the height, $a$ the absolute humidity, and $h^{aer}$ the parameter governing the vertical decay of the initial state.

# 4

# MEASUREMENT CAMPAIGN PLUS1

The PLUS1 measurement campaign took place in late summer of 2005 (11–19.09.2005) in the vicinity of a livestock (pig) farm in northern Germany (Mettingen, Westfalen: 52°19.44′ N; 7°8.80′ E; 56 m a.s.l.). The measurement campaign was financed by the *Baden-Württemberg Programm Lebensgrundlage Umwelt und ihre Sicherung* (BWPLUS) as part of the projects number `Z03K23005` and `Z03K23007`. The data and conclusions presented in this section have been previously made available in the project reports (Lammel and Valdebenito B., 2007; Lammel *et al.*, 2005, 2006, 2007, in German), and in Pal (2009); Pal *et al.* (2008); Radlach (2009); Radlach *et al.* (2006, 2008). For more detail, please refer to them and references therein.

## 4.1 CAMPAIGN DESIGN

In order to better understand the observable changes on the aerosol properties near to its source, a single source of aerosol particles was needed to be located and studied. Livestock farming has been shown as a potentially significant aerosol source (Lammel *et al.*, 2004), and the selected farm showed many advantages for the measurement campaign:

- Large number of animals.
- Good accessibility and working area.
- Experience in cooperation with research and monitoring projects.
- No similarly large animal farms in the vicinity.
- Observable from many sides.
- Flat terrain.

The need of a flat terrain comes from the limitations of the LES model, which would not be able to simulate the effects of a complex terrain. To facilitate

the representativeness of the LES model, a set of dry and sunny days where selected, in the hope that high mixing conditions would prevail. Accordingly, no measurements during night or when fully cloud covered where performed.

The stable accommodated 1800 animals (approximately 120 tons of pig under a single roof of approximately 25 m × 60 m, Figure 6). The building was ventilated actively, with output of $9 \pm 2$ m$^3$/s from 2 chimneys separated approximately 30 m from each other. There were no particle filters installed on the chimneys.

(a) (b)

Figure 6: (a) View to northeast, from one of the ground sampling locations, 150 m south-west of the farm. (b) View to south, from the lidar location, 480 m north the farm.

## 4.2 EXPERIMENTAL SETUP

During the measurement campaign (11.–19.09.2005) different instruments were employed to characterise the background aerosol and its change downwind, near to the source (1–2 km). Measurements concentrated on three days (15.–17.09.2005) when the weather conditions were favourable for a later LES simulation and the wind direction was in agreement with the single source requirement.

The UHOH scanning aerosol lidar system was used to gather 3-dimensional data sets of the aerosol optical properties (Pal, 2009). Weather balloons were launched to characterise the atmospheric conditions (temperature, humidity, wind speed and direction up to 20 km above ground) and a combination of an optical particle counter (OPC), particle collectors (impactor and filters) and trace gas sampler (diffusion-separator or denuder)[1]. The ground sampling locations were

1 Sammler Partisol 2300: $PM_{2.5}$ and $PM_{10}$ filters and the trace gases samplers (denuders).

selected and moved according to the wind direction, in order to generate data sets upwind and downwind from the farm. The downwind locations ranged between 120–900 m from the source (Figure 7).

During the intensive 3-days measurement period (15.–17.09.05):

1. more than 800.000 single lidar profiles were acquired by the UHOH scanning aerosol lidar system (Pal, 2009) (Section 4.4.2),
2. 8 meteorological radio-sounds were launched[2] (Table 3 and Figure 9),
3. extensive in-situ aerosol and trace gases measurements was performed, collecting:
   - 2 mass and ion-mass distributions of the upwind aerosol[3] (9 particle size classes, Table 5).
   - 6 particle size resolved element concentrations[4] (2 downwind and 4 upwind, Table 5).
   - 25 size resolved particle number concentration measurements[5] (12 downwind and 13 upwind, Table 4),
   - 4 ammonia and nitric acid concentration measurements[6] (2 downwind and 2 downwind, Table 6).
   - 14 size resolved aerosol type classifications[7] (6 downwind and 8 upwind, semi-quantitative, Table 7).

2 Weather balloons with Väisälä RS92-SGP radio-sounds.

3 Berner cascade impactor, gravimetry and ion chromatography. The gravimetric analysis was perfromed by Prof. Dr. Lammel (MPI-MET), and the ion chromatography was performed by G. Ganzlin (Institute of Food Chemistry, UHOH).

4 PM2.5 and PM10 filters, gravimetry, x-ray fluorescent analysis and ion chromatography. The gravimetric analysis was perfromed by Prof. Dr. G. Lammel, the x-ray fluorescent analysis was perfromed by Dr. V. Cercasov (IPM), and the ion chromatography was performed by G. Ganzlin.

5 Optical Particle Counter (OPC), GRIMM 1108, provided by IPM; 15 channels for aerodynamic diameter $> 0.23$ µm.

6 Denuder and ion chromatography. The denuder elution was performed by Prof. Dr. G. Lammel, and the ion chromatography was performed by G. Ganzlin.

7 Laser Ablation Micro Mass Analyzer (LAMMA): mini cascade impactors, electron-microscope and laser mass spectroscopy analysis, performed by Prof. Dr. R. Wurster (IPM).

(a)

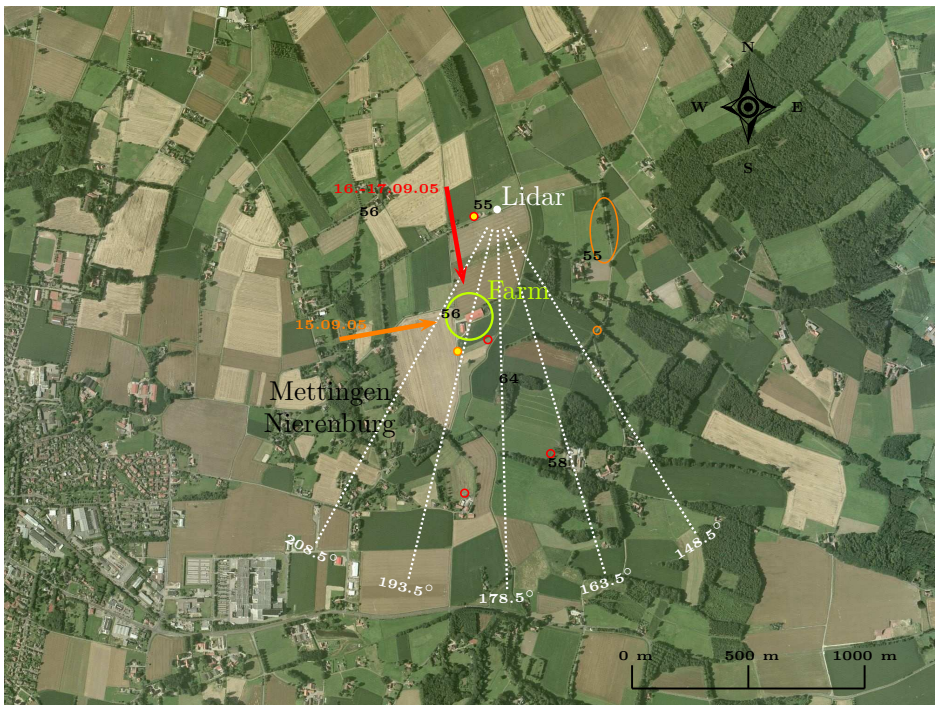


(b)


(c)


(d)

(e)

(f)

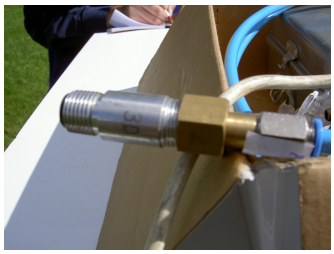

(g)

Figure 7: Field experiment configuration, PLUS1 measurement campaign, intensive measurement period 15.–17.09.05.
(a) Locations of the pig house (large green circle), UHOH scanning aerosol lidar system, sampling locations (upwind: yellow, downwind: red and orange); wind direction (arrows) and lidar PPI scanning pattern (white radii and azimuth angles). (b) UHOH scanning aerosol lidar system. (c) GRIMM optical particle counter (OPC). (d) Weather balloons. (e) Berner cascade impactor with 9 stages between 0.03–16 µm aerodynamic diameter. (f) Mini cascade impactor for single particle analysis (LAMMA) of IPM. (g) $PM_{2.5}$, $PM_{10}$ and denuder. Figure (a) based on image from Pal (2009), satellite image ©GeoContent GmbH (www.geocontent.de). Figure (b) from Pal (2009).

## 4.3 METEOROLOGICAL SITUATION

During the measurement campaign, two different air masses were investigated:

12.–15.09.05: Contaminated air which was advected from west, moist and cloudy, under a low pressure (low 'Takashi' Figure 8).

16.–18.09.05: Maritime background which was air advected from north, dry and sunny under a high pressure (high 'Katja' Figure 8).

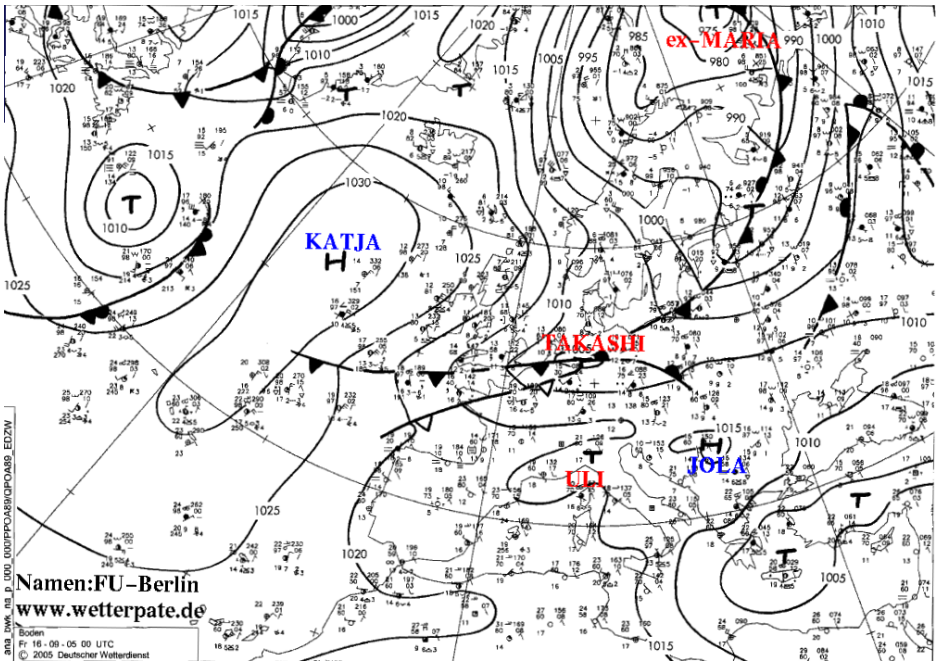


Figure 8: Weather situation on 16.09.05 at 00:00 UTC: Replacement of cyclonic by anticyclonic influence ('Takashi' and 'Katja' respectively). Image from the Institute of Meteorology of the Free University of Berlin (www.wetterpate.de).

The radio-soundings showed a clear difference in the humidity of the two air masses (1000 m above ground, Table 3 and Figure 9). Cloud cover also showed a clear distinction, the first air mass is almost fully covered, while the second has a clear sky to scatterly covered. From the 15.09.05 to the 16.09.05 temperature near the ground drops between three and four degrees for time matching radio-soundings (Table 3). Wind direction was predominantly west with a windspeed up to 15 m/s in the lowermost 2 km on the 15.09.05, while on the 17.09.05 the predominant wind direction was north with wind speeds up to 8 m/s (Figure 9).

The different air masses further differentiate in aerosol number concentrations. The first shows a relatively high number concentration, while the second

| Starting | | Near the ground (60 m) | | | | | 1000 m above the ground | | | | |
|---|---|---|---|---|---|---|---|---|---|---|---|
| Time | CC | p | T | RH | DD | FF | p | T | RH | DD | FF |
| [UTC] | [–] | [hPa] | [°C] | [%] | [°] | [m/s] | [hPa] | [°C] | [%] | [°] | [m/s] |
| 15.09 09:06 | 8/8 | 1010.0 | 18.5 | 73 | 186 | 0.6 | 895.9 | 8.9 | 96 | 272 | 14.7 |
| 15.09 11:50 | 7/8 | 1008.5 | 18.0 | 72 | 290 | 2.3 | 895.0 | 10.1 | 84 | 269 | 13.6 |
| 15.09 14:12 | 8/8 | 1006.3 | 17.0 | 76 | 260 | 1.1 | 892.9 | 9.2 | 97 | 281 | 13.6 |
| 16.09 11:43 | 4/8 | 1002.4 | 14.5 | 61 | 290 | 2.9 | 888.1 | 4.6 | 73 | 344 | 10.7 |
| 16.09 15:10 | 1/8 | 1003.4 | 12.9 | 72 | 360 | 2.7 | 888.7 | 4.7 | 79 | 349 | 12.9 |
| 17.09 07:29 | 0/8 | 1013.2 | 9.8 | 75 | 260 | 1.4 | 896.6 | 3.0 | 75 | 344 | 7.0 |
| 17.09 11:41 | 2/8 | 1014.5 | 14.4 | 50 | 320 | 2.3 | 898.5 | 3.8 | 89 | 327 | 4.6 |
| 17.09 14:54 | 3/8 | 1015.0 | 13.3 | 63 | 290 | 2.0 | 899.3 | 4.6 | 79 | 340 | 4.4 |

Table 3: Results and observations during the the radio-sound launches during the intensive measurement period 15.–17.09.05, in Mettingen. Cloud cover (CC), temperature (T), pressure (p), relative humidity (RH), wind direction (DD) and wind speed (FF).

shows a rather small one. Upwind from the farm, the particle number concentration decreased from 160–220 to 5–46 $cm^{-3}$ for particles in the accumulation mode (aerodynamic diameter between 0.3–1 µm, Table 4) and from 1.2–1.6 to 0.4–1.1 $cm^{-3}$ for large particles ($> 1$ µm, Table 4). The particle mass concentration decreased from 120–225 to 24–30 $\mu g/m^3$ ($PM_{10}$, Table 5 upwind sites). The sea-salt increased strongly while the secondary aerosols ($NH_4NO_3$ and $(NH_4)_2SO_4$) decreased drastically (Table 6 upwind sites, and Figure 10a-b compared with Figure 10c-d). The second air mass was clearly less polluted (e.g. $< 10n$ $g/m^3$ of Pb compared with 10–25, Figure 11). An elevated nitric acid concentration in the farm plume (4.5 ppbv = 13.1 $\mu g/m^3$, Table 6) in the afternoon of the 16.09.05 remains unexplained, this might indicate an sporadic upwind source of $NO_x$ pollution.

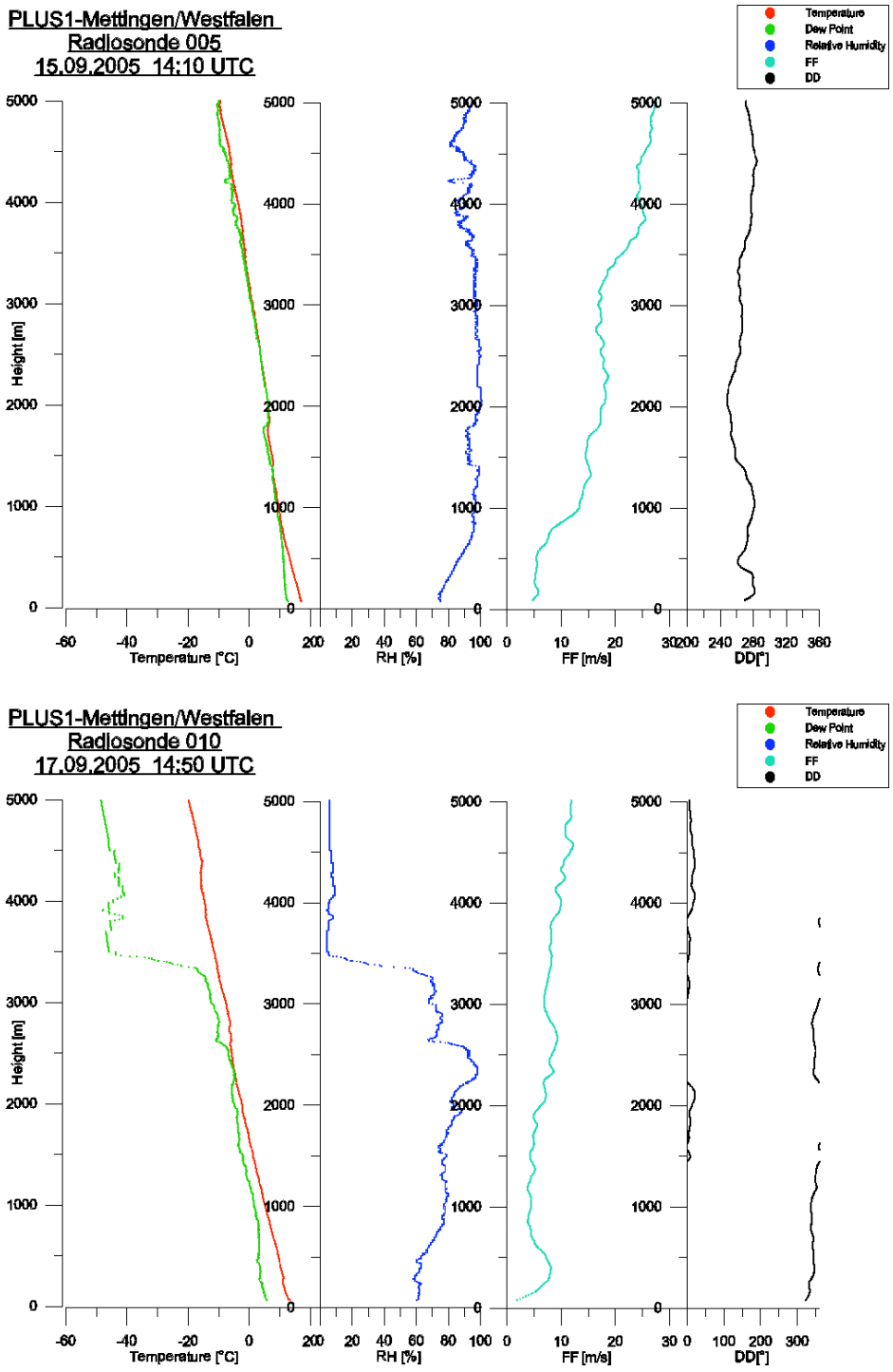


Figure 9: Afternoon radiosound launches, Mettingen 15.–17.09.05.
Vertical profiles from ground to 5000 m for temperature, dew point, relative humidity, wind velocity and wind direction.

## 4.4 RESULTS FROM MEASUREMENT CAMPAIGN

### 4.4.1 *Ground Measurements*

Several hundred meters downwind from the farm the accumulation mode (aerodynamic diameter between 0.3–1 μm, Table 4) showed an increased particle number concentration compared with the upwind values. This increase was not found at short distances downwind from the farm ($\Delta s = 120$ m), instead the number concentration was sometimes smaller. For large particles (aerodynamic diameter $> 1$ μm, Table 4) no significant difference was observed between upwind and downwind sites. In the afternoon of 16.09.05 the farm plume showed, as expected, a strong rise of the ammonia concentration when compared with the upwind level (from 4.3 to 37.7 $\mu g/m^3$ at 120 m downwind from the farm, Table 6). This is an important result, as it illustrates the importance of multiphase processes in the ammonia rich air mass downwind from the farm. Furthermore, it shows the efficiency of these processes on particle formation and growth (in less than 5 min) and its strong selectivity regarding the particle size.

The largest sensitivity to these multiphase processes is shown by the particles in the accumulation mode, which offers the largest (total) particle surface. At short distances downwind from the source, the particle number concentration in accumulation mode did not show any consistent increase or decrease, when compared to the increase observed on measurement points further downwind. This can be explained through the combination of particle formation and phase balance. If the temperature of the downwind air mass is higher compared to the surrounding (or if the moisture is lower), particles can form only after becoming more similar to the surrounding conditions. While the phase balance of the ammonium salt has a high inclination towards particle formation at low temperature (or high moisture). This behaviour was also found in a previous experiment by Lammel *et al.* (2004).

On 16.09.05 and 17.09.05 the background aerosol concentration was low, consisting of sea salt, K and Ca oxides, almost no secondary aerosols and practically no soot particles. The background aerosol concentration levels of the 17.09.05 were even lower than those of the 16.09.05. The measurements in the plume at the ground showed accumulation of organic particulate material, Ca, K, Cl and Fe (Figure 11). In the farm plume N(−III) was in the gas-phase (Table 6). On 16.09.05 the $NH_3$ concentration was distinctly higher than on 17.09.05 (37.7 compared with 4.7 $\mu g/m^3$, Table 6).

*Particle Number and Mass Concentration*

In the afternoon of the 16.09.05, at a short distance downwind from the farm ($\Delta s = 120$ m), the $PM_{2.5}$ mass concentration was approximately 2.4-times higher than the background value (37.2 compared to 15.3 $\mu$ g/m$^3$ at the upwind site, Table 5). Even though the upwind and downwind samples had different collection times, the 5 h overlap was long enough to indicate a mass increase close to the ground. Particle number concentration show little difference between the upwind and the downwind measurement sites ($\approx$ 10 % difference, Table 4).

In the afternoon of the 17.09.05, at a larger distance downwind from the source ($\Delta s = 700$ m), no significant increase of the particle number concentration was observed. One possible explanation is that the farm plume was not close to the ground but at some height above it. A tree-covered hill with small height difference (64 m a.s.l., visible in Figure 7a) between the aerosol source and this downwind measure point may have played an additional role.

*Trace Gases*

In the afternoon of the 16.09.05, the downwind measurement sample show an elevated concentration of nitric acid (4.5 ppbv), which might be an indication of an upwind source of $NO_x$ pollution on that day. Regarding the ammonia concentration, the downwind measurement of 17.09.05 afternoon was not significantly higher than the upwind measurement of 16.09.05 afternoon ($\approx$ 10 % increase, Table 6). Also indicating that the farm plume may have been at some elevation above the ground level.

During the measurement campaign there was a long time measurement of ammonia concentration in air and its deposition flux at the investigated stable made by the LUA[8]. The comparison between LUA and PLUS1 measurements gives plausible results: 55 $\mu$g/m$^3$ during the long time measurement ($\approx$ 20 m downwind from the building chimney), and 37.7 $\mu$g/m$^3$ during the afternoon of the 16.09.05 ($\Delta s = 120$ m downwind from the farm, Table 6).

*Particulate Matter Composition*

The exact mass difference between upwind and downwind particle composition can not be accurately determined. The different detection limits of the different particle collectors (cascade impactor and $PM_{2.5}$–$PM_{10}$ filters) implied different collection times and therefore no simultaneous measurement were performed on the upwind and downwind locations. The simultaneous usage of impactor

8 *Nordrhein-Westfalen Landesamt für Umwelt*: North Rhine-Westphalia Environment Agency

| Sampling | Location | | Concentration [$cm^{-3}$] | |
|---|---|---|---|---|
| Time [UTC] | | $\Delta s$ [m] | $d_a > 0.3$ µm | $d_a > 1.0$ µm |
| 15.09 08:40 | DW | 750–900 | 241 | 1.50 |
| 15.09 09:30 | UW | | 223 | 1.61 |
| 15.09 11:10 | UW | | 164 | 1.39 |
| 15.09 11:10 | DW | 750–900 | 195 | 1.60 |
| 15.09 12:00 | UW | | 198 | 1.51 |
| 15.09 14:30 | UW | | 165 | 1.30 |
| 15.09 14:30 | DW | 600 | 192 | 1.20 |
| 16.09 13:00 | UW | | 9.7 | 1.07 |
| 16.09 13:00 | DW | 120 | 8.5 | 0.80 |
| 16.09 15:30 | UW | | 5.6 | 0.44 |
| 16.09 15:30 | DW | 120 | 5.0 | 0.45 |
| 17.09 08:40 | UW | | 17 | 0.71 |
| 17.09 08:40 | DW | 700 | 40 | 0.98 |
| 17.09 09:00 | DW | 120 | 15 | 0.84 |
| 17.09 09:40 | UW | | 9.1 | 0.72 |
| 17.09 11:00 | DW | 750 | 6.9 | 0.57 |
| 17.09 12:30 | DW | 700 | 5.4 | 0.47 |
| 17.09 14:00 | UW | | 5.1 | 0.42 |
| 17.09 14:00 | DW | 120 | 6.1 | 0.40 |
| 17.09 14:20 | UW | | 4.7 | 0.39 |
| 17.09 16:00 | DW | 700 | 6.1 | 0.29 |
| 17.09 17:20 | UW | | 12 | 0.51 |
| 18.09 09:30 | UW | | 46 | 0.78 |

Table 4: Particle number concentration, Mettingen 15.–17.09.05.
5–10 min averaged number concentration for particles of aerodynamic diameter ($d_a$) $> 0.3$ µm and $> 1.0$ µm. Sampling locations upwind and downwind from source (distance $\Delta s$), Figure 7.

| Sampling | Location | | Concentration [$\mu g/m^3$] | | |
|---|---|---|---|---|---|
| Time [UTC] | | $\Delta s$ [m] | $PM_{2.5}$ | $PM_{10}$ | $PM_{16}$ |
| 13.09 19:00 – 14.09 06:00 | UW | | 248 | 225 | — |
| 13.09 19:00 – 14.09 18:00 | UW[§] | | 69 | 105 | 108 |
| 14.09 08:00 – 14.09 18:00 | UW | | 86.2 | 119 | — |
| 14.09 18:30 – 15.09 17:30 | UW[§] | | 68 | 105 | 114 |
| 14.09 19:00 – 15.09 06:00 | UW | | 124 | 126 | — |
| 15.09 07:00 – 15.09 14:20 | UW | | 69.3 | 156 | — |
| 15.09 19:00 – 16.09 10:00 | UW | | 59.2 | — | — |
| 16.09 10:40 – 16.09 16:00 | DW[†] | 120 | 37.2 | >3.4 | — |
| 16.09 10:00 – 17.09 17:00 | UW[§] | | 15.3 | 24.4 | 25.3 |
| 16.09 16:40 – 17.09 08:00 | UW[†] | | 39.2 | >1.9 | — |
| 17.09 12:25 – 17.09 16:25 | DW | 700–750 | 24.9 | >9.8 | — |
| 17.09 17:00 – 18.09 09:00 | UW | | 36.4 | 30.3 | — |
| 17.09 17:00 – 18.09 09:00 | UW[§] | | 24.1 | 30.2 | 30.2 |

[§] Extrapolated from mass concentration of the particle content of the individual impactor stages (9-stage Berner Impactor) and their total mass:

$PM_{2.5} \approx$ total impactor mass $< 2$ µm (stages 1–6).

$PM_{10} \approx$ total impactor mass $< 8$ µm (stages 1–8).

$PM_{16} \approx$ total impactor mass $< 16$ µm (stages 1–9).

[†] See $PM_{10}$ ions mass.

| Sampling | Location | | Ions mass [$\mu g/m^3$] on $PM_{10}$ | | | | | |
|---|---|---|---|---|---|---|---|---|
| Time [UTC] | | $\Delta s$ [m] | $Na^+$ | $NH_4^+$ | $K^+$ | $Cl^-$ | $NO_3^-$ | $SO_4^{2-}$ |
| 16.09 10:40 – 16.09 16:00 | DW | 120 | 0.53 | 0.17 | 0.04 | 1.35 | 1.12 | 0.16 |
| 16.09 16:40 – 17.09 08:00 | UW | | 0.55 | 0.26 | 0.03 | 0.29 | 0.27 | 0.45 |
| 17.09 12:25 – 17.09 16:25 | DW | 700–750 | 6.16 | 0.04 | 3.08 | 0.40 | 0.04 | 0.06 |

Table 5: Particle mass concentration, Mettingen 15.–17.09.05.
Particulate matter ($PM_{2.5}$, $PM_{10}$ and $PM_{16}$) at 50 % of relative humidity. Sampling locations upwind (UW) and downwind (DW) from source (distance $\Delta s$), Figure 7.

| Sampling | Location | | | | Concentration[§] [$\mu g/m^3$] | |
|---|---|---|---|---|---|---|
| Time [UTC] | | $\Delta s$ [m] | T [°C] | RH [%] | $NH_3/NH_4^+$ | $HNO_3/NO_3^-$ |
| 15.09 07:00 – 15.09 14:20 | UW | | 17–19 | 72–76 | 3.85 / — | 0.49 / — |
| 16.09 10:40 – 16.09 16:00 | DW | 120 | 13–15 | 61–72 | 37.7 / 0.17 | 13.1 / 1.12 |
| 16.09 16:40 – 17.09 08:00 | UW | | 9–13 | 46–>75 | 4.30 / 0.26 | 0.14 / 0.27 |
| 17.09 12:25 – 17.09 16:25 | DW | 700–750 | 13–15 | 50–63 | 4.73 / 0.04 | 1.32 /<0.04 |

[§] $NH_3$ & $NH_4^+$ have oxidation number -3 ($N(-III)$), while $HNO_3$ & $NO_3^-$ have oxidation number 5 ($N(V)$).

Table 6: Gaseous ammonia and nitric acid and corresponding particulate matter ion concentrations, Mettingen 15.–17.09.05. Temperature (T) and relative humidity (RH) are also given. Sampling sites upwind (UW) and downwind (DW) from source (distance $\Delta$ s), Figure 7.

and filters (on the upwind site, from 17.09.05 evening to next morning) give an excellent agreement for the particle mass concentration ($< 0.5$ % difference between PM10 and PM16). Nevertheless, an uncertainty of $\approx 20$ % has to be considered due to sampling issues (Lammel *et al.*, 2007).

The fine particulate matter ($PM_{2.5}$) content of S, Cl, Ca, K, Fe and Ni showed a significant downwind increase (S and K only on the 16.09.05 and Fe only on the 17.09.05). The downwind approximate increase factor (shown in square brackets) of the mass particle phase (as mass mixing ratio in ppm, Figure 11b,d) consisted of: Ca[13], K[2], Cl[7] on the 16.09.05 and K[65], Cl[29], Fe[67] on the 17.09.05. Given the location and surroundings of the farm, it is safe to assume that these increases are due to emission from the farm. There was also an accumulation of Ni, which was not expected as an emission from a pig farm. The downwind increase of the total ion-content was not more than three times larger. Considering the downwind variability of the aerosol composition over time, this does not represent a significant increase. The mass concentration of large particles (aerodynamic diameter $> 2.5$ µm, Table 5) showed no significant difference between upwind and downwind samples.

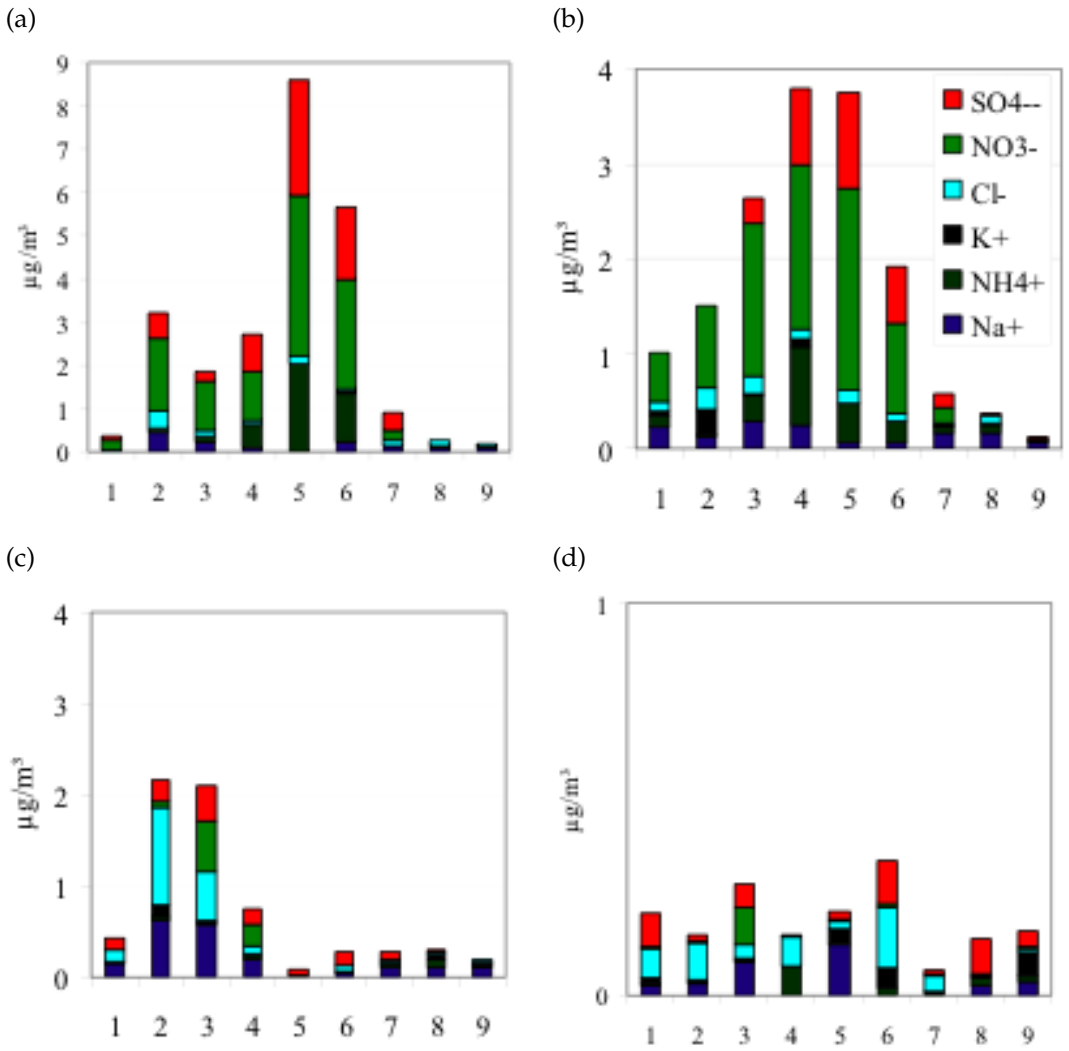


(e)

| Stage | 1 | 2 | 3 | 4 | 5 | 6 | 7 | 8 | 9 |
|---|---|---|---|---|---|---|---|---|---|
| $d_a$ [µm] $\geqslant$ | 0.03 | 0.06 | 0.13 | 0.25 | 0.5 | 1.0 | 2.0 | 4.0 | 8.0 |
| $d_a$ [µm] $\leqslant$ | 0.06 | 0.13 | 0.25 | 0.5 | 1.0 | 2.0 | 4.0 | 8.0 | 16.0 |

Figure 10: Background particle mass size distribution of inorganic ions, Mettingen at: (a) 13.–14.09.05, (b) 14.–15.09.05, (c) 16.–17.09.05, (d) 17.–18.09.05.
Two different air masses were studied (Section 4.3):
(a)–(b) humid and cyclonic air mass advected from west; (c)–(d) dry and anti-cyclonic air mass advected from north. (e) Berner cascade impactor stages and particle size range (aerodynamic diameter $d_a$). Lammel *et al.* (2007).

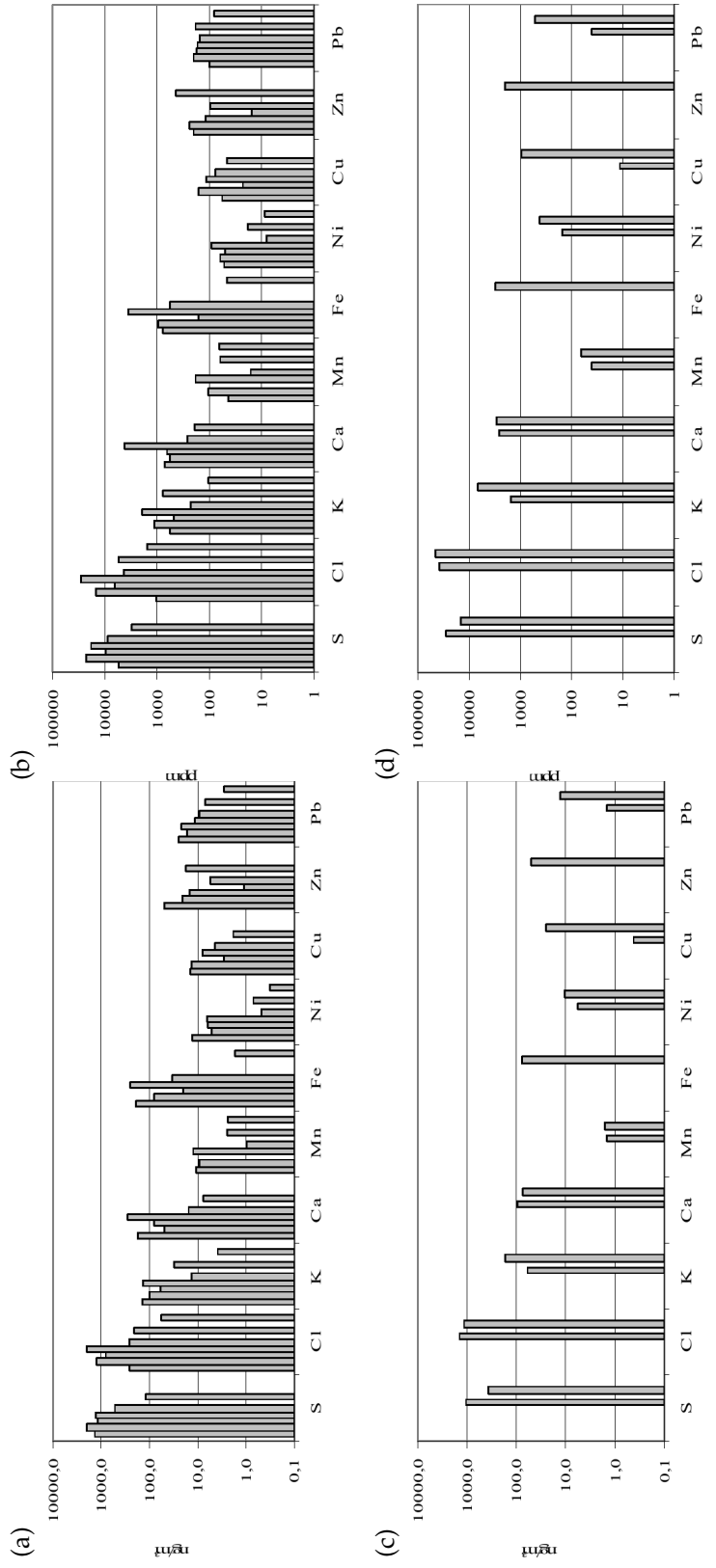


Figure 11: Elemental composition of fine particulate matter ($PM_{2.5}$), Mettingen 15.–18.09.05. Concentration per volume of air (a,c in ng/m$^3$) and mass mixing ratio (b,d in ppm) in subsequent upwind samples (a,b) and downwind samples (c,d). For each element consecutive bars represents subsequent samples, see Table 5 for sampling times of the $PM_{2.5}$ filters. Lammel *et al.* (2007).

*Single particle analyses*

Single particle analysis allows the identification of the aerosol particle types at the particle level. It also allows to assess the degree of mixing and other qualitative information regarding the chemical characteristic. Assumptions about these characteristics are essential for the aerosol module of the LES-AOP model (Section 3.3.2 and Section 3.3.3). An accurate experimental description of the aerosol population at the particle level, would therefore help to improve the representativity of the model simulations. The most important results regarding the single particle analysis are summarised in Table 7, Figure 12 and Figure 13.

The background aerosol consists mainly of chlorides, possible oxides from Na, K, Ca as well as organic carbon (OC). Different particle types where found to contribute to each size class, indicating an at least partially mixed aerosol population. Highly compacted carbon molecules, especially soot particles, were not found. This is in accordance with the fine particle bulk analysis, and confirms the original assumption that the farm location has no influence from traffic or other combustion processes.

Secondary inorganic aerosol (ammonium nitrate and ammonium sulfate) plays a inferior role at the upwind and downwind locations. In the farm plume N(−III) was found mostly in the gas-phase (Table 6).

In the downwind samples of the 17.09.05, in addition to components of the background aerosol, Ca, OC and Fe (uncertain) were found in the particulate phase. Consistently with the fine particle analyse (Figure 11), the farm plume contained sub-micron carbon particles (Figure 12) and super-micron Ca, CaO and $CaSO_4$ particles (Figure 13). Surprisingly the downwind composition of the sub-micron and super-micron particles was rather similar.s Experimental analyses were performed by Prof. Dr. R. Wurster.

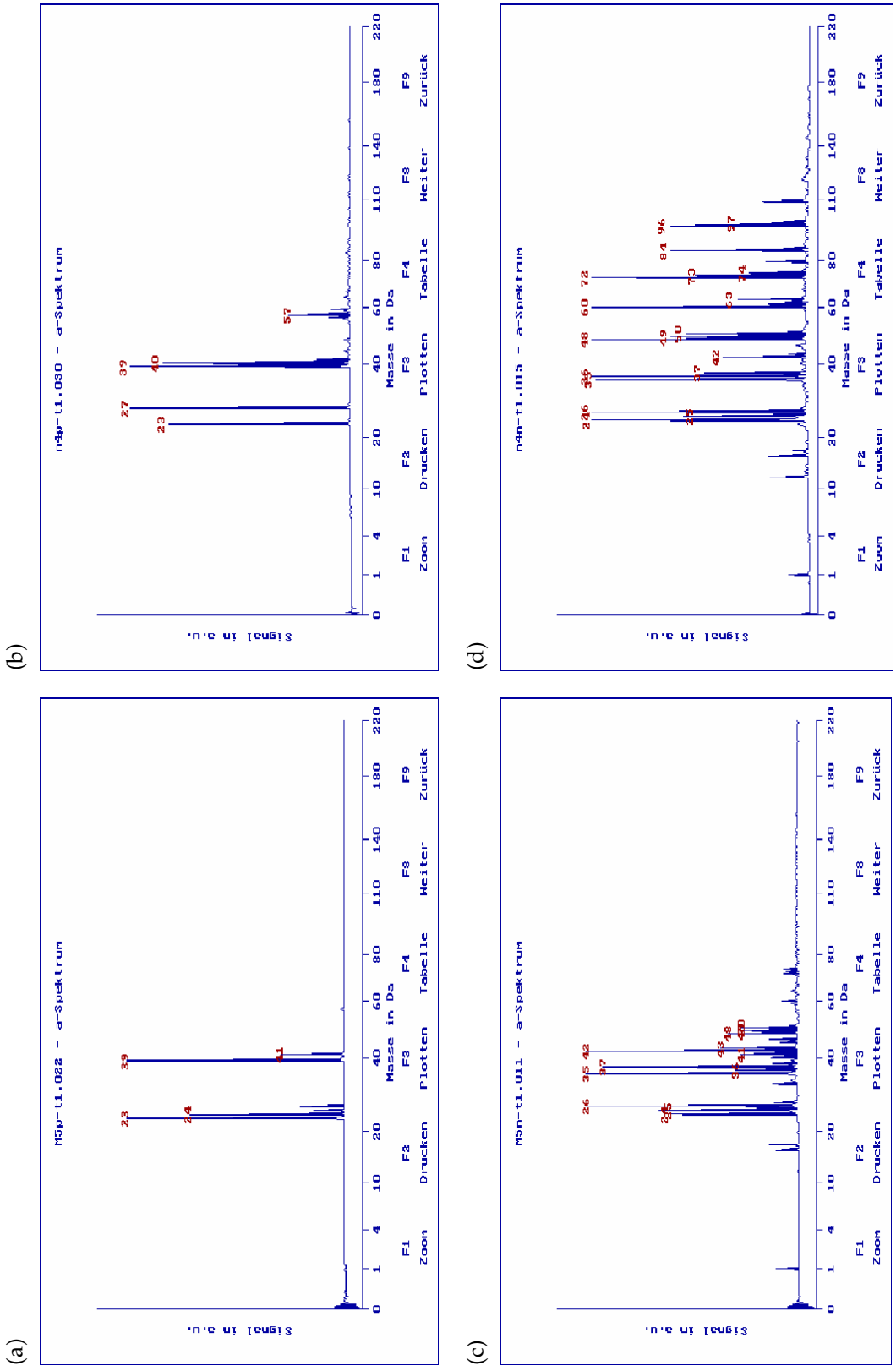


Figure 12: Mass spectra of single particles on the sub-µm range ($d_a = 0.18$–$0.35$ µm), Mettingen 17.09.05. Comparison of typical positive (a,b) and negative (c,d) mass spectra of particles upwind (UW a,c) and downwind (DW, $\Delta s = 750$ m b,d) of the aerosol source. LAMMA results are courtesy of Prof. Dr. R. Wurster, UHOH.

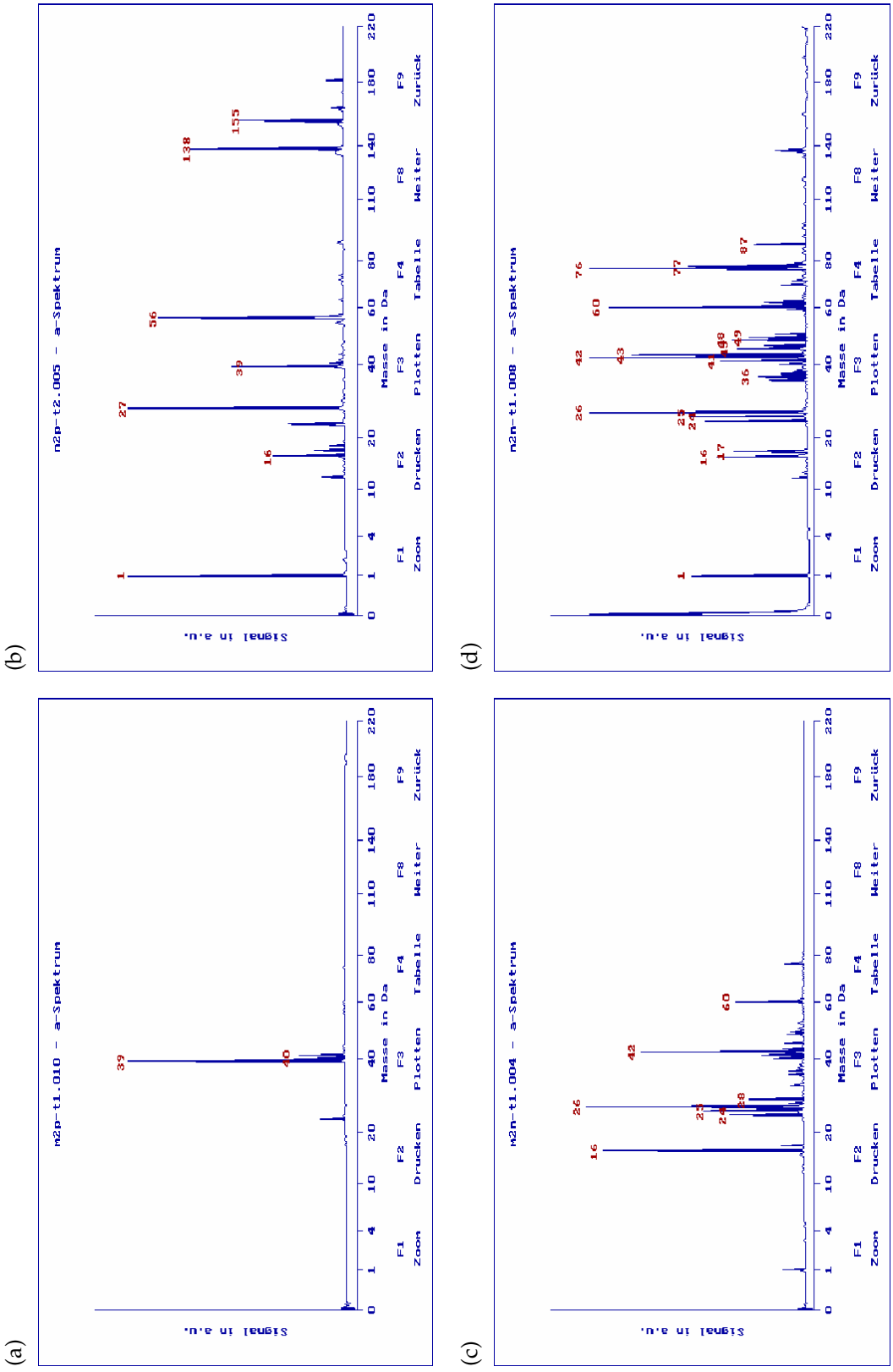


Figure 13: Mass spectra of single particles on the super-µm range ($d_a = 1.2–3.5$ µm), Mettingen 17.09.05. Comparison of typical positive (a,b) and negative (c,d) mass spectra particles upwind (UW a,c) and downwind (DW, $\Delta s = 750$ m b,d) of the aerosol source. LAMMA results are courtesy of Prof. Dr. R. Wurster, UHOH.

| Sampling | Location | | Particle | |
|---|---|---|---|---|
| Time [UTC] | | Δs [m] | $d_a$ [μm] | Mass Spectrometric Fragments[§†] |
| 16.09 15:20 – 16.09 15:25 | DW | 120 | 1.20–3.50 | Na Mg K NaO NO CaO OH $CN/C_2H_2$ Cl CNO $C_3N$ $SiO_2$ (76) |
| 16.09 15:35 – 16.09 15:40 | UW | | 0.18–0.35 | Na (Al) K Fe NaO NO CaO (81 – 83) $C_{4\_8}$ $CN/C_2H_2$ Cl $PO_2$ (87f) CNO $C_3N$ $C_xO$ |
| 17.09 09:00 – 17.09 09:48 | UW | | 0.18–0.35 | Na Al K (Fe) (63) C4_8 $CN/C_2H_2$ Cl CNO $C_3N$ $C_5O$ |
| 17.09 09:00 – 17.09 09:48 | UW | | 1.20–3.50 | Na Mg K NaO NO CaO OH $CN/C_2H_2$ Cl CNO $C_3N$ ($NO_x$,$SO_x$) (93 – 95) |
| 17.09 09:00 – 17.09 09:48 | DW | 120 | 0.18–0.35 | Na K (**Ca**) $CN/C_2H_2$ $C_{4\_5}$ ($HSO_4$) |
| 17.09 09:00 – 17.09 09:48 | DW | 120 | 1.20–3.50 | (Al) Na K (**Ca** Fe CaSO4,**154**[‡]) CN/CH NaCl CNO $\mathbf{C_{4\_6}H_{2\_4}}$,$\mathbf{C_{2\_10}}$ |
| 17.09 10:55 – 17.09 11:01 | DW | 700 | 1.20–3.50 | Na Mg K **Fe** $CaO_2H$ (CaSO4 **154**[‡]) OH $CN/C_2H_2$ NaCl CNO $NaCl_2$ $SO_3$ |
| 17.09 12:25 – 17.09 12:35 | DW | 750 | 0.18–0.35 | Al **Fe** (K **Ca**) ($CaSO_4$ **154**[‡]) $C_{4\_8}$ $CN/C_2H_2$ Cl CNO $C_3N$ $C_5O$ |
| 17.09 12:25 – 17.09 12:35 | DW | 750 | 0.35–0.65 | Na Mg K Ca (**Cu**) CaO CaOH Ca2O $\mathbf{C_{4\_8}}$ $CN/C_2H_2$ Cl CNO C3N $\mathbf{C_{4\_5}O}$ |

[§] Ionic (positive and negative) signs are omitted.

[†] Under ambient air conditions $C_{2\_5}$, $C_{4\_5}$, etc. would correspond tosoot particle fragments.

[‡] CaSO4,**154** is most probably $CaSO_5$,$FeSO_4$.

Table 7: Mass spectrometric fragments in size segregated single particle analyses upwind (UW) and downwind (DW) of the aerosol source (distance Δs), Mettingen 16.–17.09.05. Those found rarely in **bold**, found only downwind in brackets. Numbers denote unidentified fragments (mass in g/mol).

### 4.4.2 *Lidar Measurements*

The lidar system used in the measurement campaign was developed at the Institute for Physics and Meteorology (IPM) of the University of Hohenheim (UHOH). The PLUS1 was the first field campaign for the UHOH scanning aerosol lidar system, and it has been notably improved since. The UHOH scanning aerosol lidar system was developed as part of the Ph.D. work of Pal (2009). Detailed descriptions of the UHOH scanning lidar data analysis techniques can be found in Pal (2009); Pal *et al.* (2006); Radlach *et al.* (2006).

On its PLUS1 configuration the UHOH scanning aerosol lidar system counted with a high power eye-safe laser (Nd:YAG-Laser, wavelength $\lambda = 355$ nm). A fast scanner allows to change the orientation of the laser beam and get 1-D, 2-D or 3-D data sets. It was mounted in a truck for mobility (Figure 7b). On its current configuration it is also capable of measuring in several wavelengths ($\lambda = 355, 532, 1064$ nm). Additionally, a scanning rotational Raman lidar has been developed for the combined measurements of aerosol optical properties and temperature distributions (Radlach, 2009; Radlach *et al.*, 2006). Unfortunately, these were not available at the time of the PLUS1 measurement campaign.

During the measurement campaign there were external conditions which prevented the continuous operation of the lidar system. For example, rain and condensation on the optic elements of the lidar due to high ambient humidity, specially in the evenings and during the night. In addition to this, it is not possible to scan towards certain directions as function of day time, as the sensitive detector can not be exposed to direct sun-radiation. The measurements taken by the UHOH scanning aerosol lidar system are characterised in Table 8. The retrieval procedure of the aerosol backscattering coefficient from the lidar signal is described in Section 4.5.

The 2-D and 3-D lidar data sets are composed of a collection of 1-D lidar data sets (or distance-profiles). Different scanning patterns can be achieved by changing the orientation of the scanner. Detailed descriptions of the different scanning strategies of the UHOH lidar can be found in Pal (2009). The following nomenclature will be used from here on:

RANGE: Distance between the laser pulse and the detector of the lidar system.

ELEVATION ANGLE: Vertical ascending angle from the horizontal level and the lidar beam.

AZIMUTH (OR POLAR) ANGLE: Clockwise angle between the north direction and the horizontal projection of the lidar beam (e.g. the farm relative location to the lidar is 480 m of range and 193.5° of azimuth).

DISTANCE-PROFILE (OR RANGE-PROFILE): describes a linear 1-D scanning pattern, where the azimuth and elevation angles remain constant, while the distance changes continuously. The minimum range is $200 - 300$ m depending on the system configuration and the maximum range is approximately 12 km.

PPI-SCAN (PLANE POLAR INDICATOR): describes a cone-shaped 2-D scanning pattern (Figure 14a). Consecutive distance-profiles are taken during a PPI-Scan with constant elevation angle and continuously changing azimuth angle.

RHI-SCAN (RANGE-HEIGHT INDICATOR): describes a fan-shaped 2-D scanning pattern (Figure 14b). Consecutive distance-profiles are taken during a RHI-Scan with constant azimuth angle and continuously changing elevation angle.

PPI-VOLUMESCAN: is the 3-D extension of the PPI-Scan pattern. Consecutive PPI-Scans are taken during a PPI-Volumescan, where the elevation angle is changed in constant steps between successive PPI-Scans.

RHI-VOLUMESCAN: is the 3-D extension of the RHI-Scan pattern. Consecutive RHI-Scans are taken during a RHI-Volumescan, where the azimuth angle is changed in constant steps between successive RHI-Scans.

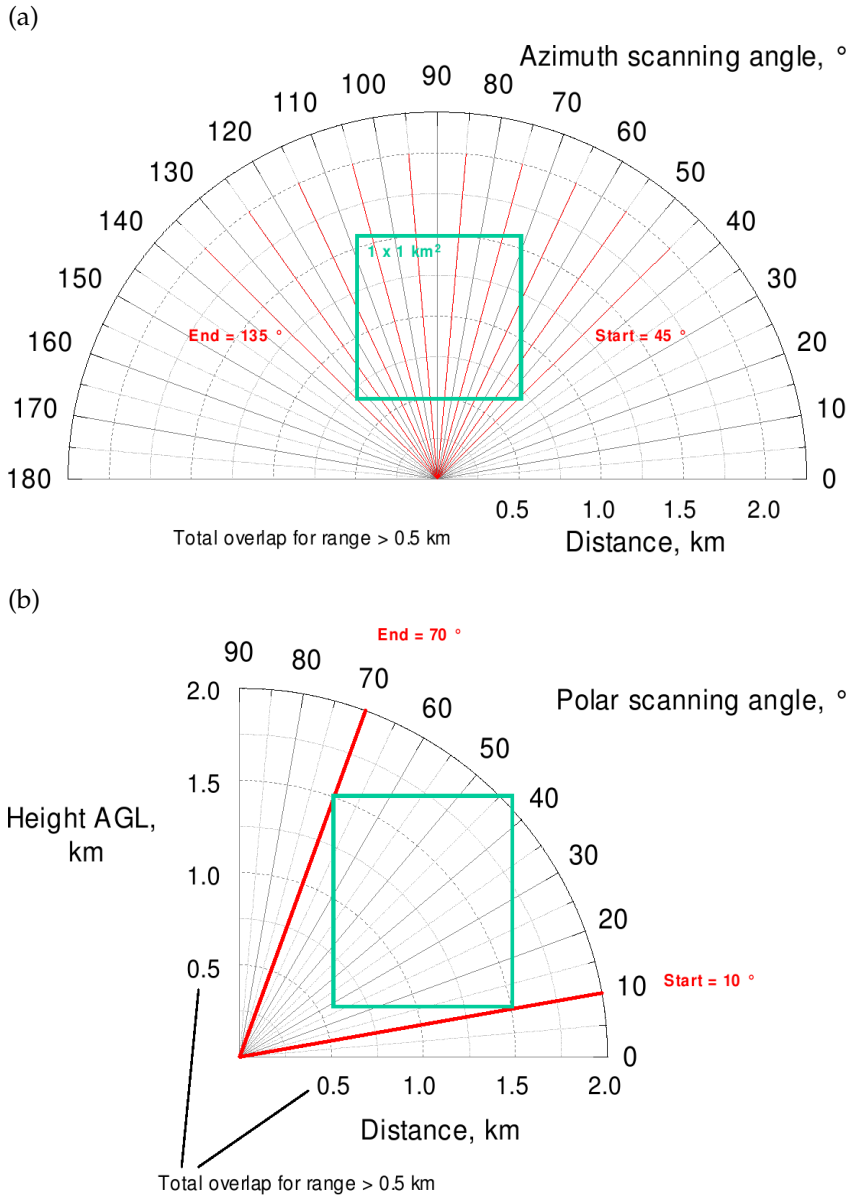


Figure 14: Example of lidar scanning patterns.
(a) PPI-Scan pattern. (b) RHI-Scan pattern. Figures from Pal (2009).

| Sampling Time [UTC] | Scan Type | Azimuth Rel.[§†] [°] | Elevation Rel.[‡] [°] | $\frac{d\measuredangle}{dt}$ [°/s] | $\Delta t$ [s] | $\Delta r$ [m] |
|---|---|---|---|---|---|---|
| 12.09 16:00 – 18:00 | Test | | | | | |
| 13.09 17:00 – 18:00[a] | PPI-Scan | | | 0.1 | 0.33 | 3 |
| 13.09 18:00 – 19:00[a] | PPI-Vol. | 73–78 | 1.5–3 | 0.1 | 0.33 | 3 |
| 15.09 08:30 – 09:00 | RHI-Scan | 60 | 5.5–20 | 0.5 | 0.033 | 3 |
| | RHI-Scan | 20 | 5.5–20 | 0.5 | 0.033 | 3 |
| | RHI-Scan | 60 | 5.5–20 | 5 | 0.033 | 3 |
| 15.09 09:00 – 09:32[b] | RHI-Scan | 60 | 5.5–20 | 0.5 | 0.033 | 3 |
| | RHI-Scan | 20 | 5.5–20 | 0.5 | 0.033 | 3 |
| | RHI-Scan | 60 | 5.5–20 | 5 | 0.033 | 3 |
| 15.09 09:45 – 10:15 | RHI-Vol. | 60–20 | 5–20 | 1 | 0.033 | 3 |
| 15.09 10:30 – 11:00 | RHI-Scan | 60 | 5–20 | — | 0.033 | 3 |
| 16.09 12:20 – 13:45 | RHI-Vol. | 0–70 | 2–30 | 1 | 0.033 | 3 |
| 16.09 13:55 – 14:20 | PPI-Scan | 0–85 | 10 | 1 | 0.033 | 3 |
| 16.09 15:14 – 15:30 | PPI-Scan | -50–85 | 10 | 1 | 0.033 | 3 |
| 16.09 16:40 – 16:50 | PPI-Scan | -40–40 | 5 | 1 | 0.033 | 3 |
| 17.09 09:40 – 10:40 | PPI-Vol. | 0–85 | 5–20 | 0.5 | 0.033 | 3 |
| 17.09 11:00 – 11:30[a] | PPI-Vol. | 73–78 | 2–3.5 | 0.1 | 0.033 | 3 |
| 17.09 11:43 – 12:40 | PPI-Vol. | 0–85 | 5–30 | 0.5 | 0.033 | 3 |
| 17.09 15:45 – 16:15 | PPI-Vol. | 0–80 | 5–20 | 0.5 | 0.033 | 3 |
| 17.09 17:00 – 18:00 | PPI-Vol. | -30–80 | 5–15 | 1 | 0.033 | 3 |
| 18.09 08:30 – 09:30 | PPI-Vol. | -30–85 | 5–20 | 5 | 0.033 | 3 |
| 18.09 09:35 – 10:15 | PPI-Vol. | -10–80 | 5–20 | 5 | 0.033 | 3 |
| 18.09 10:16 – 10:45 | PPI-Vol. | -10–80 | 5–25 | 1 | 0.033 | 3 |
| 18.09 10:45 – 12:15[c] | PPI-Vol. | -10–80 | 5–20 | 0.5 | 0.33 | 3 |
| 18.09 12:50 – 14:00 | RHI-Vol. | -10–85 | 5–25 | 1 | 0.33 | 3 |

| Sampling Time [UTC] | Scan Type | Azimuth Rel.[§†] [°] | Elevation Rel.[‡] [°] | $\frac{d\measuredangle}{dt}$ [°/s] | $\Delta t$ [s] | $\Delta r$ [m] |
|---|---|---|---|---|---|---|
| 19.09 08:55 – 09:55 | PPI-Vol. | -10–80 | 5–20 | 1 | 0.033 | 3 |
| 19.09 10:50 – 12:30 | PPI-Scan | -50–85 | 5 | 1 | 0.033 | 3 |
| 19.09 12:40 – 13:40 | PPI-Vol. | -30–60 | 5–20 | 0.5 | 0.033 | 3 |
| 19.09 13:45 – 14:30 | RHI-Scan | 0 | 5–175 | — | 0.033 | 3 |
| 19.09 16:30 – 17:40 | PPI-Vol. | -10–80 | 5–25 | 1 | 0.033 | 3 |
| 19.09 17:40 – 17:50 | RHI-Scan | 170 | 2–20 | 0.5 | 0.033 | 3 |
| 20.09 08:15 – 08:30 | PPI-Scan | -30–85 | 10 | 0.5 | 0.033 | 3 |
| 20.09 08:45 – 09:45 | PPI-Scan | -10–85 | 5 | 1 | 0.033 | 3 |
| 20.09 09:50 – 11:00 | PPI-Scan | -10–85 | 15 | 1 | 0.033 | 3 |
| 20.09 11:05 – 12:05 | PPI-Scan | -10–85 | 5 | 1 | 0.033 | 3 |
| 20.09 12:35 – 13:30 | PPI-Scan | -10–85 | 20 | 1 | 0.033 | 3 |
| 20.09 13:33 – 14:39 | RHI-Scan | 40 | 5–175 | 0.5 | 0.033 | 3 |
| 20.09 16:15 – 16:30 | PPI-Scan | 30–60 | 2.5 | 2 | 0.033 | 3 |
| 20.09 16:31 – 16:45 | PPI-Scan | 40–50 | 2.5 | 1 | 0.033 | 3 |
| 20.09 16:55 – 17:05 | PPI-Scan | 30–350 | 5 | 1 | 0.33 | 3 |
| 20.09 18:00 – 18:20[c] | PPI-Scan | 30–350 | 5 | 1 | 0.33 | 3 |
| 21.09 10:00 – 10:15[b] | PPI-Scan | 30–350 | 5 | 1 | 0.33 | 3 |
| 21.09 10:20 – 11:20 | PPI-Vol. | -30–80 | 5–20 | 0.5 | 0.33 | 3 |
| 21.09 12:15 – 13:15 | PPI-Vol. | -30–80 | 5–20 | 0.5 | 0.33 | 3 |

§ Azimuth angle relative to the *zero scan direction* (148.54°): Azimuth=Relative Azimuth+148.54°.

† Farm relative azimuth angle= $193.5° - 148.54° = 44.96°$.

‡ Elevation angle relative to the *horizon elevation* (0.24°): Elevation=Relative Elevation−0.24°.

[a] Hard target measurement for calibration of azimuth and elevation angles (Pal, 2009).

[b] Background smoke measurement.

[c] Smoke plume measurement.

Table 8: Data acquired by the UHOH scanning aerosol lidar system, Mettingen 12.–21.09.05, Pal (2009).

## 4.5 BACKSCATTERING COEFFICIENTS FROM LIDAR MEASUREMENTS

*Lidar Signal*

The lidar (Light Detection And Ranging) system is based on the principle that a fraction of the power emitted by the laser (short pulse of light) will be scattered backwards due to the presence of gas molecules and aerosol particles. The backscattered power is given in the so-called lidar-equation, which for simple elastic scattering reads:

$$P_\lambda(R) = C\,O(R)\,\frac{\beta_\lambda(R)}{R^2}\,e^{-2\int_0^R \alpha_\lambda(r)\,dr} \tag{4.1}$$

where $\lambda$ stands for the laser wavelength, $R$ the distance from the scanner of the lidar system, $P_\lambda(R)$ the instantaneous power received $\Delta t = 2Rc$ after the laser pulse emission, $c$ the speed of light, $C$ is a devise dependent constant, $O(R)$ the overlap function, $\alpha_\lambda$ and $\beta_\lambda$ are the atmospheric extinction and backscattering coefficient (particles and molecules).

In the near range, the volume of space containing the transmitted laser pulse may not be completely on the field of view of the receiver of the lidar. This effect is called *incomplete overlap* and the overlap function ($O(R)$) accounts for it. For the UHOH scanning aerosol lidar system, full overlap ($O(R) \approx 1$) is reached from 200–300 m depending on the system configuration, determining the minimum range on the data sets, while the maximum range is about 12 km.

The atmospheric extinction and backscattering coefficients can be divided into their molecular and particulate contributions:

$$\alpha_\lambda = \alpha_\lambda^{mol} + \alpha_\lambda^{par}$$
$$\beta_\lambda = \beta_\lambda^{mol} + \beta_\lambda^{par}$$

were $\alpha_\lambda^{mol}$, $\beta_\lambda^{mol}$, $\alpha_\lambda^{par}$ and $\beta_\lambda^{par}$ represent the molecular and particulate (or aerosol) contribution to the extinction and backscattering coefficients.

The molecular extinction and backscattering coefficients ($\alpha_\lambda^{mol}$ and $\beta_\lambda^{mol}$) can be calculated from the molecular concentration estimated from temperature and pressure profiles (Bucholtz, 1995). The aerosol extinction and backscattering coefficients ($\alpha_\lambda^{par}$ and $\beta_\lambda^{par}$), previously described in equations (3.1) and (3.2), can be retrieved from the lidar measurements (Fernald, 1984; Fernald *et al.*, 1972; Klett, 1981, 1985) for later comparison with model results.

*Inversion of the Lidar Equation*

For each distance ($R_i$) the lidar-equation has two unknowns ($\alpha_\lambda^{par}(R_i)$ and $\beta_\lambda^{par}(R_i)$), leading to an under determined system of equations. Assuming that the aerosol extinction to backscattering ratio (or lidar ratio) is known and constant:

$$S_\lambda^{par} = \frac{\alpha_\lambda^{par}(R_i)}{\beta_\lambda^{par}(R_i)} \quad 0.2\ km \leqslant R_1 < R_2 < \ldots < R_n \leqslant 12\ km$$

and following Fernald (1984), the aerosol backscattering coefficient ($\beta_\lambda^{par}$) can be obtained from the lidar-equation:

$$\begin{aligned}\beta_\lambda(R_i) &= \beta_\lambda^{mol}(R_i) + \beta_\lambda^{par}(R_i) \\ &= \frac{P_\lambda(R_i)\, R^2\, e^{-2\psi(0,R_i)}}{C - 2S_\lambda^{par} \int_0^{R_i} P_\lambda(r)\, r^2\, e^{-2\psi(0,r)} dr}\end{aligned} \tag{4.2}$$

with

$$\psi(a,b) = \int_a^b S_\lambda^{par} \beta_\lambda^{mol}(l) - \alpha_\lambda^{mol}(l) dl$$

The devise dependent constant (C) is proportional to the emitted power and the detection efficiency of the system:

$$C = P_{0,\lambda} \frac{c\, t_p}{2} A\, K$$

where $P_{0,\lambda}$ is the power emitted from the laser, $t_p$ the time length of the laser pulse, $A$ the receiving surface of the telescope, and $K$ the detection efficiency of the system.

The detection efficiency ($K$) is quite difficult to measure and it may change during the operation of the system. This can be overcome using of the solution of (4.2) on the far range as a priory information, transforming it into a backward recursion:

$$\begin{aligned}\beta_\lambda(R_i) &= \beta_\lambda^{mol}(R_i) + \beta_\lambda^{par}(R_i) \\ &= \frac{P_\lambda(R_i)\, R^2\, e^{-2\psi(R_{i+1},R_i)}}{\frac{P_\lambda(R_{i+1})\, R_{i+1}^2}{\beta_\lambda(R_{i+1})} - 2S_\lambda^{par} \int_{R_{i+1}}^{R_i} P_\lambda(r)\, r^2\, e^{-2\psi(R_{i+1},r)} dr}\end{aligned}$$

To start the solution of the backward recurrence it is needed to estimate the value of $\beta_\lambda(R_n)$. At a relatively large distance from the lidar, the laser beam is likely to be above the boundary layer where it is assumed that the aerosol contribution to the backscattering coefficient is negligible ($\beta_\lambda^{par}(R_n) \approx 0$) and therefore:

$$\beta_\lambda(R_n) = \beta_\lambda^{mol}(R_n)$$

*Comments and Assumptions*

According to Fernald (1984), the backward formulation is preferable over the analogous forward formulation, as it posses better numerical stability and due to its rapidly vanishing dependence from far range initial guess ($\beta_\lambda(R_n) = \beta_\lambda^{mol}(R_n)$). The lidar derived backscattering coefficient seem to have a very weak sensitivity to the lidar ratio (Feingold and Morley, 2003). For the PLUS1 lidar data sets the lidar ratio was set to be $S_\lambda^{par} = 40\ sr$, in accordance to within 10 % of the model simulations. The molecular extinction and backscattering coefficients ($\alpha_\lambda^{mol}(R_i)$ and $\beta_\lambda^{mol}(R_i)$) were calculated according to Bucholtz (1995) from temperature and pressure vertical profiles derived from the radio soundings when available (15.–17.09.05) or ECMWF data[9] when no measurements were available (18.–21.09.05).

The algorithm shown here retrieves the aerosol backscattering coefficient from single-wavelength lidar data sets. Pal (2009) developed a new technique for inversion of lidar signals collected by various scanning measurements. Using this approach, the determination of aerosol backscattering coefficient in 2-D or 3-D is possible. For multi-wavelength data sets it is possible to extend the retrieval procedure, and obtain size and even composition parameters (Böckmann, 2001; Böckmann and Wauer, 2001; Kocifaj and Horvath, 2005), under additional assumptions about the particle structure and size distribution similar to the ones employed in the construction of the LES-AOP model (Section 3.3.2 and Section 3.3.3).

## 4.6 SELECTION OF DATA SETS FOR SIMULATION

Two days were selected for model simulation after the analysis of the aerosol backscattering coefficient data sets retrieved from the lidar signals:

17.09.05: Was selected among the three days of intensive measurements (15.–17.09.05). During the whole extension of the measurement campaign RHI-Scans showed in general only weak, if any, evidence of the farm plume, thus discarding 15.09.05 when only RHI-Scans were taken (Table 8). On 16.09.05, the PPI-Scans were later found to have aimed too high (10° of elevation), thereby missing the farm plume.

20.09.05: Was selected because it contains the only set of PPI-Scans with elevation below 5° which showed the most clear indication of the farm plume among all of the lidar measurements.

9 Weather analisis obtain from the European Centre for Medium-Range Weather Forecasts (ECMWF) Data Server.

# 5

# APPLICATION OF THE EXTENDED LES TO A FAINT AGRICULTURAL SOURCE

The LES-AOP model (Chapter 3) was developed to simulate the observable aerosol optical properties with high spatial and temporal resolution. This chapter deals with the first model simulations of this kind for a faint agricultural source. The aerosol backscattering coefficients for 17.09.05 and 20.09.05 (discussion in Section 4.6) were simulated for a small model domain around the farm location (Figure 6). The aerosol module was set up from ground measurements for the PLUS1 campaign (Section 4.4.1). Some of the results are compared with aerosol backscattering coefficients derived from selected lidar measurements (Section 4.5). The LES-AOP model set-up, initialisation and forcing are described in Section 5.1 and results are discussed in Section 5.2.

## 5.1 SET-UP, INITIALISATION AND FORCING

The model domain size and resolution, as well as the aerosol particle size range and resolution are the result of a trade-off between model performance and an accurate representation of the aerosol size distribution, composition and its derived optical properties. The selected days were simulated between $09:00-18:00$[UTC], for a model domain of $4\ \mathrm{km} \times 4\ \mathrm{km}$ in horizontal and $2\ \mathrm{km}$ in vertical direction, with a horizontal and vertical resolution of $50\ \mathrm{m}$ and $20\ \mathrm{m}$ respectively. The temporal resolution was adjusted during the simulation time (between $1-5$ s) to fulfill the Courant-Friedrichs-Levy (CFL) condition. The aerosol size distribution was represented by the bin scheme (Section 3.3.3) configured for 14 size bins (Table 9).

The problem of obtaining the right balance between an accurate representation of the aerosol population and the associated computational cost is not unique to this work. In the framework of air quality modelling, Zhang *et al.* (1999) suggests that 8 size bins in the $0.01-5\ \mu\mathrm{m}$ particle radius range would generally be sufficient to simulate detailed aerosol dynamics and thermodynamics. Wu *et al.*

(1996) suggest that 9 size bins in the $0.005 - 5$ $\mu m$ particle radius range would genetrate accurate results for aerosol optical properties. von Salzen and Schlünzen (1999b) suggest that 4 size bins in the $0.05 - 50$ $\mu m$ particle radius range would provide sufficient accuracy for mass distribution, at least 8 size bins for accurate surface area distribution and more than 16 size bins for total particle number. The 14-bin scheme used here, is comparable to the 16 size bins of von Salzen and Schlünzen (1999b). In addition, it offers a slightly better resolution of the particle size range than the first two recommendations, while maintaining a relatively small number of size bins and therefore keeping an acceptable computational cost.

| Size Range | Resolution | Size Bin Edges |
|---|---|---|
| $r_p$ [$\mu m$] | bins [#] | $r_p$ [$\mu m$] |
| 0.005–0.01 | 1 | $0.005 \cdots 0.010$ |
| 0.01–0.1 | 4 | $0.010 \cdots 0.017 \cdots 0.031 \cdots 0.056 \cdots 0.100$ |
| 0.1–1 | 4 | $0.100 \cdots 0.177 \cdots 0.316 \cdots 0.566 \cdots 1.000$ |
| 1–10 | 4 | $1.000 \cdots 1.778 \cdots 3.162 \cdots 5.663 \cdots 10.00$ |
| 10–15 | 1 | $10.00 \cdots 15.00$ |

Table 9: Bin scheme resolution: Number of size bins per particle radius range and their edges. Wet radius $r_p$ at 20 C° of temperature and 80 % of relative humidity.

The forcing and the output time steps were set to 15 $min$, when instantaneous fields for the wind components, temperature, relative humidity and the particle number concentrations for each aerosol size bin were written. Additionally, 15 $min$ averaged fields were written for temperature, relative humidity and the particle number concentration for each aerosol size bin. The instantaneous and time averaged fields were used to produce instantaneous and time averaged fields for aerosol extinction and backscattering coefficients as described in Section 3.1.

The farm emission (Section 3.7.1) was set up in the middle of the model domain. Boundary conditions for the aerosol fields were set up following the *boundary recycling from background aerosol field* scheme described in Section 3.7.2. In which every size bin for each aerosol specie is represented by two fields: the background field (BGD) and the polluted field (POL). The background field has no farm emission and normal lateral cyclic boundary conditions. The polluted field has farm emission and the same inflow boundary conditions as the background field but open outflow conditions. This set-up allows to isolate the farm emission

plume as the difference between the polluted and background fields, which will be referred in the following as the farm contribution.

### 5.1.1 *Aerosol Simulation Scenarios*

The aerosol scenarios for 17.09.05 and 20.09.05 are based upon the ground measurements of 17.09.05, assuming the same aerosol composition and size distribution for 17.09.05 and 20.09.05. This was due to the lack of measurements of the aerosol particle size distribution and composition after the intensive measurement period of the PLUS1 measurement campaign (15.–17.09.05).

#### *Aerosol Mass Size Distribution*

Two aerosol load scenarios were considered to represent the range of possible aerosol particle number (wet) size distributions (NSDs) derived from different dry mass concentrations from the PLUS1 in-situ measurements. Both scenarios are based on the measurements for the 17.09.05. The background aerosol load is derived from the nine stages of the Berner cascade impactor, and the farm contribution from the relative mass increase in the $PM_{2.5}$ and the $PM_{10}$ measurements (measured 700 m downwind from the farm). The aerosol load scenarios are summarised in Table 10.

The high aerosol load (HAER) is based on the total mass on the individual stages of the cascade impactor (determined by gravimetry) which determines the background aerosol NSD. The farm contribution to the aerosol NSD comes from the measured $PM_{2.5}$ and $PM_{10}$ increase relative to the upwind measurement (background aerosol), which suggests an increase of 140 % for particles of aerodynamic diameter below 2.5 µm and 10 % for particles between $2.5 - 10$ µm.

The mass determination by gravimetry is more uncertain than by ion chromatography. Furthermore, the particularly low ratio of ions and total mass suggests that the total mass concentration might have been lower than gravimetrically determined (HAER scenario). Therefore, the background aerosol NSD for the low load aerosol scenario (LAER) was derived by scaling down of the HAER background NSD to the total mass shown on the total inorganic ions, and the farm contribution from assuming a 100 % increase on the downwind measurement for $PM_{2.5}$ and $PM_{10}$.

#### *Aerosol Composition*

Following the Hess *et al.* (1998) description for *continental average* aerosol, the background aerosol is described as an externally mixed aerosol composed of

| Scenario | Dry Mass Concentration [$\mu g/m^3$] | | | |
|---|---|---|---|---|
| | Background[§] | | Farm Contribution[†] | |
| | 0.03–2 $\mu m$ | 2–16 $\mu m$ | 0.03–2 $\mu m$ | 2–16 $\mu m$ |
| HAER | 12.36 | 12.05 | 17.30 | 1.21 |
| LAER | 2.78 | 2.72 | 2.78 | 2.72 |

[§] From 17.09.05 upwind PLUS1 measurements.

[†] From 17.09.05 downwind PLUS1 measurements.

Table 10: Aerosol load scenarios: high (HAER) and low (LAER) load. Dry mass concentration for $0.03 - 2$ $\mu m$ and $2 - 16$ $\mu m$ aerodynamic diameter range.

water soluble (WASO), water insoluble (INSO) and soot (SOOT) particles. The number concentration of WASO particles depends on the assumptions of the hygroscopic properties. In order to take this into account, two hygroscopicity scenarios were created from different hygroscopicity parameterisations (Section 3.2 and Appendix B). The low hygroscopicity scenarios (LWAT) assume the empirical growth curve for a continental aerosol (Deuselhach aerosol in Winkler, 1988), the high hygroscopicity scenarios (HWAT) assumes the hygroscopicity of a pure salt aerosol ($NH_4NO_3$ in Robinson and Stokes, 1959). The hygroscopicity scenarios combined with the aerosol load scenarios leads to a total of four simulation scenarios (Table 11) for each of the simulated days (17.09.05 and 20.09.05).

For all scenarios, the INSO and SOOT particle concentrations were set consistently to a continental aerosol. The WASO particle concentration was set to complete the total mass according to the aerosol load scenario. The INSO and SOOT particle concentrations follow the log-normal distribution description for *continental average* aerosol from Hess *et al.* (1998) (9.5 $\mu g/m^3$ and 0.5 $\mu g/m^3$ dry mass concentration, respectively). The INSO particle concentration was reduced to a level consistent with the 3.0 $\mu g/m^3$ dry mass concentration estimated from the measurements.

### 5.1.2 LES *Initialisation and Forcing*

Output data from the *Lokal Modell* (LM; Doms and Schättler, 2002; Doms *et al.*, 2005; Schraff and Hess, 2005) from the *Deutscher Wetterdienst* (DWD, German Weather Service) was used to derive the initialisation and forcing of the LES part of the LES-AOP model (without precipitation, Section 2.7). LM output has 1 h temporal resolution and approximately 7 km horizontal resolution, with different vertical resolution depending on the variable (Table 12). The LM output variables

| Component | Dry Mass Concentration [$\mu g/m^3$] | | | |
|---|---|---|---|---|
| | Background[§] | | Farm Contribution[†] | |
| | $< 2\ \mu m$ | $\geqslant 2\ \mu m$ | $< 2\ \mu m$ | $\geqslant 2\ \mu m$ |
| HAER-LWAT scenario | | | | |
| WASO | 12.05 | 11.38 | 17.33 | 1.20 |
| INSO | 0.01 | 2.72 | — | — |
| SOOT | 0.56 | 0.00 | — | — |
| HAER-HWAT scenario | | | | |
| WASO | 12.20 | 11.69 | 17.33 | 1.20 |
| INSO | 0.01 | 2.72 | — | — |
| SOOT | 0.56 | 0.00 | — | — |
| LAER-LWAT scenario | | | | |
| WASO | 2.50 | 2.22 | 2.74 | 2.52 |
| INSO | 0.01 | 2.72 | — | — |
| SOOT | 0.56 | 0.00 | — | — |
| LAER-HWAT scenario | | | | |
| WASO | 2.63 | 2.36 | 2.78 | 2.50 |
| INSO | 0.01 | 2.72 | — | — |
| SOOT | 0.56 | 0.00 | — | — |

[§] From 17.09.05 upwind PLUS1 measurements.

[†] From 17.09.05 downwind PLUS1 measurements.

Table 11: Aerosol composition scenarios: Dry mass concentrations for water soluble (WASO), water insoluble (INSO) and soot (SOOT) particles of aerodynamic diameter $< 2\ \mu m$ and $\geqslant 2\ \mu m$ for the 14 size bins configuration (Table 9).

were interpolated from the pole rotated coordinate system of the LM to the farm coordinates using the *Climate Data Operators* (CDO; Schulzweida *et al.*, 2007).

For initialisation of the LES runs, the vertical profiles of several variables (u, v and w wind components, temperature, humidity and turbulent kinetic energy, Section 2.7) are needed on the LES vertical levels ($10, 30, \ldots, 1990$ m). They were linearly interpolated from the available LM levels for the variable (Table 12) using INTERPOL routine of IDL (Interactive Data Language from RSI). The LES model was

forced only by the LM latent and sensible heat fluxes, interpolated to the farm location and considered constant over the model domain. These heat fluxes were linearly interpolated in time to the 15 $min$ output resolution of the LES model.

| Variable | LM levels | | |
|---|---|---|---|
| | Surface | Above ground | Model Levels |
| | 0 m | 500, 1000, 1500, 2000 m | 24–36 |
| Used for LES initialisation | | | |
| temperature | √ | √ | — |
| u component (zonal) of wind | — | √ | — |
| v component (meridional) of wind | — | √ | — |
| w component (vertical) of wind | — | √ | √ |
| specific humidity | √ | — | — |
| relative humidity | — | √ | — |
| turbulent kinetic energy | — | — | √ |
| Used for LES forcing | | | |
| latent heat flux | √ | — | — |
| sensible heat flux | √ | — | — |

Table 12: LM variables used for initialisation and forcing of the LES model.

## 5.2 MODEL SIMULATIONS

### 5.2.1 *Post Processing*

For the farm polluted fields (POL) some extra post processing was needed before the calculation of the aerosol extinction and backscattering coefficients (Section 3.1).

The farm contribution to the aerosol NSD, for all scenarios, was based on the $PM_{2.5}$ and $PM_{10}$ increase observed 700 m downwind from the farm. As the PM increase did not take place directly at the farm location, the farm emission strength was systematically underestimated. Under the assumption of the bin scheme (Section 3.3.3), for each one of the 42 bins (14 size bins for WASO, INSO and SOOT particles) all particles are assumed to have the same (dry) mass, equal to the bin characteristic dry mass. Therefore, the total particle number and the total particle mass can be determined from equations (3.21) and (3.22) (Section 3.8).

Consequently, to correct the emission strength of the farm, the aerosol farm contribution to the particle number concentration for each one of the different 42 bins was amplified by the quotient of the 9 h-mean number concentration of the lowermost model level over the farm location and the corresponding 9 h-mean of the maximum 700 m away from the farm. Thereby the aerosol farm contribution was re-scaled to be consistent with the 700 m downwind measurement.

The farm emission scheme (Section 3.7.1), assumes that turbulent diffusion is the predominant transport mechanism between the near ground and the lowermost model level. It consequently exhibits a turbulence driven daily cycle on the farm emission flux. The stables are actively ventilated, and livestock activity inside the stable is not driven by turbulence outside the stable. The farm emission flux was calculated as the difference between the flux trough two parallel vertical cross sections upwind and downwind from the farm location. Consequently, the POL fields were corrected so that they exhibit a constant farm emission flux equal to the mean farm total mass emission flux for the 17.09.05 for the corresponding scenario (approximately 100 g/h and 500 g/h for the LAER and HAER scenarios, respectively).

All LES-AOP simulations show inertial oscillation in the wind field. Attempts to force LES with LM derived geostrophic winds in order to obtain wind directions similar to the LM model were unsuccessful. Therefore, the LES-AOP aerosol fields needed to be adjusted to the observed wind direction according to the $50 - 250$ m height of the radio-soundings for the 17.09.05 simulations, or according to the wind direction predicted by the LM for the 20.09.05.

### 5.2.2 *Model Simulation Results*

The aerosol backscattering coefficient of the LES-AOP model levels ($10, 30, \ldots, 1990$ m) were interpolated to the PPI-Scan projection for 2.26° and 4.76° elevation (Section 4.4.2). These results are displayed in Table 13, Figure 15 and Figure 16. The farm contribution to the aerosol backscattering coefficient on the original model levels is shown in Figure 17 and Figure 18.

The aerosol backscattering coefficient ($\beta$) for 20.09.05 is consistently higher than for 17.09.05 (Table 13). For both days and all model simulations the mean aerosol backscattering coefficient ($\overline{\beta}$) decreases with simulation time, while the farm contribution ($\Delta\beta$) increases. The decrease of $\overline{\beta}$ is caused by the aerosol surface flux (ASF, Section 3.7.1), which constantly decrease the background concentration at the lowermost level. This indicates that the assumption for the initial vertical profile of the aerosol NSD (Section 3.8) overestimated the particle number concentration at the lowermost model level. The sustained increase of $\Delta\beta$ may be explained as

the combined effect of the ASF decreasing the background aerosol concentration and the post processing corrections to the farm contribution (Section 5.2.1), but further testing is required to confirm this explanation.

For the 17.09.05 simulations, it is possible to discriminate the farm plume from the background in most of the 2.26° elevation snapshot and averaged fields (Figure 15), and in some of the 4.76° elevation time averaged fields (Figure 16). The lack of farm emission signal in the 4.76° snapshot fields suggests that the core of the farm plume was lower than that elevation. This is in agreement with the lack of evidence of farm emission in the lidar data for this day.

The farm contribution to the aerosol backscattering coefficient for the 17.09.05 (Figure 17 and Figure 18) does not show levels that would allow to discriminate the farm plume from the background (POL-BGD $\geqslant \cdot 10^{-6}$ $sr^{-1}$ $m^{-1}$) at a height of 150 $m$ or above. The shape of the farm plume in the snapshot fields is clearly influenced by the turbulent structure of the wind field, while it shows a more Gaussian shape on the time averaged fields.

In Figure 19 it is possible to observe the development of a numerical instability that causes unphysical values in the upper model domain towards the end of the simulation of 17.09.05. In the 15 $min$ averaged fields (Figure 19a–c) it is not possible to observe the development, only the artifact at 16 : 00[UTC]. It is in the instantaneous fields (Figure 19d–f) that the evolution becomes evident. The proximity of the boundary layer top to the model upper boundary, may be the reason for unphysical oscillations (Figure 19e), that produce the artifacts observed (Figure 19c,e). Fortunately, the artifact remains localised at the top of the model domain, without reaching the region of interest for this study, i.e. the near ground region.

### 5.2.3 *Comparison Between Model Results and Lidar Measurements*

From the statistical values for the aerosol backscattering coefficient ($\beta$) derived from the lidar measurements for 17.09.05 and 20.09.05 (Lammel *et al.*, 2007) summarised in Table 14, the almost total absence of measurements at low elevations becomes evident. The only clear evidence of the farm plume was found in the PPI-Scan at 2.26° elevation on the 20.09.05 around 16 : 00[UTC] (Figure 20).

Table 13 and Table 14 are not directly comparable as the scanning pattern and time length of the lidar data sets changes during each day (Table 8), while the LES-AOP model consistently outputs every 15 $min$ on a predefined Cartesian grid. In addition, the lidar measurements and the model domain have a relatively small intersection. Furthermore, the LES-AOP model simulates both background and farm polluted fields, while the lidar measurements can refer as background only

| Time | HAER-LWAT | | | | HAER-HWAT | | | | LAER-LWAT | | | | LAER-HWAT | | | |
|---|---|---|---|---|---|---|---|---|---|---|---|---|---|---|---|---|
| [UTC] | 17.09.05 | | 20.09.05 | | 17.09.05 | | 20.09.05 | | 17.09.05 | | 20.09.05 | | 17.09.05 | | 20.09.05 | |
| | $\Delta\beta$ | $\overline{\beta} \pm \sigma_\beta$ | $\Delta\beta$ | $\overline{\beta} \pm \sigma_\beta$ | $\Delta\beta$ | $\overline{\beta} \pm \sigma_\beta$ | $\Delta\beta$ | $\overline{\beta} \pm \sigma_\beta$ | $\Delta\beta$ | $\overline{\beta} \pm \sigma_\beta$ | $\Delta\beta$ | $\overline{\beta} \pm \sigma_\beta$ | $\Delta\beta$ | $\overline{\beta} \pm \sigma_\beta$ | $\Delta\beta$ | $\overline{\beta} \pm \sigma_\beta$ |
| PPI-Scan at 2.26° ($\beta$ [$10^{-6}$/(sr m)]) | | | | | | | | | | | | | | | | |
| 10:00 | 0.30 | 4.08±0.24 | 3.68 | 5.95±0.16 | 0.42 | 5.81±0.34 | 5.26 | 8.60±0.24 | 0.05 | 0.74±0.05 | 0.60 | 1.10±0.05 | 0.08 | 1.19±0.07 | 0.90 | 1.77±0.06 |
| 11:00 | 0.81 | 3.37±0.22 | 1.38 | 5.65±0.12 | 1.16 | 4.80±0.31 | 2.00 | 8.13±0.23 | 0.14 | 0.61±0.04 | 0.27 | 1.02±0.05 | 0.21 | 0.98±0.06 | 0.36 | 1.66±0.06 |
| 12:00 | 0.64 | 3.38±0.21 | 8.51 | 4.73±0.43 | 0.90 | 4.91±0.31 | 12.30 | 6.75±0.64 | 0.11 | 0.64±0.04 | 1.43 | 0.85±0.09 | 0.16 | 1.02±0.07 | 2.15 | 1.38±0.13 |
| 13:00 | 0.68 | 3.15±0.17 | 10.10 | 4.36±0.31 | 1.00 | 4.63±0.27 | 14.60 | 6.25±0.46 | 0.12 | 0.60±0.03 | 1.67 | 0.80±0.06 | 0.18 | 0.97±0.06 | 2.52 | 1.29±0.09 |
| 14:00 | 1.05 | 2.94±0.15 | 7.26 | 4.19±0.34 | 1.56 | 4.36±0.23 | 10.60 | 6.14±0.50 | 0.18 | 0.56±0.03 | 1.17 | 0.79±0.06 | 0.28 | 0.91±0.05 | 1.80 | 1.28±0.09 |
| 15:00 | 1.16 | 2.73±0.10 | 10.90 | 3.90±0.38 | 1.74 | 4.09±0.17 | 16.50 | 5.81±0.57 | 0.20 | 0.53±0.02 | 1.79 | 0.75±0.06 | 0.31 | 0.86±0.04 | 2.88 | 1.21±0.10 |
| 16:00 | 2.66 | 2.55±0.12 | 11.10 | 3.61±0.40 | 4.04 | 3.86±0.19 | 16.60 | 5.43±0.59 | 0.45 | 0.49±0.02 | 1.68 | 0.70±0.06 | 0.71 | 0.81±0.04 | 2.67 | 1.14±0.10 |
| 17:00 | 3.23 | 2.39±0.15 | 10.30 | 3.42±0.44 | 4.59 | 3.64±0.22 | 15.80 | 5.18±0.68 | 0.55 | 0.46±0.03 | 1.61 | 0.66±0.07 | 0.84 | 0.77±0.04 | 2.59 | 1.08±0.11 |
| 18:00 | 3.29 | 2.25±0.10 | 46.30 | 3.39±1.88 | 4.23 | 3.43±0.14 | 68.80 | 5.14±2.75 | 0.57 | 0.44±0.02 | 7.19 | 0.65±0.29 | 0.82 | 0.72±0.03 | 11.50 | 1.07±0.46 |
| PPI-Scan at 4.76° ($\beta$ [$10^{-6}$/(sr m)]) | | | | | | | | | | | | | | | | |
| 10:00 | 0.02 | 4.28±0.25 | 0.93 | 5.70±0.29 | 0.03 | 6.11±0.36 | 1.42 | 8.31±0.37 | 0.01 | 0.78±0.05 | 0.16 | 1.07±0.05 | 0.01 | 1.25±0.07 | 0.28 | 1.72±0.07 |
| 11:00 | 0.05 | 3.62±0.30 | 1.01 | 5.58±0.23 | 0.07 | 5.17±0.43 | 1.54 | 8.11±0.29 | 0.01 | 0.66±0.06 | 0.18 | 1.03±0.05 | 0.01 | 1.06±0.09 | 0.31 | 1.68±0.06 |
| 12:00 | 0.07 | 3.48±0.18 | 1.94 | 5.02±0.37 | 0.10 | 5.03±0.27 | 2.80 | 7.27±0.61 | 0.01 | 0.65±0.04 | 0.33 | 0.93±0.09 | 0.02 | 1.04±0.06 | 0.49 | 1.50±0.14 |
| 13:00 | 0.10 | 3.22±0.16 | 3.58 | 4.48±0.30 | 0.14 | 4.70±0.25 | 5.19 | 6.46±0.49 | 0.02 | 0.61±0.03 | 0.59 | 0.83±0.06 | 0.03 | 0.98±0.05 | 0.91 | 1.33±0.10 |
| 14:00 | 0.09 | 2.99±0.13 | 1.95 | 4.19±0.16 | 0.13 | 4.42±0.19 | 2.83 | 6.12±0.26 | 0.02 | 0.57±0.02 | 0.31 | 0.79±0.03 | 0.02 | 0.92±0.04 | 0.48 | 1.27±0.05 |
| 15:00 | 0.08 | 2.78±0.09 | 1.89 | 3.90±0.13 | 0.13 | 4.15±0.14 | 2.85 | 5.79±0.20 | 0.02 | 0.53±0.02 | 0.31 | 0.75±0.02 | 0.02 | 0.87±0.03 | 0.50 | 1.21±0.04 |
| 16:00 | 0.39 | 2.58±0.07 | 2.30 | 3.63±0.23 | 0.59 | 3.89±0.11 | 3.43 | 5.43±0.34 | 0.07 | 0.50±0.01 | 0.35 | 0.70±0.03 | 0.10 | 0.82±0.02 | 0.55 | 1.14±0.06 |
| 17:00 | 0.39 | 2.42±0.08 | 3.23 | 3.44±0.19 | 0.55 | 3.66±0.13 | 4.94 | 5.18±0.28 | 0.07 | 0.47±0.02 | 0.51 | 0.66±0.03 | 0.10 | 0.77±0.03 | 0.82 | 1.09±0.05 |
| 18:00 | 0.55 | 2.27±0.07 | 7.18 | 3.34±0.81 | 0.71 | 3.45±0.10 | 10.60 | 5.04±1.19 | 0.09 | 0.44±0.01 | 1.12 | 0.64±0.13 | 0.14 | 0.73±0.02 | 1.78 | 1.05±0.20 |

Table 13: Model predicted aerosol backscattering coefficient ($\beta$[$10^{-6}$/(sr m)]), PPI-Scans for 17.09.05 and 20.09.05. Maximum source contribution ($\Delta\beta = \max\{\text{POL} - \text{BGD}\}$) of the 15 min averaged field, and mean ($\overline{\beta} = \text{mean}\{\text{POL}\}$) and standard deviation ($\sigma_\beta = \text{st.dev.}\{\text{POL}\}$) of the farm polluted instantaneous field.

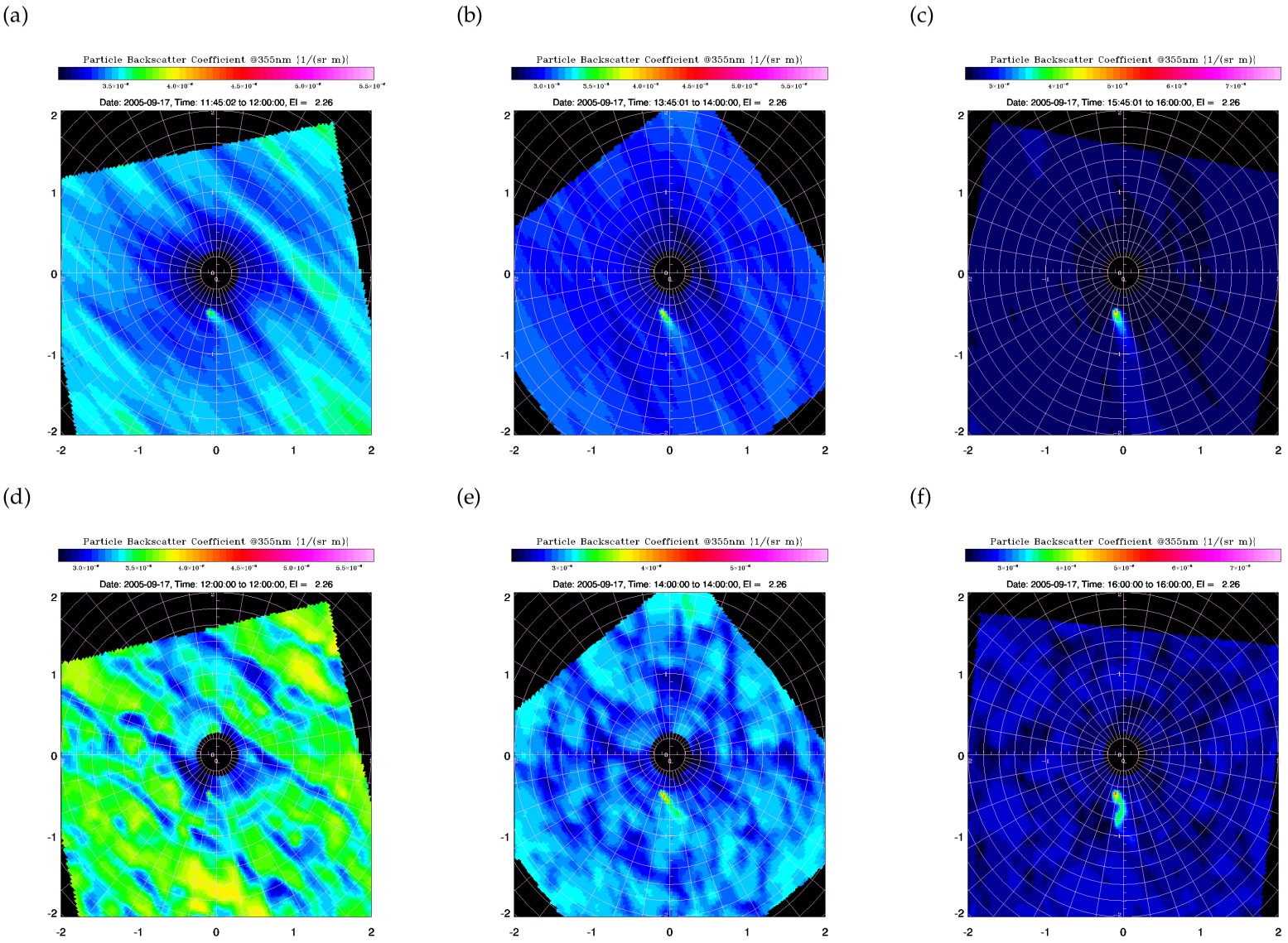


Figure 15: Simulated aerosol backscattering coefficients for 17.09.05, PPI-Scans for the farm polluted fields (POL) at 2.26° elevation 15 min averaged (a,b,c) and instantaneous snapshots (d,e,f) under the HAER-LWAT aerosol scenario at 12 : 00 (a,d), 14 : 00 (b,e) and 16 : 00 [UTC] (c,f).

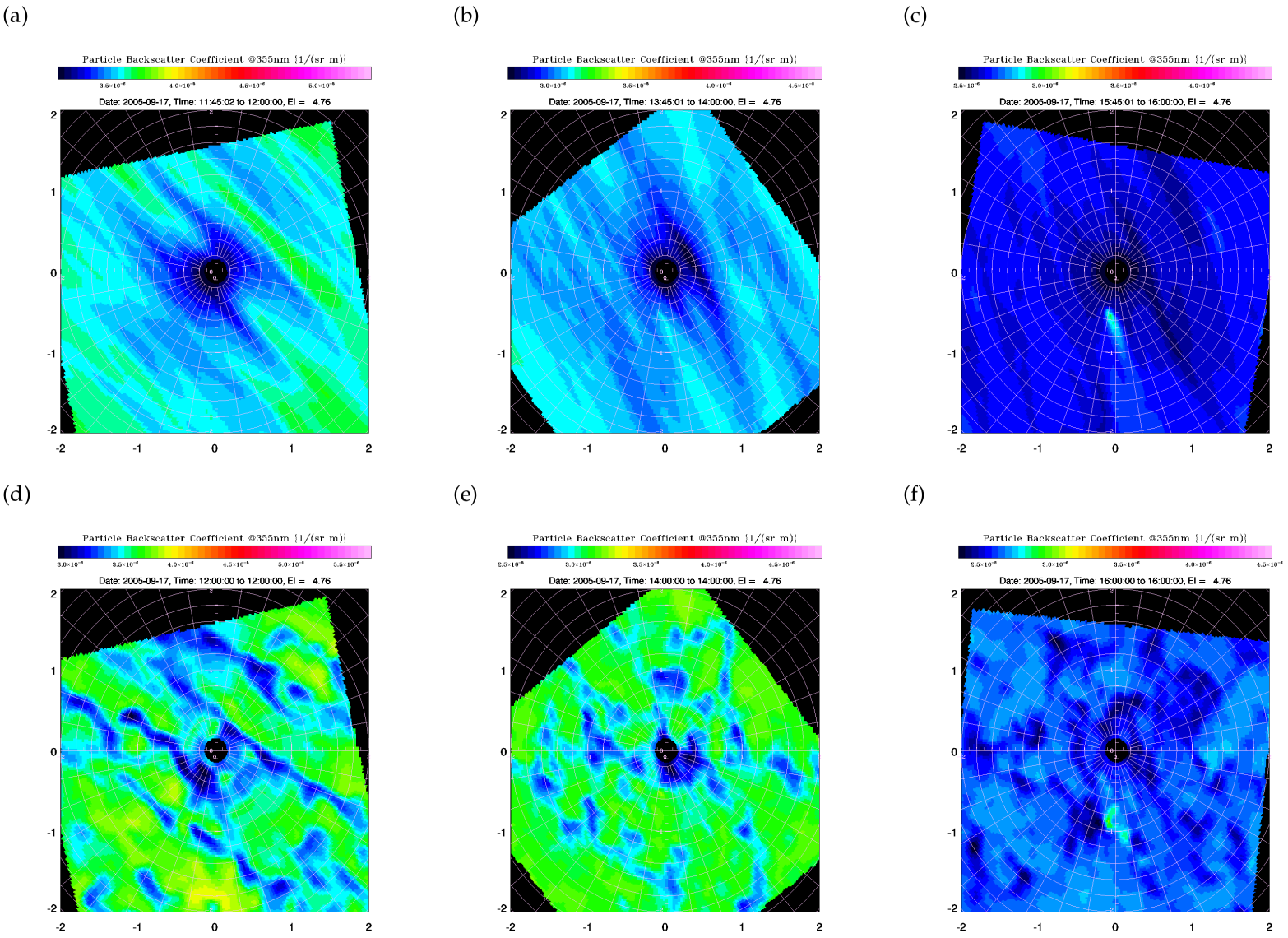


Figure 16: Simulated aerosol backscattering coefficients for 17.09.05, PPI-Scans for the farm polluted fields (POL) at 4.76° elevation 15 min averaged (a,b,c) and instantaneous snapshots (d,e,f) under the HAER-LWAT aerosol scenario at 12 : 00 (a,d), 14 : 00 (b,e) and 16 : 00 [UTC] (c,f).

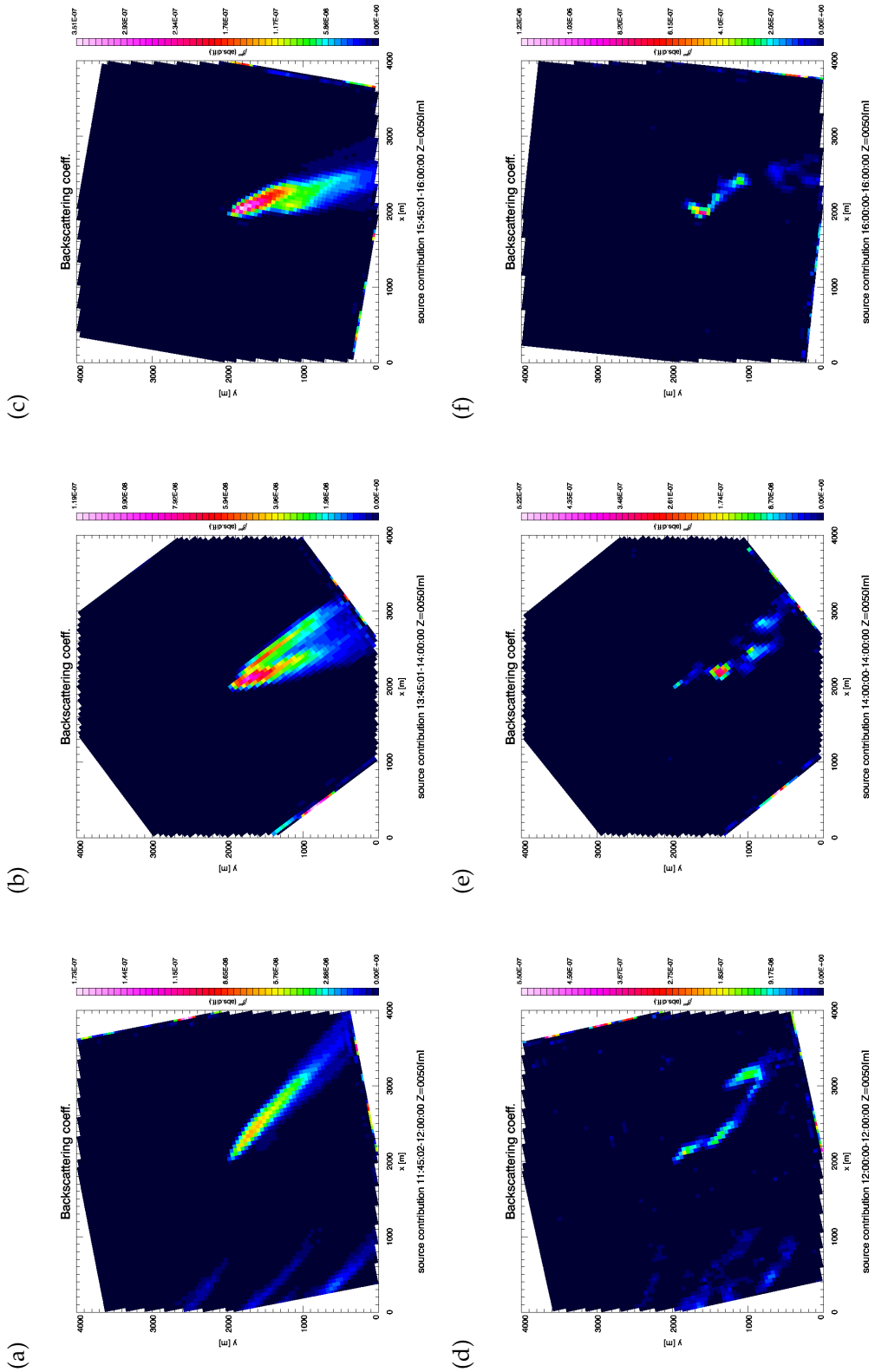


Figure 17: Simulated aerosol backscattering coefficients for 17.09.05, farm contribution fields (POL-BGD) at 50 m high 15 min averaged (a,b,c) and instantaneous snapshots (d,e,f) under the HAER-LWAT aerosol scenario at 12 : 00 (a,d), 14 : 00 (b,e) and 16 : 00 [UTC] (c,f).

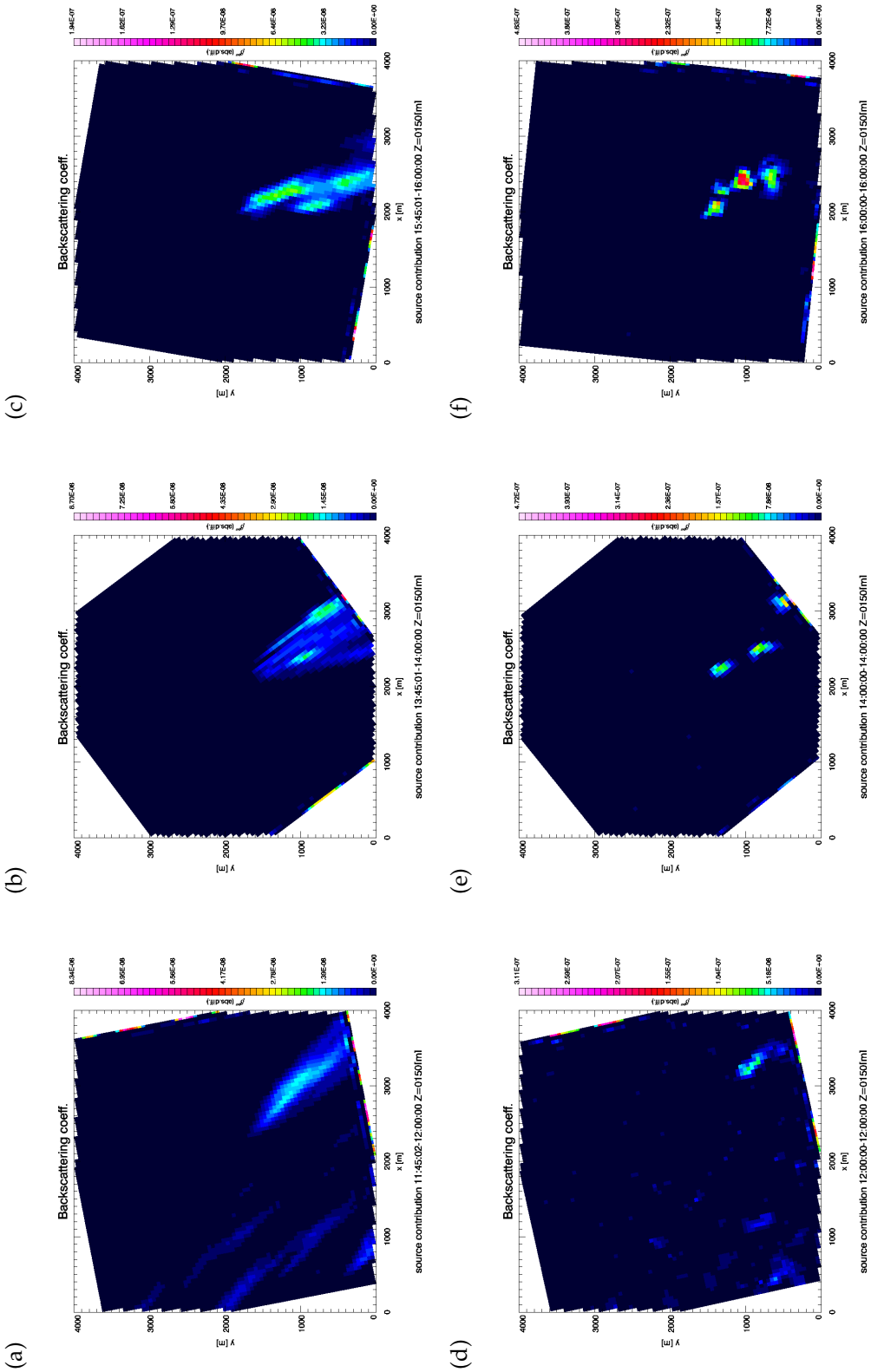


Figure 18: Simulated aerosol backscattering coefficients for 17.09.05, farm contribution fields (POL-BGD) at 150 m high 15 min averaged (a,b,c) and instantaneous snapshots (d,e,f) under the HAER-LWAT aerosol scenario at 12 : 00 (a,d), 14 : 00 (b,e) and 16 : 00 [UTC] (c,f).

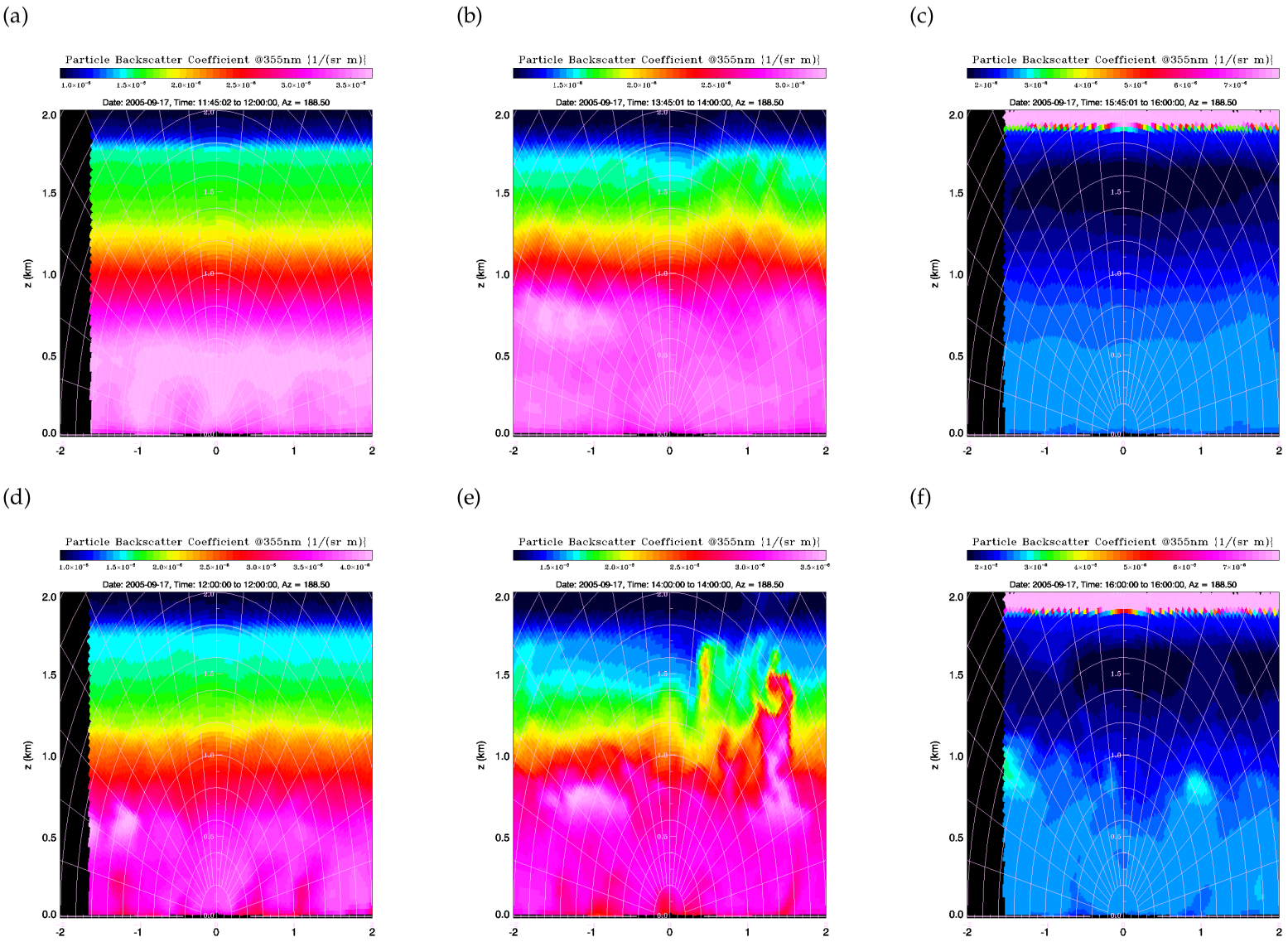


Figure 19: Simulated aerosol backscattering coefficients for 17.09.05, background field (BGD) at at 188.50° azimuth 15 min averaged (a,b,c) and instantaneous snapshots (d,e,f) under the HAER-LWAT aerosol scenario at 12 : 00 (a,d), 14 : 00 (b,e) and 16 : 00[UTC] (c,f).

to the portion of the scan pattern upwind to the farm location. Therefore, $\Delta\beta$ have different definitions, and $\overline{\beta}$ & $\sigma_\beta$ are based on different domains. Still, some comparison is possible, and shows that the observed range of values of $\beta$ lies between the simulated values under the various scenarios. No single simulation scenario seems to match all the observations.

| Time | UHOH scanning aerosol lidar system | | | |
|---|---|---|---|---|
| [UTC] | 17.09.05 | | 20.09.05 | |
| | $\Delta\beta$ | $\overline{\beta} \pm \sigma_\beta$ | $\Delta\beta$ | $\overline{\beta} \pm \sigma_\beta$ |
| PPI-Scan at 2.26° ($\beta$ $[10^{-6}/(\mathrm{sr\ m})]$) | | | | |
| 16:00 | — | — ± — | 3.0–9.0 | 2.9± 0.21 |
| 17:00 | — | — ± — | — | —± — |
| 18:00 | — | — ± — | <0.32 | 2.2± 0.16 |
| PPI-Scan at 4.76° ($\beta$ $[10^{-6}/(\mathrm{sr\ m})]$) | | | | |
| 10:00 | <0.22 | 2.0 ±0.11 | <0.25 | 2.5± 0.12 |
| 11:00 | — | — ± — | <0.42 | 3.5± 0.21 |
| 12:00 | <0.62 | 1.25±0.31 | <1.00 | 1.5± 0.51 |
| 13:00 | <0.54 | 1.2 ±0.27 | — | —± — |
| 14:00 | — | — ± — | <0.62 | 1.8± 0.31 |
| 15:00 | <0.26 | 1.8 ±0.13 | <0.22 | 1.8± 0.11 |
| 16:00 | — | — ± — | — | —± — |
| 17:00 | <0.20 | 1.0 ± 0.1 | <0.38 | 2.5± 0.19 |
| 18:00 | — | — ± — | <0.31 | 3.1± — |

Table 14: Observed aerosol backscattering coefficient ($\beta[10^{-6}/(\mathrm{sr\ m})]$), PPI-Scans for 17.09.05 and 20.09.05. Mean ($\overline{\beta}$) and standard deviation ($\sigma_\beta$) on the PPI-Scan data set, and maximum source contribution ($\Delta\beta$: maximum increase on $\beta$, when compared to the farm upwind region) averaged over the data set length. Values compiled from Lammel *et al.* (2007, Table 4.7 and Table 4.8), for lidar data set description see Table 8.

A direct comparison between the 15 min average aerosol backscattering coefficient from the lidar measurements and model simulations (Figure 20) for the 20.09.05 around 16 : 00[UTC] shows, that the model simulations managed to represent the intensity of the farm contribution, but failed to capture the shape of the farm plume and the intensity of the background fluctuations. The background

values seem to be better represented by the HAER scenarios. The lack of smaller structures can be attributed to the difference between the spatial resolutions of measurements and model ($\Delta r = 3$ m and $\Delta x = \Delta y = 50$ m, respectively). In addition, the LES model simulates the filtered values of each variable (Section 2.2), i.e. it simulates for each grid point the mean value on a sub-grid volume (disregarding sub-grid variability), while the aerosol backscattering coefficients derived from the lidar measurements retain part of the original variability[1].

The structure shown in Figure 20a can be caused by the change of the aerosol towards a more hygroscopic composition or by the vertical structure of the plume captured in the 2.26° PPI-Scan. Unfortunately, this measurement is not part of a PPI-Volume-Scan. Therefore, all the available information about the vertical structure of the farm plume is contained in this single PPI-Scan. There is no information about the aerosol composition of 20.09.05 to test the composition change hypothesis. The model simulation for 20.09.05 were conducted under the assumptions of the aerosol composition derived from the ground measurements of 17.09.05, which suggested no change of the aerosol hygroscopic properties.

The discrepancy of the farm plume shape between the model simulations and the lidar observations at 2.26° of elevation, can be explained through the difference between the vertical resolution of the model domain and the scanning pattern of the lidar. The entry point of the farm emissions into the model domain is the grid-point on top of the farm location at the lowermost model domain (10 m height) instead of the top of the farm chimney (approximately 7 m height). This 3 m discrepancy on the vertical location of the emission point, translate for an 2.26° PPI-Scan to a 76 m displacement on the radial direction of the lidar scanning pattern. At an elevation of 2.26° the model vertical resolution ($\Delta z = 20$ m) is roughly equivalent to 500 m on the radial direction of the lidar scanning pattern. The model vertical resolution should be reduced to about 1.2 m, in order to match lidar measurements with a 30 m radial resolution with this low elevation. Therefore, the current model vertical resolution, and any other pratical vertical resolution, would be insufficient to capture the vertical structure of the farm plume in such detail as shown in Figure 20a.

### 5.2.4 *Discussion*

The LES-AOP model proved to be a useful tool to determine the presence or absence of observable structures attributable to the farm plume on the lidar data-sets,

1 In order to improve the noise to signal ratio, a 30 m gliding mean was used on each lidar data set during post-processing. Such an average will smooth out the data, while retaining a fraction of the sub average scale variability.

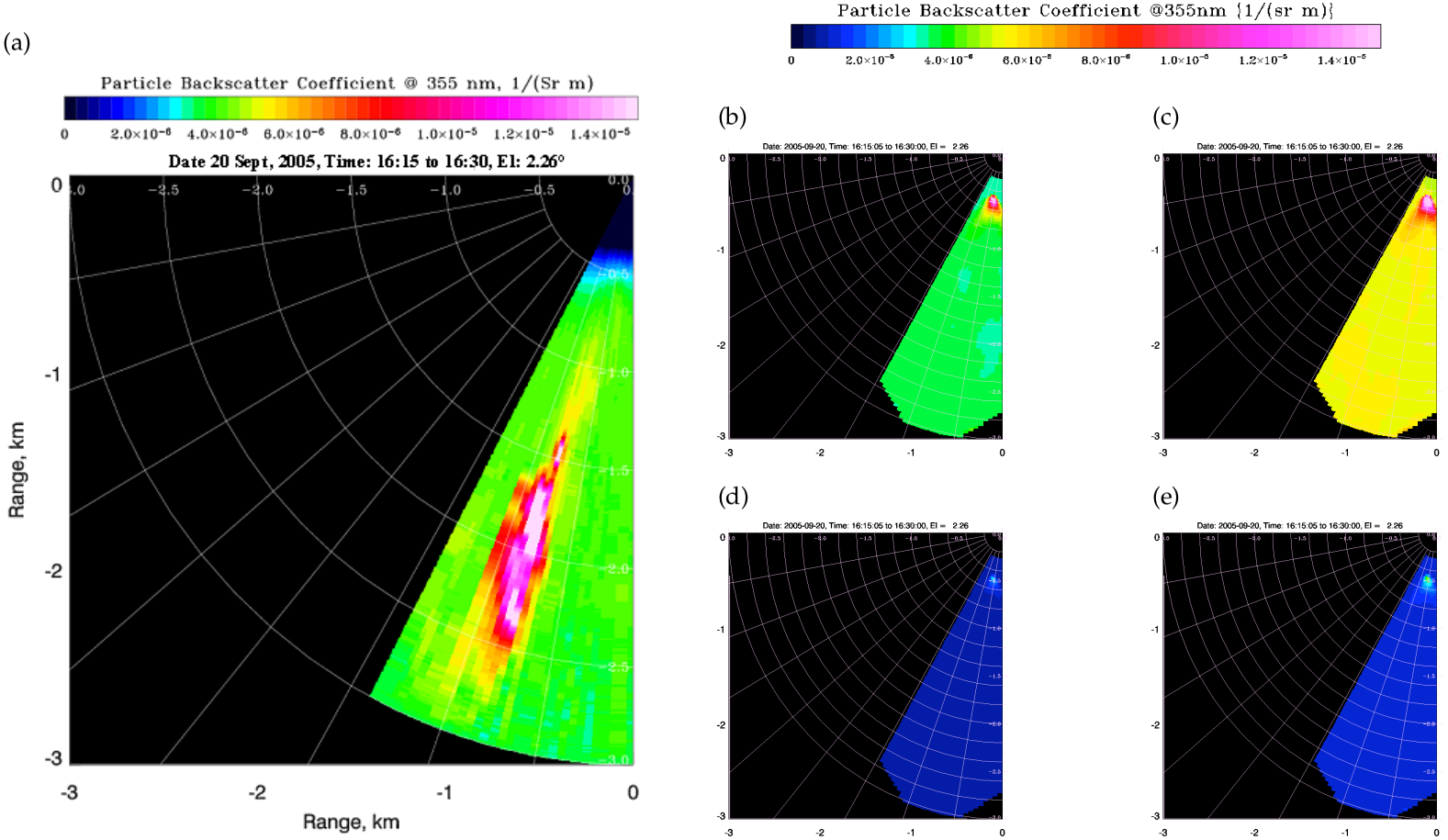


Figure 20: Observed and simulated aerosol backscattering coefficients for 20.09.05, 16 : 15 – 16 : 30[UTC] averaged PPI-Scans for: UHOH lidar measurements (a), and model results under the HAER-LWAT (b), HAER-HWAT (c), LAER-LWAT (d) and LAER-HWAT (e) aerosol scenarios. Figure (a) from Pal (2009).

helping to eliminate false positives in the search for the farm plume on the 17.09.05 4.76° PPI-Scans. It indicates that the farm plume stayed close to the ground on this day. From the experience of the PLUS1 measurement campaign on the current location, in order to capture and study the farm emission plume, lidar measurements should follow the PPI-Scan and PPI-Volume-Scan pattern starting at low elevations ($\leqslant 2°$). Pal (2009) showed an intercomparison among three different PPI scans performed during the PLUS1 measurement campaign to assess the applicability of a suitable strategy to detect the emission from the farm and to illustrate the complexities involved in the aerosol emission and transport processes. Fast consecutive PPI-Scans at constant elevation would allow statistical comparison with model simulation. Periodic PPI-Volume-Scans (e.g. every hour) could be used to investigate the vertical structure of the farm plume and its evolution during daytime.

The steady decrease of the background aerosol backscattering coefficient indicates that the assumption for the initial vertical profile of the aerosol NSD overestimated the particle number concentration at the lowermost model level. Further investigation is needed in other to find a suitable way to determine the initial vertical profile of the aerosol NSD. The model vertical resolution should be increased close to the ground in order to compare with low elevation scans. The vertical extension of the model domain (currently 2 km) should be increased in order to prevent numerical artifacts as the ones observed in the upper model domain on the 17.09.05 simulations. The computational cost of each simulation for the 17.09.05 ranged between 50 and 200 CPUh (computer hours) per hour of simulation, depending on the aerosol bin scheme configuration and daytime. The simulations for the 20.09.05 required roughly half of the CPU time. Increased vertical domain and resolution will result in an even greater computational demand.

To resolve the turbulent motions, LES models need finer resolution near to the ground than in the mid boundary layer (Sullivan *et al.*, 1996). Increased near ground resolution reduces the under resolved region and improves LES predictions (Khanna and Brasseur, 1997). Increasing the vertical resolution near to the ground by *grid stretching* increases the risk of numerical instability (Cook, 1999). A vertically nested grid refinement (i.e. nested uniform grids of the same horizontal resolution and extent, with increasing vertical resolution near to the ground) offers a computationally efficient solution to the need of increasing both vertical extension of the model domain and vertical resolution near to the ground. Vertically nested grids have been previously developed for other LES implementations (Cook, 1999; Sullivan *et al.*, 1996) improving the reliability of the results near to the ground with relatively low computational overhead. Model development on the representation of the aerosol composition, coagulation and

hygroscopicity is needed in order to test the effect of the change on the aerosol composition in the aerosol backscattering coefficient of the far plume.

The lack of the lidar low elevation measurements and of farm emission evidence in the lidar data sets during the intensive measurement period of the PLUS1 measurement campaign (15.–17.09.05), prevented the acquisition of a consistent data set of ground level aerosol composition and lidar farm plume images. Thus, leaving the analysis of the observed farm plume structure to a large degree of speculation. The observed plume on 20.09.05 does not provide a perfect base for comparison with model simulations, as these relies on the aerosol scenarios constructed from measurements for 17.09.05. Further measurements and model simulations would be needed to investigate relevance of the different aerosol processes on the observed shape of the farm plume.

# 6

# CONCLUSIONS & OUTLOOK

As part of the BWPLUS project number Z03K23005, the LES-AOP model was developed and applied to simulate the evolution of 3-D fields representing the aerosol backscattering coefficient in the vicinity of a livestock farm in northern Germany during two days in late summer of 2005. The comparison with aerosol backscattering coefficients derived from lidar measurements obtained during the PLUS1 measurement campaign showed that the model was able to simulate the observed values corresponding to the background aerosol.

By construction, the LES-AOP model resolve the equations of motion for filtered variables. Therefore, the model can only capture structures of much larger size than its spatial resolution. Low elevation scans demand from the model a vertical resolution beyond any practical application, in order to be fairly compared with observations when projecting model results into the geometry of the lidar observations. This may explain the absence in the model results of small structures like the ones observed in the lidar measurements of the background aerosol.

The use of model simulations is advisable at the designing stage of future measurement campaigns, to be conducted for the same or similar locations. Model results can assist on the design of the scanning patterns and ensure that the farm plume would be captured in most of the measurements. In its current development stage, the LES-AOP model applicability to the design of the lidar scanning pattern is limited by its high computational demand. However, the model usefulness of the evaluation of the scanning patterns is evident. The model results can be used to discard false positives when searching for evidence of the farm plume on the lidar scans. This was the case on the 17.09.05, where model results showed that the farm plume was lower than the elevation of the lidar measurements.

In addition to simulate the observable aerosol optical properties, results from the LES-AOP model were used to estimate the farm emission strength for the 17.09.05. This showed its potential for retrieving aerosol parameters not explicitly available from measurements. Further model development is needed in order

to study the composition change of the farm plume aerosol and its effect on the aerosol optical properties.

An improved version of the LES-AOP model would be needed to assess the changes of the aerosol particle number (wet) size distribution (NSD) and composition due to the farm emission and their influence on the aerosol optical properties. With the inclusion of particle coagulation, the LES-AOP model could assess the aerosol NSD and mixing dynamics. In addition to the previously implemented gas phase chemistry and the aerosol nucleation modules, the inclusion of condensation of gases (other than water) onto the pre-existing particles, is needed to study the chemical dynamics of the aerosol composition. The LES-AOP model with its high spatial and temporal resolution approach would thus offer an insight view to the 3-D structure and temporal evolution of the aerosol properties.

A simplified version of the LES-AOP model could be used, before a measurement campaign, to characterise the expected vertical structure of the farm plume under different emission and stratification scenarios. Increased model resolution close to the ground would improve the comparability of model results with low elevation lidar scans.

The current LES-AOP model version is the result of a tradeoff between computational costs and number of aerosol processes included. The computational demand of the current aerosol module is the main restriction to the model applications. An improved aerosol module should allow to easily switch off some of the aerosol processes depending on the model application. This flexible process description could be used to construct three aerosol module configurations of increasing complexity and processes comprehension:

BASIC: The basic configuration would consist of a simplified version of the current LES-AOP model, with only two internally mixed aerosol species (background and farm contribution) and a minimum of two size bins for aerosol specie (with aerosol loads scenarios derived from different $PM_{2.5}$ and $PM_{10}$ measurements upwind and downwind from the farm).

INTERMEDIATE: The intermediate configuration would consist of the current LES-AOP model plus particle coagulation (neglecting gas phase chemistry, nucleation and gas condensation).

FULL: As its name suggests, the full configuration would consist of the current LES-AOP model plus particle coagulation, gas phase chemistry, nucleation and gas condensation.

The *basic* configuration could be used to produce results comparable with the lidar observations, to study the 3-D structure of the farm plume under different

scenarios for stratification, aerosol load, composition and mixing state. Results from the *basic* configuration can contribute to the design and evaluation of the lidar scanning patterns regarding the farm plume height and intensity.

The *intermediate* configuration could be used to study the temporal evolution of the NSD, mixing state and optical properties of the background aerosol for selected scenarios derived from measurements. Results from the *intermediate* configuration can improve the aerosol vertical profiles used to initialise the aerosol module. Results from both *basic* and *intermediate* configurations can be used to study the sensitivity of the optical properties to the representation of the background aerosol (number of size bins and aerosol species), and to its initialisation (composition and mixing state).

The *full* configuration could be used to assess changes of the aerosol NSD and composition due to the farm emission, and their influence on the aerosol optical properties. Combined results from the three configurations could be used to study the sensitivity to each aerosol process on the optical properties of the background aerosol and the lidar observations of the farm polluted aerosol. The high computational demand of the LES approach puts a limit to the number of the aerosol processes included in the LES-AOP model, and the complexity and detail of the parametrisation of such processes.

Depending on the application, LES-AOP model results can be complemented with results from other models. A Reynolds-averaged Navier-Stokes (RANS) model[1] forced by a weather forecast model could be used to test the lidar scanning patterns before the actual measurements. The LES-AOP model could assist in the evaluation of the lidar scanning patterns, specially regarding the detection limit of the farm plume for the instantaneous scans (which is not possible with the RANS approach).

Multi-wavelength lidar data (as currently provided by the UHOH scanning aerosol lidar system) allows the retrieval of aerosol size and composition parameters. Thus, allowing model and measurement comparison of not only the aerosol backscatering coefficients, but also of modeled and retrieved aerosol NSD. In addition, it provides an improved framework to the study of the temporal evolution of the aerosol NSD and composition, as well as to the validation of the assumptions underlaying the LES-AOP model (or any other aerosol model).

Consistent data-sets of lidar and ground measurements characterising the background aerosol and its change downwind from the farm are indispensable requirements for reliable LES-AOP model simulations. Since the PLUS1 measurement campaign the UHOH scanning aerosol lidar system has been further developed.

1 The RANS approach differs from the LES formulation as the equations of motion are filtered in time instead of space.

Real-time visualisation of the aerosol backscattering coefficient is now possible, allowing to see the structure of the farm plume and identify other possible aerosol sources during the measurements. Thus, the UHOH scanning aerosol lidar system now permits to evaluate and correct the lidar scanning pattern in real-time. Additionally, the develoment of a scanning rotational Raman lidar enables the direct and simultaneous measurement of temperature, aerosol extinction and backscattering coefficients (Radlach, 2009; Radlach *et al.*, 2006). Multi-wavelength lidar measurements enables the retrieval of particle size distribution and composition parameters, providing a better framework for comparison with model results.

The improvement of the experimental setup could increase the knowledge about the meteorological situation and the aerosol properties near to the ground, thus improving the quality of the model simulations. First, a weather station should be employed to keep record of the pressure, temperature, humidity, as well as wind velocity and direction at the ground location nearest to the farm. The inclusion of $PM_{2.5}$ and $PM_{10}$ filters and the trace gases samplers (denuders) at the upwind location would allow to perform simultaneous upwind/downwind measurements, providing a better base for the estimation of the farm contribution to the aerosol load. The addition of a *tandem differential mobility analyser* (TDMA) to the upwind site would help to characterise the hygroscopic properties and degree of mixing of the background aerosol. Finally, a *nephelometer* located at the upwind site would help to characterise the optical properties of the background aerosol.

# APPENDIX A

## AEROSOL ABSORPTION AND BACKSCATTERING

This section is mainly based on Boheren and Huffman (1983), for a more detailed description, please refer to Boheren and Huffman (1983) or Wiscombe (1980)[1]. To make the notation easier, the reference to the position in space will be omitted in this section.

### A.1 COMPLEX REFRACTIVE INDEX

The complex refractive index (CRI) is the physical parameter describing the behaviour of an electromagnetic wave when travelling through a given material compared with its behaviour in vacuum. The CRI is a complex number (with real and imaginary parts), its real part is the ratio of the speed of light in a vacuum to the speed within the medium, and its imaginary part is related to the absorptivity of the medium. It can be represented by $m(\lambda) = n(\lambda) \pm i \cdot k(\lambda)$, where $\lambda$ is the wavelength, $n(\lambda)$, $k(\lambda)$ are no negative real numbers which can be found in the literature under the names of index of refraction and the extinction coefficient.

The relative complex refractive index (RCRI), defined as $m = \frac{m}{m_{air}}$, takes into account the fact that in the case of aerosol (particles), light travels through air before interacting with the particles.

In the following, the sign convention for the mathematical formulation of the time dependence of an electromagnetic plane wave ($e^{\mp iwt}$) will be taken according to Boheren and Huffman (1983), where it is chosen to be $e^{-iwt}$, and consequently $m(\lambda) = n(\lambda) + i \cdot k(\lambda)$.

If the aerosol specie contains hygroscopic material, the RCRI will change as the particle gains or loses water due to changes in the ambient humidity. In the case

1 The reader should be aware that Boheren and Huffman (1983) and Wiscombe (1980) follow a different sign conventions.

of a spherically homogeneous aerosol particle, this can be easily parameterised by a spherical volume interpolation, such as:

$$m_*^{aer} = \frac{r_{dry}^3}{r_p^3}\, m_{dry}^{aer} + \frac{r_p^3 - r_{dry}^3}{r_p^3}\, m^{H_2O}$$

where $r_p$ is the particle radius, $m_{dry}^{aer}$ and $m^{H_2O}$ stand for the RCRI of the *"dry"* aerosol and water.

A more general form of this relation, for internally mixed aerosol, composed of an insoluble core and a water soluble shell is:

$$m_*^{shl} = \frac{\varepsilon_v\, r_{dry}^3\, m_{dry}^{shl} + (r_p^3 - r_{dry}^3)\, m^{H_2O}}{r_p^3 - (1-\varepsilon_v)\, r_{dry}^3}$$

where $m_*^{shl}$ and $m_{dry}^{shl}$ represents the RCRI of the aerosol shell and the dry shell, and $\varepsilon_v$ the volume fraction of soluble material in the (dry) aerosol.

Complex refractive index values of water for different wavelength ($\lambda$) can be found in Hale and Querry (1973) and for several dry aerosol components in Shettle and Fenn (1979)[2]. The specific values used in this work are summarised in Table 15.

| Aerosol | Density | CRI 0.355 | | CRI 1.453 | |
|---|---|---|---|---|---|
| Component | $\rho$ [g/cm$^3$] | n [–] | k [–] | n [–] | k [–] |
| Water Soluble | 1.8 | 1.530 | 5.000E-03 | 1.510 | 1.911E-02 |
| Water Insoluble | 2.0 | 1.530 | 8.000E-03 | 1.458 | 8.000E-03 |
| Soot | 1.0 | 1.750 | 4.645E-01 | 1.760 | 4.503E-01 |
| Sea Salt | 2.2 | 1.509 | 2.946E-07 | 1.470 | 3.646E-04 |
| Water | 1.0 | 1.345 | 1.345E+00 | 1.321 | 1.321E+00 |

Table 15: Properties of the aerosol dry components and water: Density and complex refractive index (CRI), for the different aerosol components used in this work. The values for the CRI for $\lambda = 0.355$ and 1.453 $\mu$m (CRI $_{0.355}$ and CRI $_{1.453}$) were obtained by linear interpolation from the values at available wavelengths found in Hale and Querry (1973) and the FTP distribution of OPAC Hess *et al.* (1998).

2 While accessibility to Shettle and Fenn (1979) is rather limited, the CRI values can be also found via the FTP distribution of OPAC (Hess *et al.*, 1998) and in the HITRAN database (Rothman *et al.*, 2005)

## A.2 EXTINCTION AND BACKSCATTERING COEFFICIENTS OF A MIXED AEROSOL POPULATION

According to the theory of *Absorption and Scattering of light by small particles*, the aerosol extinction and backscattering coefficients of an aerosol population described as an external mixture of different aerosol species, can be obtained as the sum of the coefficients of each aerosol species ($aer$).

$$\alpha^{par} = \sum_{aer} \alpha^{aer}$$
$$\beta^{par} = \sum_{aer} \beta^{aer}$$

and from these quantities an aerosol lidar ratio can be defined as $S_L^{par} = \frac{\alpha^{par}}{\beta^{par}}$. The underlying assumptions are:

SINGLE SCATTERING: the light *"bounces only one time"* between the source and the observer.

PARALLEL LIGHT: the incident light is composed of parallel light beams.

ADDITIVITY: the extinction, absorption and backscattering coefficients of a mixture of particles can be obtained as the sum of the coefficients of each individual particle.

For a specific aerosol specie ($aer$) the extinction and backscattering coefficients can be obtained from the extinction efficiency ($Q_{ext}^{aer}$), the backscattering efficiency ($Q_{bsc}^{aer}$) and the aerosol NSD ($n^{aer}$). This relationship can be described as follows:

$$\alpha^{aer} = \int_{r_p \in \mathbb{R}_+} Q_{ext}^{aer}(r_p)\, \pi r_p^2\, n^{aer}(r_p)\, \mathrm{d}\, r_p$$
$$\beta^{aer} = \int_{r_p \in \mathbb{R}_+} Q_{bsc}^{aer}(r_p)\, \pi r_p^2\, n^{aer}(r_p)\, \mathrm{d}\, r_p$$

## A.3 EXTINCTION AND BACKSCATTERING EFFICIENCIES OF AN AEROSOL SPECIE

The extinction and backscattering efficiencies are functions of the particle structure, composition and size.

*Mie theory* provides an analytical solution for the scattering of light by spherical particles, which can also be used for stratified spheres (shell structures). In the aerosol module, $Q_{ext}^{aer}$ and $Q_{bsc}^{aer}$ are calculated for a *homogeneous sphere* and for a *coated sphere* using the code provided by Boheren and Huffman (1983, Appendix A and B).

### A.3.1 *Homogeneous Structure*

For an aerosol species describing spherical particles of homogeneous composition, the extinction and backscattering efficiencies can be described as follows:

$$Q_{ext}^{aer}(r_p) = Q_{ext}(x(r_p), m_*^{aer}) \tag{A.1}$$
$$Q_{bsc}^{aer}(r_p) = Q_{bsc}(x(r_p), m_*^{aer}) \tag{A.2}$$

where $x(r_p) = \frac{2\pi}{\lambda} r_p$ is the size parameter and $m_*^{aer}$ is the RCRI of the component of the aerosol particle.

From the *Mie theory*, the extinction and backscattering efficiencies can be expressed as follows:

$$Q_{ext}^{aer} = \frac{2}{x^2} \sum_{n \geqslant 1} (2n+1) Re(a_n + b_n) \tag{A.3}$$
$$Q_{bsc}^{aer} = \frac{1}{x^2} |\sum_{n \geqslant 1} (2n+1)(-1)^n (a_n - b_n)|^2 \tag{A.4}$$

where $a_n = a_n(x(r), m_*^{aer})$ and $b_n = b_n(x(r), m_*^{aer})$ are complex numbers, derived from the spherical *Bessel Functions* (Wiscombe, 1980).

### A.3.2 *Heterogeneous Structure*

For an aerosol specie describing spherically symmetrical particles, with a simple two layer shell structure, namely a water insoluble *core* and a water soluble *shell*, the extinction and backscattering efficiencies follow the same functional relations as in the homogeneous case, but the coefficients in equations (A.1) and (A.2) depend on the radial variation of the composition, i.e.:

$$Q_{ext}^{aer}(r_{cor}, r_{man}) = Q_{ext}(x(r_{cor}), m_*^{cor}, x(r_{man}), m_*^{shl}) \tag{A.5}$$
$$Q_{bsc}^{aer}(r_{cor}, r_{man}) = Q_{bsc}(x(r_{cor}), m_*^{cor}, x(r_{man}), m_*^{shl}) \tag{A.6}$$

where $r_{cor}$ is the radius of the aerosol water insoluble core and $r_{man} = r_p$ the particle radius, $x(r_{cor})$ and $x(r_{man})$ the size parameter of the aerosol core and shell, $m_*^{cor}$ and $m_*^{shl}$ the RCRI of the core and shell.

Note that, under the previous notation, $r_{cor} = \sqrt[3]{1-\varepsilon_v}\, r_{dry}$ and $r_{man} = r_p$. And note that the relation between the mass fraction ($\varepsilon_m$) and the volume fraction ($\varepsilon_v$) of soluble material in the (dry) aerosol is simply $\frac{\varepsilon_m}{\varepsilon_v} = \frac{\rho_s}{\rho_p}$.

Finally, the coefficients of equations (A.3) and (A.4) are functionally described by: $a_n = a_n(x(r_{cor}), m_*^{cor}, x(r_{man}), m_*^{shl})$ and $b_n = b_n(x(r_{cor}), m_*^{cor}, x(r_{man}), m_*^{shl})$.

# APPENDIX B

## AEROSOL WATER UPTAKE

The Köhler curve (equation (3.8)), describe the relation between particle wet size and the ambient conditions. It assumes that the aerosol size is in equilibrium with the ambient humidity. The term representing the solute effect or hygroscopicity, B in equation (3.9) can be re-written as:

$$B = \varepsilon_m \tilde{B} = \varepsilon_m \frac{\upsilon M_w \rho_p \phi_s}{M_s \rho_w}$$

where $\varepsilon_m$ is the mass fraction of water soluble material in the dry aerosol, $\upsilon$ the total number of ions of the water soluble material when fully dissociated, $\phi_s$ the practical osmotic coefficient of the water soluble material, and $M_w$, $M_s$, $\rho_w$ and $\rho_s$ represent the molar weight and the densities of the water and the aerosol water soluble part.

Two parametrisations were implemented in the aerosol module for the hygroscopicity. Both assume the mass fraction of soluble material in the dry aerosol ($\varepsilon_m$) to be constant over the model simulation. An example of the effect on the particle size of these two representations can be found in Figure 2.

The first representation describes the hygroscopicity coefficient ($\tilde{B}$) as a polynomial function of the ambient relative humidity (U). The values used in this work are listed in Table 16.

The second representations requires to specify the values for the water soluble component of the dry aerosol for the total number of ions when fully dissociated ($\upsilon$), the molar weight ($M_s$), the density ($\rho_s$) and the practical osmotic coefficient ($\phi_s$). The values for $\phi_s$ used in this work are listed on Table 17.

| Aerosol Type | Continental (Hamburg) | | | Continental (Deuselbach) | |
|---|---|---|---|---|---|
| Size Range | Aitken | Large | Gigant | Large | Gigant |
| $r_p$ [µm] | $< 0.1$ | $0.1 - 1.0$ | $> 1.0$ | $0.1 - 1.0$ | $> 1.0$ |
| $a_0$ | 8.010E+00 | -1.453E+00 | 2.140E+00 | -1.240E+00 | -3.421E-01 |
| $a_1$ | -1.205E+00 | 2.306E-01 | -3.183E-01 | 1.968E-01 | 4.847E-02 |
| $a_2$ | 7.639E-02 | -1.352E-02 | 2.023E-02 | -1.154E-02 | -1.257E-03 |
| $a_3$ | -2.525E-03 | 4.106E-04 | -6.670E-04 | 3.504E-04 | 5.930E-06 |
| $a_4$ | 4.724E-05 | -7.051E-06 | 1.233E-05 | -6.017E-06 | 3.968E-07 |
| $a_5$ | -5.040E-07 | 6.919E-08 | -1.280E-07 | 5.904E-08 | -7.608E-09 |
| $a_6$ | 2.863E-09 | -3.590E-10 | 6.997E-10 | -3.063E-10 | 4.849E-11 |
| $a_7$ | -6.742E-12 | 7.534E-13 | -1.577E-12 | 6.429E-13 | -9.582E-14 |

Table 16: Hygroscopicity coefficients: the values for the polynomial representation of the hygroscopicity coefficient as function of the ambient relative humidity ($\tilde{B} = \sum_i a_i U^i$) were derived from the values for the empirical growth coefficients for aerosol particles found in Winkler (1988).

| Salt | NaCl | $NH_4NO_3$ | $(NH_4)_2SO_4$ |
|---|---|---|---|
| $\phi_s$ | 9.180E-01 | 7.923E-01 | 6.632E-01 |

Table 17: Practical osmotic coefficients: the values for the practical osmotic coefficient ($\phi_s$) were derived from the values for the osmotic coefficient for different molalities found in Robinson and Stokes (1959).

# APPENDIX C

## GRAVITATIONAL SETTLING

The falling of a particle in a viscous fluid is characterised by the *Reynolds Number*, which describes the ratio between the inertial and viscous force in the flow:

$$Re_r = \frac{r_p u_\infty}{\nu} \approx \frac{|\mathbf{u} \cdot \nabla \mathbf{u}|}{|\nu \nabla^2 \mathbf{u}|}$$

where $\nu$ stands for the kinematic viscosity of the fluid, $\mathbf{u}$ for the velocity, $r_p$ for the particle radius and $u_\infty$ for it's terminal velocity.

An alternative, and more widely used definition of the *Reynolds Number*, is based on the particle diameter $d_p$:

$$Re = \frac{d_p u_\infty}{\nu} = 2Re_r$$

In this work the definition based on the diameter will be used.

### C.1 STOKES LAW

For a small *Reynolds Number* the drag force can be described by the *Stokes Law*, which in the case of air is described by:

$$F_{drag} = 6\pi\rho_{air}\nu_{air}r_p u_\infty \tag{C.1}$$

where $\rho_{air}$ and $\nu_{air}$ are the air density and kinematic viscosity.

Under the *Stokes Law* regimen, the equilibrium between the gravitational force and the drag force over a rigid spherical particle, determines the settling velocity ($v_s = u_\infty$), which can be calculated as follows:

$$v_s = \frac{2\rho_p\, g}{9\rho_{air}\nu_{air}} r_p^2 \tag{C.2}$$

where $g$ represents the gravitational acceleration, $r_p$ and $\rho_p$ the particle radius and density.

Unfortunately this assumption is not always true. To take into account the inertia in the drag force, $F_{drag}$ can be described as:

$$F_{drag} = C_D \, A_p \, \rho_p \frac{u_\infty^2}{2} \tag{C.3}$$

where $A_p = \pi r_p^2$ is the particle cross section to the flow and $C_D$ is the drag coefficient defined as (Seinfeld and Pandis, 1998):

$$C_D = \begin{cases} \frac{24}{Re} & Re < 0.1 \ (\textit{Stokes Law}) \\ \frac{24}{Re}\left[1 + \frac{3}{16}Re + \frac{9}{160}Re^2 \ln(2Re)\right] & 0.1 < Re < 2 \\ \frac{24}{Re}\left[1 + 0.15Re^{0.687}\right] & 2 < Re < 500 \\ 0.44 & 500 < Re < 2 \cdot 10^5 \end{cases}$$

Fortunately a simple comparison of the values for the settling velocity as described by equations (C.1) and (C.3) for aerosol particles in the size range simulated by the aerosol module, shows that the effects of assuming the *Stokes Law* can be neglected (Section 3.4 and Figure 5).

## C.2 CUNNINGHAM CORRECTION FACTOR

The *Stokes Law* (C.1) assumes a *"continuum medium"*. This is not the case when the particle radius ($r_p$) is of the same order of magnitude as the mean free path of the fluid, in this case air ($\lambda_{air}$), which can be calculated as:

$$\lambda_{air} = \frac{2\nu_{air}}{\sqrt{\frac{8M_{air}}{\pi RT}}} = \nu_{air}\sqrt{\frac{\pi}{2}R_{air}T}$$

where $M_{air} = 28.8 \ gr/mol$ is the air's molecular weight.

For small particles the *"continuum medium"* assumption will lead to an over-estimation of the drag force and therefore to a under-estimation of the particle settling velocity. To take into account the non-continuity effects the *Cunningham Correction Factor* ($C_c$) is introduced into the *Stokes Law* (C.1) leading to:

$$F_{drag} = \frac{6\pi\rho_{air}\nu_{air}r_p u_\infty}{C_c} \tag{C.4}$$

where the *Cunningham Corrector* is defined as:

$$C_c = 1 + K_n[1.257 + 0.4\, e^{\frac{-1.1}{K_n}}]$$

and $K_n = \frac{\lambda_{air}}{r_p}$ is the *Knudsen Number* of the air.

Finally the settling velocity ($v_s$) (C.2) can be corrected by $C_c$:

$$v_s = \frac{2\rho_p \, g \, C_c}{9\rho_{air}\nu_{air}} r_p^2 \tag{C.5}$$

# APPENDIX D

## DRY DEPOSITION

The dry deposition is the removal from the atmosphere due to deposition on the ground surface and its vegetation cover. This process can be described by the deposition velocity for gaseous species ($v_d^{gas}$) and for particles ($v_d^{par}$) defined as follows:

$$\begin{aligned} v_d^{gas} &= \frac{1}{R_a + R_b + R_c} \\ v_d^{par} &= \frac{1}{R_a + R_b + R_a\, R_b\, v_s} + v_s \end{aligned} \tag{D.1}$$

where $R_a$, $R_b$ and $R_c$ stand for the aerodynamic transport resistance, the boundary layer resistance and the canopy resistance respectively, $v_s$ is the settling velocity described in equation (C.2).

In the following sections the focus will be on the deposition velocity for particles, which will be denoted as $v_d(r_p)$, where $r_p$ represent the particle radius. For a more detailed description please refer to Seinfeld and Pandis (1998); Zufall and Davidson (1998).

Equation (D.1) assumes that the dry deposition can be represented by a series of resistances acting in parallel with the gravitational settling (Figure 21). It also assume that the aerosol particles adhere to the surface upon contact ($R_c = 0$), and therefore $n_p^{z_{veg},b}(r_p) = n_p^{z_{veg},c}(r_p) = 0$. The flux of particles leaving the model domain due to dry deposition can be therefore calculated as:

$$\begin{aligned} -F_{dep}^{n_p}(r_p) &= v_d(r_p)\, n_p^{z_r}(r_p) \\ &= \frac{n_p^{z_r}(r_p) - n_p^{z_0}(r_p)}{R_a} + v_s(r_p)\, n_p^{z_r}(r_p) \\ &= \frac{n_p^{z_r}(r_p)}{R_b(r_p)} + v_s(r_p)\, n_p^{z_0}(r_p) \end{aligned}$$

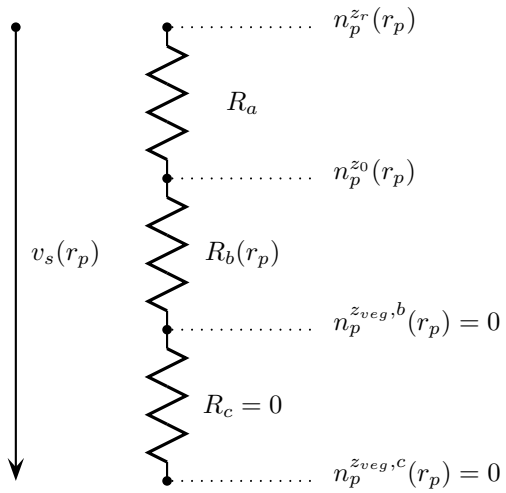


Figure 21: Resistance scheme of the aerosol dry deposition.

## D.1 AERODYNAMIC TRANSPORT RESISTANCE

The calculation of the aerodynamic transport resistance ($R_a$) assumes that turbulent transport is the prevalent transport mechanism between the lowermost model level and some distance above the ground surface and its vegetation cover. From Monin-Obukhov similarity theory, the formulation of the eddy diffusivity leads to the following formulation for $R_a$:

$$R_a = \frac{1}{\kappa u_*} \int_{z_o}^{z_r} \phi_c \left(\frac{z}{L}\right) \frac{dz}{z}$$

where $z_r$ is the height, $z_0$ the roughness length $\kappa = 0.4$ the *von Karman's constant*, $u_*$ the friction velocity, $L$ the Obukhov length, $\phi_c$ is a stability function.

For consistency with the parametrisations of the LES model, it is assumed that $\phi_c = \phi_h$, where $\phi_h$ is the stability function for heat, described in Webb (1982) and Chlond (1998a) as:

$$\phi_h \left(\frac{z}{L}\right) = \begin{cases} 1 + 9.2\frac{z}{L} & \frac{z}{L} > 0 \quad (\textit{stable}) \\ 1 & \frac{z}{L} = 0 \quad (\textit{neutral}) \\ \left(1 - 12.2\frac{z}{L})\right)^{-1/2} & \frac{z}{L} < 0 \quad (\textit{unstable}) \end{cases}$$

Finally:

$$R_a = \begin{cases} \frac{1}{\kappa u_*}\left[\ln\left(\frac{z_r}{z_0}\right) + 9.2\frac{z_r - z_0}{L}\right] & (\textit{stable}) \\ \frac{1}{\kappa u_*}\ln\left(\frac{z_r}{z_0}\right) & (\textit{neutral}) \\ \frac{1}{\kappa u_*}\left[\ln\left(\frac{z_r}{z_0}\right) + \ln\left(\frac{(\eta_0+1)^2}{(\eta_r+1)^2}\right)\right] & (\textit{unstable}) \end{cases}$$

where $\eta_r = \sqrt{1 - 12.2\frac{z_r}{L}}$ and $\eta_0 = \sqrt{1 - 12.2\frac{z_0}{L}}$.

## D.2 SURFACE LAYER RESISTANCE

In the formulation of the surface layer resistance ($R_b$), the transport between the near-ground level, the ground surface and its vegetation cover, and some distance above it is assumed to be mainly due to Brownian diffusion. Among the many different parametrisation for $R_b$ in the literature (Zufall and Davidson, 1998), the following is used in the aerosol module:

$$R_b(r_p) = \frac{2(Sc(r_p)/Pr)}{\kappa u_*}$$

where Sc and Pr stands for the *Schmidt Number* and the *Prandtl Number*, which are defined as:

$$Pr = \frac{\nu_{air}}{\kappa_{air}}$$
$$Sc(r_p) = \frac{\nu_{air}}{D_b(r_p)}$$

where $\nu_{air}$ and $\kappa_{air}$ are the kinematic viscosity and the thermal diffusivity of the air, and $D_b(r_p)$ stands for the *Brownian diffusivity* of the aerosol, described in equation (3.10) as:

$$D_b(r_p) = \frac{k_B T C_c(r_p)}{6\pi\rho_{air}\nu_{air}r_p}$$

where $r_p$ stands for the particle radius, $k_B$ is the *Boltzmann's constant*, $\rho_{air}$ and $\nu_{air}$ the air density and kinematic viscosity and $C_c(r_p)$ the *Cunningham Correction Factor* (Appendix C). Finally:

$$R_b(r_p) = \frac{2\kappa_{air}}{\kappa u_* D_b(r_p)}$$

## D.3 CANOPY RESISTANCE

It is assumed that the aerosol particles adhere to the surface upon contact, then $R_c = 0$. For completeness reasons, a formulation for $R_c$ for gaseous species is included here.

According to Zufall and Davidson (1998), following the *"Big-leaf"* model, the canopy resistance for gaseous species ($R_c$) can be described as:

$$\frac{1}{R_c} = \frac{1}{R_s(Sc/Pr) + R_m} + \frac{1}{R_{cut}} + \frac{1}{R_{soil}}$$

where $R_s$ is the stomata resistance, $R_m$ the mesophyll resistance, $R_{cut}$ the cuticular resistance, and $R_{soil}$ the resistance of the soil.

# BIBLIOGRAPHY


Atkinson, R. (1990). Gas-phase tropospheric chemistry of organic compounds: A review. *Atmospheric Environment*, 24A:1–41. (Cited on page 11.)

Behrendt, A, G. Wagner, A. Petrova, M. Shiler, S. Pal, T. Schaberl, and V. Wulfmeyer (2005). Modular lidar systems for high-resolution 4-dimensional measurements of water vapor, temperature, and aerosols. In U.N. Singh and K. Mizutani, editors, *Lidar Remote Sensing for Industry and Environment Monitoring V (Proceedings of SPIE 5653)*, pages 220–227. Honolulu, Hawaii, USA. (Cited on page 2.)

Betts, A.K. (1973). Non-precipitating cumulus convection and its parameterization. *Quarterly Journal of the Royal Meteorological Society*, 99:178–196. (Cited on page 7.)

Böckmann, C (2001). Hybrid regularization method for the ill-posed inversion of multiwavelength lidar data in the retrieval of aerosol size distributions. *Applied Optics*, 40:1329–1342. (Cited on page 72.)

Böckmann, C. and J. Wauer (2001). Algorithms for the inversion of light scattering data from uniform and non-uniform particles. *Journal of Aerosol Science*, 32:49–61. (Cited on page 72.)

Boheren, C.F. and D.R. Huffman (1983). *Absorption and scattering of light by small particles*. Wiley, New York, 530 pages. (Cited on pages 19, 20, 21, 99, and 101.)

Bott, A. (1989a). A positive definite advection scheme obtained by nonlinear renormalization of the advective fluxes. *Monthly Weather Review*, 117:1006–1016. (Cited on pages 11 and 43.)

Bott, A. (1989b). Reply. *Monthly Weather Review*, 117:2633–2636. (Cited on pages 11 and 43.)

Bucholtz, A. (1995). Rayleigh-scattering calculations for the terrestrial atmosphere. *Applied Optics*, 34:2765–2773. (Cited on pages 70 and 72.)

Buseck, P.R. and M. Pósfai (1999). Airborne minerals and related aerosol particles: Effects on climate and the environment. In *Proceedings of the National Academy of Sciences of the USA*, volume 96, pages 3372–3379. (Cited on page 27.)

Carmichael, G.R., A. Sandu, T. Chai, D.N. Daescu, E.M. Constantinescu, and Y. Tang (2008). Predicting air quality: Improvements through advanced methods to integrate models and measurements. *Journal of Computational Physics*, 227:3540–3571. (Cited on page 1.)

Carter, W.P.L. (1990). A detailed mechanism for the gas-phase atmospheric reactions of organic compounds. *Atmospheric Environment*, 24A:481–518. (Cited on page 11.)

Chlond, A. (1992). Three-dimensional simulation of cloud street development during a cold air outbreak. *Boundary-Layer Meteorology*, 58:161–200. (Cited on pages 3, 5, and 14.)

Chlond, A. (1994). Locally modified version of bott's advection scheme. *Monthly Weather Review*, 122:111–125. (Cited on pages 11, 35, and 43.)

Chlond, A. (1998a). Grobstruktursimulation - eine Methode zur Berechnung turbulenter atmosphärischer Strömungen. Examensarbeit No. 66, Max Planck Institute for Meteorology, Hamburg, 181 pages. (Cited on pages 3, 5, 7, 11, 13, 14, 34, and 110.)

Chlond, A. (1998b). Large-eddy simulation of contrails. *Journal of the Atmospheric Sciences*, 55:796–819. (Cited on pages 3, 5, 10, and 14.)

Chlond, A. and A. Wolkau (2000). Large-eddy simulation of a nocturnal stratocumulus-topped marine atmospheric boundary layer: An uncertainty analysis. *Boundary-Layer Meteorology*, 95:31–55. (Cited on pages 5 and 14.)

Clark, A.R., J.H. Ferziger, and W.C. Reynolds (1979). Evaluation of subgrid-scale models using an accurately simulated turbulent flow. *Journal of Fluid Mechanics*, 91:1–16. (Cited on page 8.)

Cook, Andrew W. (1999). A consistent approach to large eddy simulation using adaptive mesh refinement. *Journal of Computational Physics*, 154:117–133. (Cited on page 90.)

Covert, D.S., R.J. Charlson, and N.C. Ahlquist (1972). A study of the relationship of chemical composition and humidity to light scattering by aerosols. *Journal of Applied Meteorology*, 11:968–976. (Cited on page 3.)

Deardorff, J.W. (1980). Stratocumulus-capped mixed layers derived from a three-dimensional model. *Boundary-Layer Meteorology*, 18:495–527. (Cited on pages 9 and 10.)

Debry, E. and B. Sportisse (2007). Solving aerosol coagulation with size-binning methods. *Applied Numerical Mathematics*, 57:1008–1020. (Cited on pages 24 and 30.)

Doms, G. and U. Schättler (2002). A description of the nonhydrostatic regional model LM. part I: Dynamics and numerics. Technical report, Deutscher Wetterdienst, Offenbach, 134 pages. (Cited on page 76.)

Doms, G., J. Förstner, E. Heise, H.-J. Herzog, M. Raschendorfer, R. Schrodin, T. Reinhardt, and G Vogel (2005). A description of the nonhydrostatic regional model LM. part II: Physical parameterization. Technical report, Deutscher Wetterdienst, Offenbach, 133 pages. (Cited on page 76.)

Dressel, M. (1985). Dynamic shape factors for particle shape characterization. *Particle and Particle Systems Characterization*, 2:62–66. (Cited on page 32.)

Feingold, G. and S.M. Kreidenweis (2002). Cloud processing of aerosol as modeled by a large eddy simulation with coupled microphysics and aqueous chemistry. *Journal of Geophysical Research*, 107:4687. (Cited on pages 2 and 3.)

Feingold, G. and B. Morley (2003). Aerosol hygroscopic properties as measured by lidar and comparison with in situ measurements. *Journal of Geophysical Research*, 108:4327. (Cited on page 72.)

Fernald, F.G. (1984). Analysis of atmospheric lidar observations: some comments. *Applied Optics*, 23:652–653. (Cited on pages 2, 18, 70, 71, and 72.)

Fernald, F.G., B.M. Herman, and J.A. Reagan (1972). Determination of aerosol height distributions by lidar. *Journal of Applied Meteorology*, 11:482–489. (Cited on pages 2, 18, and 70.)

Fitzgerald, J.W., W.A. Hoppel, and M.A. Vietti (1982). The size and scattering coefficient of urban aerosol particles at Washington, DC as a function of relative humidity. *Journal of the Atmospheric Sciences*, 39:1838–1852. (Cited on page 3.)

Gong, W. and H. Cho (1993). A numerical scheme for the integration of the gas-phase chemical rate equations in three-dimensional atmospheric models. *Atmospheric Environment*, 27A:2147–2160. (Cited on page 11.)

Gurtin, M.E. (1981). *An Introduction to Continuum Mechanics*, volume 15 of *Mathematics in Science and Engineering*. Academic Press, New York. (Cited on page 6.)

Hale, G.M. and M.R. Querry (1973). Optical constants of water in the $200 - nm$ to $200 - \mu m$ wavelength region. *Applied Optics*, 12:555–563. (Cited on pages 27 and 100.)

Hänel, G. (1976). The properties of atmospheric particles as functions of the relative humidity at thermodynamic equilibrium with surrounding moist air. *Advances in Geophysics*, 19:73–118. (Cited on pages 22 and 27.)

Hartung, J., J. Seedorf, Th. Trickl, and H. Gronauer (1998). Freisetzung partikelförmiger Stoffe aus einem Schweinestall mit zentraler Abluftführung in die Stallumgebung. *Deutsche Tierärztliche Wochenschrift*, 105:209–252. (Cited on page 1.)

Hess, M., P. Koepke, and I. Schult (1998). Optical properties of aerosols and clouds: The software package OPAC. *Bulletin of the American Meteorological Society*, 79:831–844. (Cited on pages 21, 27, 75, 76, and 100.)

Holmen, B.A., W.E. Eichinger, and R.G. Flocchini (1998). Application of elastic lidar to pm10 emissions from agricultural nonpoint sources. *Environmental Science and Technology*, 32:3068–3076. (Cited on page 1.)

Holmen, B.A., T.A. James, L.L. Ashbaugh, and R.G. Flocchini (2001a). Lidar-assisted measurement of PM10 emissions from agricultural tilling in California's San Joaquin Valley - Part II: emission factors. *Atmospheric Environment*, 35:3265–3277. (Cited on page 1.)

Holmen, B.A., T.A. James, L.L. Ashbaugh, and R.G. Flocchini (2001b). Lidar-assisted measurement of PM10 emissions from agricultural tilling in California's San Joaquin Valley- Part I: lidar. *Atmospheric Environment*, 35:3251–3264. (Cited on page 1.)

Japar, S.M., T.J. Wallington, J.F.O. Richert, and J.C. Ball (1990). The atmospheric chemistry of oxygenated fuel additives: t-butyl alcohol, dimethyl ether, and methyl t-butyl ether. *International Journal of Chemical Kinetics*, 22:1257–1269. (Cited on page 11.)

Khanna, S. and J.G. Brasseur (1997). Analysis of Monin-Obukhov similarity from large-eddy simulation. *Journal of Fluid Mechanics*, 345:251–286. (Cited on page 90.)

Kim, Y.P. and J.H. Seinfeld (1990). Simulation of multicomponent aerosol condensation by the moving sectional method. *Journal of Colloid and Interface Science*, 135:185–199. (Cited on page 30.)

Klett, J.D. (1981). Stable analytical inversion solution for processing lidar returns. *Applied Optics*, 20:211–220. (Cited on pages 2, 18, and 70.)

Klett, J.D. (1985). Lidar inversion with variable backscatter/extinction ratios. *Applied Optics*, 24:1638–1643. (Cited on pages 2, 18, and 70.)

Kocifaj, M. and H. Horvath (2005). Inversion of extinction data for irregularly shaped particles. *Atmospheric Environment*, 39:1481–1495. (Cited on page 72.)

Koo, B., T.M. Gaydos, and S.N. Pandis (2003). Evaluation of the equilibrium, dynamic, and hybrid aerosol modeling approaches. *Aerosol Science and Technology*, 37:53–64. (Cited on page 30.)

Köpke, P., M. Hess, I. Schult, and E. Shettle (1997). Global aerosol data set. MPI-Report No. 243, Max Planck Institute for Meteorology, Hamburg, 44 pages. (Cited on page 21.)

Lammel, G. and Á.M. Valdebenito B. (2007). Aerosole aus der Nutztierhaltung (Teil A). `bwplus.fzk.de/berichte/ZBer/2007/ZBerZO3K23005+7.pdf`. In German. (Cited on page 47.)

Lammel, G., F. Schneider, E. Brüggemann, T Gnauk, A. Röhrl, and P. Wieser (2004). Aerosols emitted from a livestock farm in southern germany. *Water, Air and Soil Pollution*, 154:313–330. (Cited on pages 1, 47, and 54.)

Lammel, G., V. Wulfmeyer, S. Pal, Á.M. Valdebenito B., A. Behrendt, F. Müller, A. Petrova, and T. Schaberl (2005). Aerosole aus der Nutztierhaltung (Teil A + B). `bwplus.fzk.de/berichte/ZBer/2005/ZBerzo3k23005.pdf`. In German. (Cited on page 47.)

Lammel, G., V. Wulfmeyer, S. Pal, Á.M. Valdebenito B., A. Behrendt, F. Müller, M. Radlach, and T. Schaberl (2006). Aerosole aus der Nutztierhaltung (Teil A + B). In German. (Cited on page 47.)

Lammel, G., V. Wulfmeyer, S. Pal, Á.M. Valdebenito B., A. Behrendt, F. Müller, and M. Radlach (2007). Aerosole aus der Nutztierhaltung (Teile A und B). `www.bwplus.fzk.de/berichte/SBer/ZO3K23005+ZO3K23007SBer.pdf`. In German. (Cited on pages 47, 58, 59, 60, 80, and 87.)

Lurmann, F.W., W.P.L. Carter, and L.A. Coyner (1987). A surrogate species chemical reaction mechanism for urban-scale air quality simulation models. Technical Report No. EPA/600/3-87/014, U.S. Environmental Protection Agency, Research Triangle Park N.C. (Cited on page 11.)

Mayor, S.D. (2001). *Volume Imaging Lidar Observations and Large-Eddy Simulations of Convective Internal Boundary Layers*. Ph.D. thesis, University of Wisconsin-Madison. (Cited on pages 2 and 3.)

Mayor, S.D. and E.W. Eloranta (2001). Two-dimensional vector wind fields from volume imaging lidar data. *Journal of Applied Meteorology*, 40:1331–1346. (Cited on page 3.)

Mayor, S.D., G.J. Tripoli, and E.W. Eloranta (2003). Evaluating large-eddy simulations using volume imaging lidar data. *Monthly Weather Review*, 131:1428–1452. (Cited on pages 2 and 3.)

Mayor, Shane D., Philippe R. Spalart, and Gregory J. Tripoli (2002). Application of a perturbation recycling method in the large-eddy simulation of a mesoscale convective internal boundary layer. *Journal of the Atmospheric Sciences*, 59:2385–2395. (Cited on pages 2, 3, and 41.)

McGraw, R., P.I. Huang, and S.E. Schwartz (1995). Optical properties of atmospheric aerosols from moments of the particle size distribution. *Geophysical Research Letters*, 22:2929–2932. (Cited on pages 2 and 29.)

Mishchenko, M.I, L.D. Travis, R.A. Kahn, and R.A. West (1997). Modeling phase functions for dustlike tropospheric aerosols using a shape mixture of randomly oriented polydisperse spheroids. *Journal of Geophysical Research*, 102:16831–16847. (Cited on pages 21 and 27.)

Mishchenko, M.I., L. Liu, L.D. Travis, and A.A. Lacis (2004). Scattering and radiative properties of semi-external versus external mixtures of different aerosol types. *Journal of Quantitative Spectroscopy and Radiative Transfer*, 88:139–147. (Cited on pages 21, 27, and 28.)

Müller, F. (2004). chemistry.gasp.cross.f: A FORTRAN implementation of a photochemical mechanism extended for ternary nucleation of $H_2SO_4$-$NH_3$-$H_2O$ particles. Unpublished. (Cited on page 10.)

Müller, G. and A. Chlond (1996). Three-dimensional numerical study of cell boarding during cold-air-outbreaks. *Boundary-Layer Meteorology*, 81:289–323. (Cited on page 12.)

Newsom, R.K. and R.M. Banta (2004a). Assimilating coherent doppler lidar measurements into a model of the atmospheric boundary layer. part i: Algorithm development and sensitivity to measurement error. *Journal of Atmospheric and Oceanic Technology*, 21:1328–1345. (Cited on pages 3 and 4.)

Newsom, R.K. and R.M. Banta (2004b). Assimilating coherent doppler lidar measurements into a model of the atmospheric boundary layer. part II: Sensitivity analyses. *Journal of Atmospheric and Oceanic Technology*, 21:1809–1824. (Cited on page 3.)

Pal, S. (2009). *A mobile, scanning eye-safe lidar for the study of atmospheric aerosol particles and transport processes in the lower troposphere*. Ph.D. thesis, University of Hohenheim, Stuttgart, Germany. (Cited on pages 2, 47, 48, 49, 50, 65, 67, 69, 72, 89, and 90.)

Pal, S., A. Behrendt, M. Radlach, T. Schaberl, and V. Wulfmeyer (2006). Eye-safe scanning rotational raman lidar at 355 nm. In C. Nagasawa and N. Sugimoto, editors, *Reviewed and Revised Papers of the 23rd International Laser Radar Conference (ILRC)*. Nara, Japan. (Cited on pages 2 and 65.)

Pal, S., A. Behrendt, H. Bauer, M. Radlach, A. Riede, M. Schiller, G. Wagner, and V. Wulfmeyer (2008). 3-dimensional observations of atmospheric variables during the field campaign COPS. *IOP Conference Series: Earth and Environmental Science*, page 012031. (Cited on pages 2 and 47.)

Pirjola, L., S. Tsyro, L. Tarrason, and M. Kulmala (2003). A monodisperse aerosol dynamics module, a promising candidate for use in long-range transport models: Box model tests. *Journal of Geophysical Research*, 108:4258. (Cited on page 2.)

Pruppacher, H.R. and J.D. Klett (1978). *Microphysics of clouds and precipitation*. Reidel, Boston, 714 pages. (Cited on page 32.)

Radlach, M. (2009). *A scanning eye-safe rotational Raman lidar in the ultraviolet for measurements of tropospheric temperature fields*. Ph.D. thesis, University of Hohenheim, Stuttgart, Germany. (Cited on pages 47, 65, and 96.)

Radlach, M., A. Behrendt, S. Pal, T. Schaberl, and V. Wulfmeyer (2006). Scanning rotational raman lidar at 355 nm for the measurement of tropospheric temperature fields. In C. Nagasawa and N. Sugimoto, editors, *Reviewed and Revised Papers of the 23rd International Laser Radar Conference (ILRC)*, pages 699–702. Nara, Japan. (Cited on pages 47, 65, and 96.)

Radlach, M., A. Behrendt, S. Pal, A. Riede, and V. Wulfmeyer (2008). State-of-the-art daytime scanning temperature measurements by rotational raman lidar. In *Reviewed and Revised Papers Presented at the 24th International Laser Radar Conference (ILRC)*, pages 1056 – 1059. Boulder, CO, USA. (Cited on page 47.)

Robinson, R.A. and R.H. Stokes (1959). *Electrolyte Solutions: The Measurement and Interpretation of Conductance, Chemical Potential and Diffusion in Solutions of Simple Electrolytes*. Butterworth, London, 2nd edition, 571 pages. (Cited on pages 22, 23, 76, and 104.)

Rothman, L.S., D. Jacquemart, A. Barbe, D. Chris Benner, M. Birk, L.R. Brown, M.R. Carleer, C. Chackerian Jr., K. Chance, L.H. Coudert, V. Dana, V.M. Devi, J.-M. Flaud, R.R. Gamache, A. Goldman, J.-M. Hartmann, K.W. Jucks, A.G. Maki, J.-Y. Mandin, S.T. Massie, J. Orphal, A. Perrin, C.P. Rinsland, M.A.H. Smith, J. Tennyson, R.N. Tolchenov, R.A. Toth, J. Vander Auwera, P. Varanasi, and G. Wagner (2005). The HITRAN 2004 molecular spectroscopic database. *Journal of Quantitative Spectroscopy and Radiative Transfer*, 96:139–204. (Cited on page 100.)

Scheuch, G. and J. Heyder (1990). Dynamic shape factor of nonspherical aerosol particles in the diffusion regime. *Aerosol Science and Technology*, 12:270–277. (Cited on page 32.)

Schraff, C. and R. Hess (2005). A description of the nonhydrostatic regional model LM. part III: Data assimilation. Technical report, Deutscher Wetterdienst, Offenbach, 133 pages. (Cited on page 76.)

Schulzweida, U., L. Kornblueh, and R. Quast (2007). *CDO User's Guide*. Max Planck Institute for Meteorology, Hamburg, 156 pages. Climate Data Operators version 1.0.8. (Cited on page 77.)

Seigneur, C., A.B. Hudischewskyj, J.H. Seinfeld, K.T. Whitby, E.R. Whitby, J.R. Brock, and H.M. Barnes (1986). Simulation of aerosol dynamics: A comparative review of mathematical models. *Aerosol Science and Technology*, 5:205–222. (Cited on pages 24 and 30.)

Seinfeld, J.H. and S.N. Pandis (1998). *Atmospheric Chemistry and Physics: From Air Pollution to Climate Chage*. Wiley, New York, 1326 pages. (Cited on pages 22, 32, 34, 106, and 109.)

Shettle, E.P. and R.W. Fenn (1979). Models for the aerosols of the lower atmosphere and the effects of humidity variations on their optical properties. Technical Report No. AFGL-TR-79-0214, U.S. Air Force Geophysics Lab, Hanscom Air Force Base, USA, 94 pages. (Cited on page 100.)

Sommeria, G. and J.W. Deardorff (1977). Subgrid-scale condensation in models of nonprecipitating clouds. *Journal of the Atmospheric Sciences*, 34:344–355. (Cited on pages 6 and 10.)

Spalding, D.B. (1972). A novel finite difference formulation for differential expressions involving both first and second derivatives. *International Journal for Numerical Methods in Engineering*, 4:551–559. (Cited on pages 11 and 43.)

Stier, P., J. Feichter, S. Kinne, E. Kloster, S.and Vignati, J. Wilson, L. Ganzeveld, I. Tegen, M. Werner, Y. Balkanski, M. Schulz, O. Boucher, A. Minikin, and A. Petzold (2005). The aerosol-climate model ECHAM5-HAM. *Atmospheric Chemistry and Physics*, 5:1125–1156. (Cited on page 32.)

Sullivan, P.P., J.C. McWilliams, and C.-H. Moeng (1996). A grid nesting method for large-eddy simulation of planetary boundary-layer flows. *Boundary-Layer Meteorology*, 80:167–202. (Cited on page 90.)

Tang, I. N. (1996). Chemical and size effects of hygroscopic aerosols on light scattering coefficients. *Journal of Geophysical Research*, 101:19245–19250. (Cited on page 27.)

Upadhyay, R.R. and O.A. Ezekoye (2006). Treatment of size-dependent aerosol transport processes using quadrature based moment methods. *Journal of Aerosol Science*, 37:799–819. (Cited on page 32.)

Vignati, E., J. Wilson, and P. Stier (2004). M7: An efficient size-resolved aerosol microphysics module for large-scale aerosol transport models. *Journal of Geophysical Research*, 109:1–17. (Cited on page 2.)

von Salzen, K. and K.H. Schlünzen (1999a). A prognostic physico-chemical model of secondary and marine inorganic multicomponent aerosols I. model description. *Atmospheric Environment*, 33:567–576. (Cited on pages 2 and 30.)

von Salzen, K. and K.H. Schlünzen (1999b). A prognostic physico-chemical model of secondary and marine inorganic multicomponent aerosols II. model tests. *Atmospheric Environment*, 33:1543–1552. (Cited on pages 2, 30, and 74.)

Warren, D.R. and J.H. Seinfeld (1985). Simulation of aerosol size distribution evolution in systems with simultaneous nucleation, condensation, and coagulation. *Aerosol Science and Technology*, 4:31–43. (Cited on page 30.)

Webb, E.K. (1982). Profile relationships in the superadiabatic surface layer. *Quarterly Journal of the Royal Meteorological Society*, 108:661–688. (Cited on pages 13 and 110.)

Winkler, P. (1988). The growth of atmospheric aerosol particles with relative humidity. *Physica Scripta*, 37:223–230. (Cited on pages 23, 76, and 104.)

Wiscombe, W.J. (1979). Mie scattering calculations: Advances in technique and fast, vector-speed computer codes. Ncar Technical Note NCAR/TN-140+STR, National Center for Atmospheric Research (NCAR), 64 pages. (Cited on page 21.)

Wiscombe, W.J. (1980). Improved mie scattering algoritms. *Applied Optics*, 19:1505–1509. (Cited on pages 21, 99, and 102.)

Wu, X.A., C. Seigneur, and R.W. Bergstrom (1996). Evaluation of a sectional representation of size distributions for calculating aerosol optical properties. *Journal of Geophysical Research*, 101:19277–19283. (Cited on pages 2 and 73.)

Wulfmeyer, V. and G. Feingold (2000). On the relationship between relative humidity and particle backscattering coefficient in the marine boundary layer determined with differential absorption lidar. *Journal of Geophysical Research*, 105:4729–4741. (Cited on pages 2 and 3.)

Young, D.M.Jr. (1950). *Iterative Methods for Solving Partial Difference Equations of Elliptic Type*. Ph.D. thesis, Harvard University, Cambridge, Massachusett. (Cited on page 12.)

Zhang, Y., C. Seigneur, J.H. Seinfeld, M.Z. Jacobson, and F.S. Binkowski (1999). Simulation of aerosol dynamics: A comparative review of algorithms used in air quality models. *Aerosol Science and Technology*, 31:487–514. (Cited on pages 24, 30, and 73.)

Zufall, M.J. and C.I Davidson (1998). *Atmospheric Particles*, volume 5 of *IUPAC Series on Analytical and Physical Chemistry of Enviromental Systems*, chapter Dry Deposition of Particles, pages 425–473. Wiley, Chichester. (Cited on pages 109, 111, and 112.)

# ACKNOWLEDGMENTS

Now that I have passed beyond the final words of the final chapter of this work, I wish to thank and acknowledge the people and institutions that helped me to get here. The time I spent in Hamburg was rich and full of personal and professional experiences that one page can not cover.

I wish to thank Prof. K.H. Schlünzen for her kind support and encouragement to finish, and Prof. G. Lammel for his guidance and support throughout the entire length of my PhD. Prof. V. Wulfmeyer, Sandip Pal, Dr. A. Behrendt, Marcus Radlach and Prof. R. Wurster at the IPM of the UHOH for the scientific collaboration that made this project possible. The lidar group at the IPM provided me with their plotting scripts for the lidar scan geometry, and Dr. H.-S. Bauer and Thomas Schwitalla at the IPM provided me with the LM output which was used to force the LES model. The BWPLUS funded this project, and the MPI-MET and Prof. M. Claußen provided a unique work environment, and economic support during the final stages of this work. I want to acknowledge my colleagues of the MEMI group at the UHH, and the Aerosol Chemistry group at the MPI-MET as well as Dr. F. Müller and Dr. A. Chlond for their technical support and many profitable discussions. I also wish to thank Dr. L. Tarrason at the MET.NO, for the facilities that she provided me with in order to finish writing this thesis.

I arrived to Hamburg alone. With me I had only a backpack and the contact information of my supervisor-to-be. I had no fixed place to stay, no knowledge of the German language and no return ticket. When I left Hamburg, I had with me a family, friends scattered trough the world and a truck half full of stuff. Without the friends that I made during my stay, none of this would have come to be. Marin sheltered me when I arrived. Miren and Luis gave a home to all of us who were away. Gabi, Patrice and Luca were among my first friends in Hamburg, even if Gabi tried to deny it. In Francesca, Semeena and Irene I found much more than colleagues, and I am happy to count them as my friends. I also want to thank Dorothea, Melissa, Ole, Maria Paz, Nidia, Sabrina and Tobias for the wonderful time we spent together, both at Grindelhof 85 and in the 4th floor kitchen. I want to specially thank Irene for helping me with the German language and bureaucracy. I can not forget my chilean friends (or Miguel will never speak to me again) Marcelo, Ángela, Miguel, Pato, Nelson, Lucho and Juan Pablo, who shared their homesickness with me.

Finally I want to mention my family, to whom I am grateful for their love, support and understanding. To them, I dedicate this thesis. As a child my Abuela taught me that knowledge is the only true possesion, alas she forgot to tell me to be selective of what I learn. My parents have been extremely supportive and understanding with my choice of not buying a return ticket. A special thanks to Ingrid who took the painful work of proof reading, and never ceased to provide extra motivation.

## COLOPHON

This thesis was typeset with LaTeX $2_\varepsilon$ using the template developed by André Miede. The template is available for LaTeX via CTAN as "`classicthesis`".

*Final Version* as of 26th June 2009 at 14:55.

Die gesamten Veröffentlichungen in der Publikationsreihe des MPI-M
„Berichte zur Erdsystemforschung“,
„Reports on Earth System Science“,
ISSN 1614-1199

sind über die Internetseiten des Max-Planck-Instituts für Meteorologie erhältlich:

http://www.mpimet.mpg.de/wissenschaft/publikationen.html



ISSN 1614-1199